

# Mathematical and Computational Modeling of Biodegradation Behavior of Personalized Printed Implants

**Mojtaba Barzegari Shankil**

Supervisor:  
Prof. dr. ir. L. Geris

Dissertation presented in partial  
fulfillment of the requirements for the  
degree of Doctor of Engineering  
Science (PhD): Mechanical  
Engineering

November 2022



# **Mathematical and Computational Modeling of Biodegradation Behavior of Personalized Printed Implants**

**Mojtaba BARZEGARI SHANKIL**

Examination committee:

Prof. dr. ir. The Chairman, chair  
Prof. dr. ir. L. Geris, supervisor  
Prof. dr. ir. H. Van Oosterwyck  
Prof. dr. ir. N. Moelans  
Prof. dr. G. Závodszyk  
(University of Amsterdam)

Dissertation presented in partial  
fulfillment of the requirements for  
the degree of Doctor of Engineering  
Science (PhD): Mechanical Engineering

November 2022

© 2022 KU Leuven – Faculty of Engineering Science  
Uitgegeven in eigen beheer, Mojtaba Barzegari Shankil, Celestijnenlaan 300 box 2419, B-3001 Leuven (Belgium)

Alle rechten voorbehouden. Niets uit deze uitgave mag worden vermenigvuldigd en/of openbaar gemaakt worden door middel van druk, fotokopie, microfilm, elektronisch of op welke andere wijze ook zonder voorafgaande schriftelijke toestemming van de uitgever.

All rights reserved. No part of the publication may be reproduced in any form by print, photoprint, microfilm, electronic or any other means without written permission from the publisher.

# Preface

Here we will have acknowledgment, in which I talk about people supported me during my PhD.

سلام این یک تست است و من آن را برای شما نوشته ام. امیدوارم این نوشته ازاردنه نباشد. این متن برای قدردانیست و ممکن است کمی طولانی شود.

This is the continuation of the text.



# **Abstract**

...



# Beknopte samenvatting

...







# Contents

<b>Abstract</b>	iii
<b>Beknopte samenvatting</b>	v
<b>List of Abbreviations</b>	vii
<b>List of Symbols</b>	ix
<b>Contents</b>	ix
<b>List of Figures</b>	xv
<b>List of Tables</b>	xix
<b>I Introduction</b>	1
<b>1 Introduction</b>	2
1.1 Chemistry of biodegradation of magnesium . . . . .	2
1.1.1 Degradation rate evaluation techniques . . . . .	6
<b>2 Aim and objective</b>	7
<b>II Model Development</b>	9
<b>3 Developing the core computational model</b>	10
3.1 Introduction . . . . .	10
3.1.1 Magnesium biodegradation . . . . .	10
3.1.2 Computational modeling of Mg degradation . . . . .	11

3.2	Background theory . . . . .	13
3.2.1	Biodegradation as a reaction-diffusion system . . . . .	13
3.2.2	Moving boundary - Stefan problems . . . . .	14
3.2.3	Level set method . . . . .	15
3.3	Materials and methods . . . . .	15
3.3.1	Underlying chemistry . . . . .	15
3.3.2	Mathematical modeling . . . . .	16
3.3.3	Interface movement formulation . . . . .	18
3.3.4	Boundary conditions . . . . .	19
3.3.5	Implementation . . . . .	20
3.3.6	Experimental setup . . . . .	21
3.3.7	Parameter estimation . . . . .	22
3.3.8	Simulation setup . . . . .	24
3.3.9	Case study . . . . .	26
3.4	Results . . . . .	26
3.4.1	Optimization results . . . . .	26
3.4.2	Degradation prediction . . . . .	27
3.4.3	Example application . . . . .	29
3.5	Discussion . . . . .	29
3.6	Conclusions . . . . .	34
<b>4</b>	<b>Fluid flow and convection</b>	<b>37</b>
4.1	Introduction . . . . .	37
4.2	Methodology . . . . .	37
4.2.1	Navier-Stokes equations . . . . .	37
4.2.2	Weak formulation of the Navier-Stokes equations . . . . .	39
4.2.3	Stokes equations . . . . .	40
4.2.4	Implementation . . . . .	41
4.2.5	Considering the degrading object . . . . .	43
4.2.6	Simulation setup . . . . .	44
4.3	Results and discussion . . . . .	44
<b>5</b>	<b>Advanced model with kinetics</b>	<b>51</b>
5.1	Introduction . . . . .	51
5.2	Results . . . . .	53
5.2.1	Thermodynamics-based simulation . . . . .	53
5.2.2	Biodegradation simulations . . . . .	54
5.3	Discussion . . . . .	56
5.4	Methods . . . . .	56

5.5	Data Availability . . . . .	58
5.6	Code Availability . . . . .	58
5.7	Acknowledgements . . . . .	59
5.8	Author Contributions . . . . .	59
5.9	Competing Interests . . . . .	59
<b>6</b>	<b>Tissue growth modeling</b>	<b>63</b>
6.1	Introduction . . . . .	63
6.2	Deriving the model . . . . .	64
6.2.1	General equation of interface motion . . . . .	64
6.2.2	Phase-field formulation . . . . .	65
6.2.3	Level-set formulation . . . . .	66
6.3	Dimensionless forms for various cases . . . . .	67
6.3.1	Stationary interface . . . . .	67
6.3.2	Evolution under constant normal speed . . . . .	68
6.3.3	Curvature-driven interface evolution . . . . .	69
6.4	Numerical implementation . . . . .	69
6.5	Adapting the formulation for curvature-driven tissue growth . . . . .	71
6.A	Implementing the phase-field model using physics-informed neural networks . . . . .	72
<b>III</b>	<b>Code Implementation and Software Development</b>	<b>73</b>
<b>7</b>	<b>Model parallelization</b>	<b>74</b>
7.1	Introduction . . . . .	74
7.2	Background theory and model description . . . . .	77
7.2.1	Chemistry of degradation . . . . .	78
7.2.2	Reaction-diffusion equation . . . . .	78
7.2.3	Level set method . . . . .	80
7.3	Methodology of model implementation . . . . .	82
7.3.1	Finite element discretization (bottleneck of the algorithm)	83
7.3.2	Implementation and parallelization . . . . .	87
7.3.3	Level set issues . . . . .	90
7.3.4	Simulation setup . . . . .	92
7.3.5	Performance analysis . . . . .	93
7.3.6	Compute environment . . . . .	95
7.4	Results . . . . .	95
7.4.1	Numerical simulation results . . . . .	95

7.4.2 Weak and strong scaling results . . . . .	96
7.5 Discussion . . . . .	98
7.6 Conclusion . . . . .	101
7.A Comparing the performance of different combinations of KSP types and preconditioners . . . . .	102
<b>8 BioDeg software</b>	<b>105</b>
8.1 Summary . . . . .	105
8.2 Statement of need . . . . .	106
8.3 Overview of BioDeg . . . . .	107
8.3.1 Basic concepts . . . . .	107
8.3.2 Implementation . . . . .	108
8.3.3 High-performance computing . . . . .	110
8.3.4 Installation . . . . .	110
8.3.5 Documentation . . . . .	111
8.3.6 Contribution . . . . .	111
8.3.7 Published works . . . . .	112
8.4 Acknowledgements . . . . .	112
<b>9 Bayesian parameter estimation of the computational models</b>	<b>113</b>
9.1 Summary . . . . .	113
9.2 Statement of Need . . . . .	115
9.3 Learning objectives . . . . .	115
9.4 Prerequisites . . . . .	116
9.5 Pedagogy and instructional design . . . . .	116
9.6 Getting started . . . . .	117
9.7 Acknowledgements . . . . .	117
9.A A glimpse of the Jupyter notebook . . . . .	118
9.A.1 Introduction . . . . .	118
9.A.2 Bayesian optimization . . . . .	119
9.A.3 Sample problem . . . . .	121
<b>IV Model Applications</b>	<b>123</b>
<b>10 Applications: Mandible plate</b>	<b>124</b>
10.1 Introduction . . . . .	124
10.2 Materials and methods . . . . .	127
10.2.1 Case study . . . . .	127
10.2.2 Biodegradation behavior simulation . . . . .	127

10.2.3 Mechanical behavior simulations . . . . .	130
10.2.4 Bone healing and implant load models . . . . .	133
10.2.5 Coupling of the models . . . . .	136
10.3 Results . . . . .	137
10.3.1 Biodegradation results . . . . .	137
10.3.2 Sensitivity analyses . . . . .	137
10.3.3 Coupled models results . . . . .	139
10.4 Discussion . . . . .	140
10.5 Future perspectives . . . . .	142
<b>11 Applications: Acetabular cup</b>	<b>145</b>
11.1 Introduction . . . . .	145
11.2 Materials and Methods . . . . .	146
11.3 Results and Discussion . . . . .	147
11.4 Conclusions . . . . .	148
11.5 Acknowledgments . . . . .	148
<b>12 Applications: Mechanical integrity of infilled structures</b>	<b>151</b>
<b>V Conclusion and General Discussion</b>	<b>153</b>
<b>13 Conclusion</b>	<b>154</b>
<b>Bibliography</b>	<b>155</b>
<b>List of publications</b>	<b>173</b>



# List of Figures

1.1	Commonly used electrolytes for testing biodegradable metals . . . . .	3
1.2	Mg biodegradation behavior in commonly used test solutions . . . . .	5
3.1	Simplified chemistry of biodegradation of Mg . . . . .	17
3.2	Schematic overview of exposed boundary conditions and constraints for biodegradation simulations . . . . .	20
3.3	Simulation setup of the biodegradation tests . . . . .	25
3.4	Simulation results of the cuboid sample in the biodegradation test	28
3.5	Change of concentration of various chemical components over a line . . . . .	29
3.6	Simulation results of the sample screw in the biodegradation test	30
4.1	Fluid flow model construction for comparison with experimental setup . . . . .	44
4.2	Comparing streamline results of developed CFD code and OpenFOAM - side view . . . . .	45
4.3	Comparing streamline results of developed CFD code and OpenFOAM - top view . . . . .	46
4.4	Comparing flow field results of developed CFD code and OpenFOAM . . . . .	47
4.5	Comparing flow field results of developed CFD code and OpenFOAM - zoomed view . . . . .	48
4.6	Biodegradation simulation results in the presence of fluid flow . . . . .	49
4.7	Fluid flow streamlines in the presence of a degrading object . . . . .	50
5.1	Hydra-Medusa software output for given experimental conditions	54
5.2	Simulation results for local pH predictions . . . . .	55
5.3	Experimental results for distribution of local pH above the sample	56

5.4 Comparing computational and experimental for horizontal line scans of local pH . . . . .	57
5.5 Comparing computational and experimental vertical pH profiles . . . . .	57
5.6 Experimental setup for validating the coupled biodegradation model . . . . .	60
5.7 Computational model setup for local pH simulations . . . . .	61
6.1 Comparison of phase field variable and level set function . . . . .	68
7.1 Schematic presentation of different components of the studied moving boundary problem . . . . .	77
7.2 The implicit function definition in the studied problem . . . . .	81
7.3 Overlapping domain decomposition . . . . .	89
7.4 Comparison of the sparsity patterns of the global matrix A . . . . .	89
7.5 Simulation setup for evaluating parallel performance . . . . .	93
7.6 Models used for performing the weak-scaling test . . . . .	94
7.7 Numerical simulation result of the reaction-diffusion system . . . . .	96
7.8 Weak-scaling test result . . . . .	97
7.9 Speed-up and parallel efficiency of the weak-scaling experiment . . . . .	97
7.10 Strong-scaling test result . . . . .	98
7.11 Speed-up and parallel efficiency of the strong-scaling test . . . . .	98
7.12 Performance test result for various preconditioners and solvers .	103
8.1 Simulation result of degradation of a screw performed using BioDeg . . . . .	109
9.1 A typical output of the parameter estimation process . . . . .	122
10.1 The change in mechanical integrity of the implant and tissue strength over time (Adapted from Chen et al. [1]) . . . . .	125
10.2 Miniplate fixation by AO Surgery Foundation [2] . . . . .	128
10.3 Occurrence of compressive- and tensile stresses around the fracture site when biting [3] . . . . .	128
10.4 Model for the jaw plate . . . . .	129
10.5 Five, four or two screws . . . . .	129
10.6 True stress-strain curve of WE43 [4] . . . . .	131
10.7 Top view of the jaw plate with five screws with dimensions and boundary conditions . . . . .	132
10.8 Mandible with indication of fracture line, jaw plate, lever arm and load [5] . . . . .	133

10.9 cross-section of the mandibular body on the left and approximation of this cross-section with dimensions on the right [6] . . . . .	134
10.10 Close view of the cross-section of the jaw plate (indicated with JP in the figure) around the third hole (arbitrary, break does not always occur around this hole) with dimensions . . . . .	135
10.11A cross-section of the computational mesh and simulation results of the degradation model of the jaw bone plate in SBF solution as well as the mass loss graph over time. The contours display the concentration of magnesium ions on a cross-section view of the medium beside the moving surface of the bone plate at 1) 1st day (initial state), 2) 40th day, 3) 80th day, and 4) 120th day. The gray surface is the zero iso-contour of the level set function, which indicates the surface of the bone plate. . . . .	137
10.12 Results of tensile test on jaw plate with five screws with different amounts of corrosion . . . . .	139
10.13 Maximal force that can be carried by the jaw plate in each case and estimation of load occurrence as a function of time after implantation in days for five screws . . . . .	139
10.14 Flow chart for the process of iteratively designing a suitable jaw plate . . . . .	142
11.1 Application of the acetabular implant . . . . .	146
11.2 Computational biodegradation model for the porous acetabular implant . . . . .	146
11.3 Mesh decomposition of the acetabular implant model . . . . .	147
11.4 Infilled acetabular implant . . . . .	148
11.5 Biodegradation rate for the acetabular implant . . . . .	149
11.6 Visualization of the change of morphology of the acetabular implant . . . . .	149
11.7 Strong scaling of individual components of the biodegradation model . . . . .	150
11.8 Weak and strong scaling of of the acetabular implant model . . . . .	150



# List of Tables

1.1	Summary of various common methods to asses the degradation rate of Mg . . . . .	6
3.1	Chemical composition of NaCl and SBF electrolytes . . . . .	23
3.2	Effective parameters to be considered in the Bayesian optimization for parameter calibration . . . . .	27
3.3	Values used in the biodegradation model simulation performance	27
5.1	Solubility products of related chemical reactions . . . . .	59
5.2	Chemical composition of the HBSS electrolyte . . . . .	59
5.3	The elemental composition of highly-pure and commercial-pure Mg . . . . .	60
7.1	Strong-scaling test result, presented by the execution time of each PDE in simulations with a different number of employed MPI cores. . . . .	97
7.2	Performance test result for various combinations of preconditioners and solvers, presented by the execution time of each PDE.	103
10.1	Material parameters for WE43 . . . . .	131
10.2	Dimensions and mesh size of the different models for the jaw plate with five screws, along with the DAF value . . . . .	132
10.3	Details about the FE analysis . . . . .	132



# **Part I**

# **Introduction**

# **Chapter 1**

## **Introduction**

The application of biodegradable metallic biomaterials [7, 8, 9], including magnesium [10, 11, 12], zinc [13, 14], and iron [15], has become more prominent for over a decade in various biomedical engineering and tissue engineering disciplines. Among the mentioned materials, magnesium (Mg) is the most studied metals [16], the reason of which is its suitable mechanical and chemical properties for biomedical applications. Although poor corrosion resistance of Mg is a limiting factor for its application as a light structural material, like in transportation industry, it becomes an interesting characteristic when it comes to biodegradable materials field for cardiovascular and orthopedic applications [17, 18, 19]. The first clinical usage of Mg was reported in 1878, but a renewed interest on it has grown significantly in the last 15-20 years [16]. From the clinical and biomedical perspective, two major concerns about using Mg in clinics are the release of hydrogen gas and surface alkalization due to Mg dissolution [20]. These issues are commonly addressed by alloying, biocompatible coating, and surface modification [16].

### **1.1 Chemistry of biodegradation of magnesium**

The biodegradation behavior of Mg is investigated in corrosion tests, in which the selection of the corrosive media plays an important role since it affects the underlying chemical reactions [21]. By considering the main application

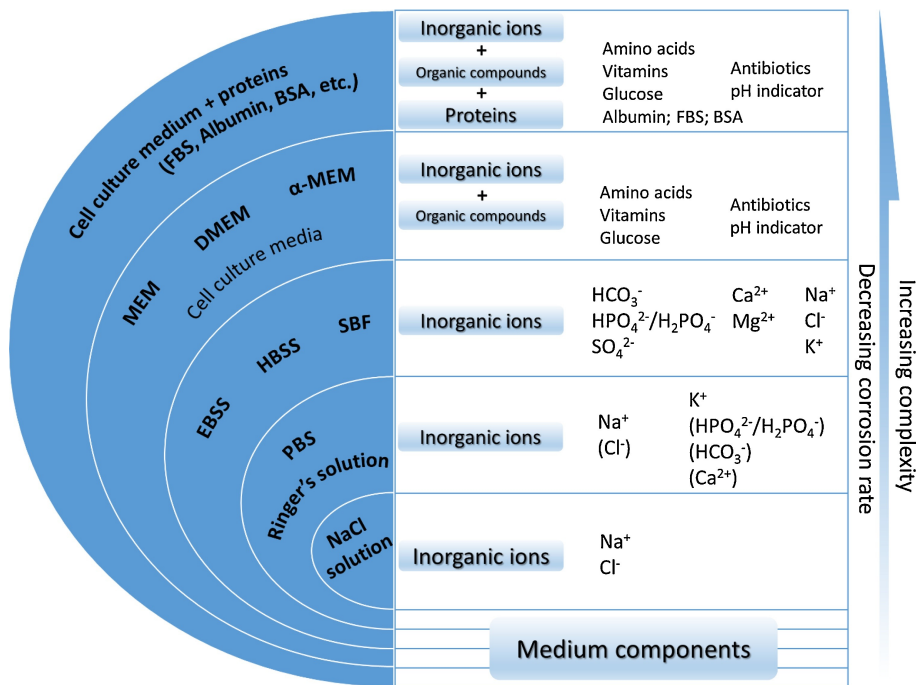


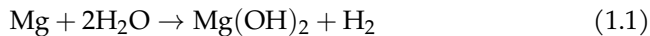
Figure 1.1: A schematic representation of commonly used electrolytes for testing biodegradable metals, sorted by their complexity from the chemical perspective from bottom to top [21].

of the biomaterial, which can be tissue engineering scaffolds, vascular stents, or orthopedic fixation implants, the corrosive media can be selected to be a representative of the service environment. The most basic form of the medium is a saline ( $\text{NaCl}$ ) solution, in which the degradation rate is the highest possible [21]. More complex solutions can be used to mimic the behavior of body environment by taking into account more body fluid components, the most popular of which are the Ringer's solution, PBS (phosphate buffered saline), SBFs (simulated body fluids), HBSS (Hank's balanced salt solution), and Earle's balanced salt solution (EBSS) [21]. Adding more organic components to the solution will make it ready to simulate cell culture conditions. The common media for this purpose are MEM (Minimum Essential medium) and DMEM (Dulbecco's modified Eagle's medium) [21]. Fig. 1.1 summarizes various commonly used electrolytes for testing biodegradable metals [21].

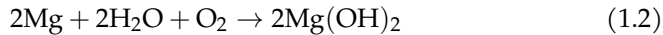
A wide range of various studies have already investigated the effect of different components in the aforementioned corrosive media on the degradation behavior of Mg materials [22, 23, 24, 25, 26]. In addition to the presented chemical components, synthetic pH buffers (such as Tris as HEPES) has been shown to contribute to the biodegradation rate of Mg [22]. The performed investigations on the effect of different inorganic components, including carbonate, phosphate, sulfate, and calcium, show the effective contribution of these components on the rate of degradation, although the corrosion protection resulted from the mutual effect of carbonate, phosphate and calcium has been more emphasized [22, 25].

The most common solution for performing corrosion test on Mg is saline (NaCl) solution, in which the material undergoes an aggressive corrosion due to higher electrochemical activities [27, 28]. In a typical aqueous solution, the major corrosion reactions occurring can be written as [29, 30]:

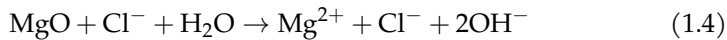
Main, hydrogen evolution reaction (HER):



Secondary, oxygen reduction reaction (ORR):



In this situation, the corrosion products forming on the corroded surface of Mg consists mainly of  $\text{Mg(OH)}_2$  and  $\text{MgO}$ , and the pH in regions close to this surface remains alkaline. In presence of chloride ions in the saline medium, the formed corrosion product may be broken or bypassed, leading to increased degradation rate:



The main advantage of using a saline solution for corrosion tests in comparison to more complex media is that absence of inorganic ions like carbonate, phosphate, sulfate, and calcium allows investigating the corrosion behavior without concerning possible contamination by microbial life. On the other hand, the main weakness of saline solution is that it cannot represent the

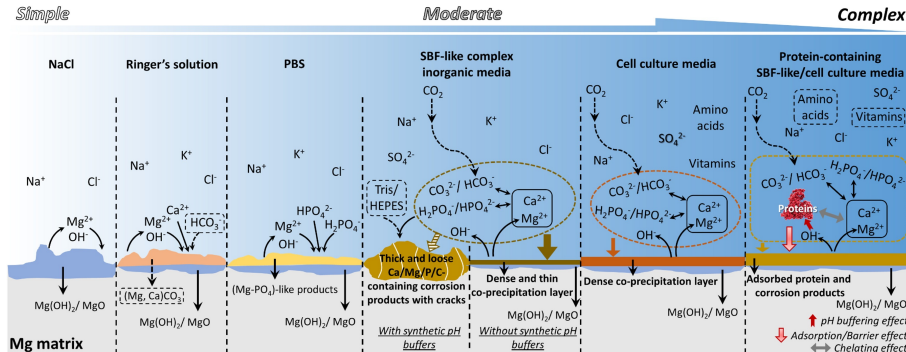


Figure 1.2: A schematic representation of Mg biodegradation behavior in commonly used solutions for corrosion tests of biodegradable metals [21].

complexity of real body fluid, and as a result, a more complex medium is required to investigate such conditions. To address this issue, more complex saline solutions, such as PBS are widely used for assessing the applicability of Mg alloys in more complex conditions from the chemical perspective [31, 32]. Despite the mentioned limitations, corrosion test in saline solution is beneficial for understanding intrinsic degradation properties of Mg.

The term "simulated body fluid" is generally used to refer to solutions containing inorganic ions of human serum and interstitial fluid in corrosion tests [21]. The commonly used media in this regard are SBF, HBSS, and EBSS, which include the same inorganic components with a slight difference in their concentrations. A typical composition of these media is chloride, carbonate, phosphates, sulfate, and calcium. The individual effect of these components on the rate of degradation of Mg has been extensively studied, in which it has been observed that carbonate and phosphate slow down the rate while the effect of sulfate is negligible [24, 26]. The concentration of  $HCO_3^-$  affects the pH buffering capacity and the degradation rate of Mg simultaneously [33]. The effect of calcium ion is more complex because it doesn't contribute to the Mg corrosion directly. Fig. 1.2 briefly summarizes the various reactions and formed precipitation compositions of the mentioned media for testing the degradation behavior of Mg [21].

### 1.1.1 Degradation rate evaluation techniques

Generally speaking, the method used for evaluating the degradation rate can affect the reported behavior. For example, it has been shown that in HBSS, the measured corrosion rate of Mg is lower (slower) when evaluated using hydrogen evolution in comparison to the rate found by direct weight loss measurements [41, 42], which can be due to the secondary dissolution of evolved hydrogen. Moreover, the consumption of oxygen due to secondary ORR can affect the volume of evolved gas, which is more significant for media with slower degradation rate such as HBSS and MEM [43]. Table 1.1 summarizes the advantages and shortcomings of widely used techniques for measuring degradation rate [21].

Table 1.1: Summary of various common methods to asses the degradation rate of Mg

Test method	Advantages	Shortcomings
Weight loss	High reliability Direct measurement Easily controlled test environment	Non-continuous. Does not reveal varying corrosion rate throughout the immersion Low sensitivity at the initial stages
Hydrogen evolution	Continuous Can be automated Can be performed in closed eu-dimeters	Performed in open environment in most cases Might show underestimated values of corrosion rate due to secondary ORR and solubility of H <sub>2</sub> in aqueous media
Potentiodynamic polarization	Fast measurement	Non-continuous Open environment measurement in most cases Very often low correlation with long-term weight loss measurements
Electrochemical impedance spectroscopy	Continuous In situ investigation of protective properties of forming corrosion products	Performed in open environment in most cases

Introducing some symbol:  $\Theta$ .

Introducing an acronym: MD.

## **Chapter 2**

### **Aim and objective**



## **Part II**

# **Model Development**

# Chapter 3

## Developing the core computational model

This chapter is based on previously published content in *Corrosion Science*: M. Barzegari, D. Mei, S. V. Lamaka, and L. Geris, “Computational modeling of degradation process of biodegradable magnesium biomaterials,” *Corrosion Science*, vol. 190, p. 109674, Sep. 2021.

### 3.1 Introduction

#### 3.1.1 Magnesium biodegradation

Due to their bio-friendly properties, biodegradable metallic biomaterials, including magnesium (Mg), iron (Fe), and zinc (Zn), are regaining attention in recent years [7]. These biomaterials find important applications in the design and manufacturing of supportive implants such as temporary devices in orthopedics and the cardiovascular field [44, 10]. In orthopedics, the biodegradable metallic biomaterials are used as fixation devices, providing adequate support in the early stages while being absorbed gradually during the bone healing process [45]. Implants fabricated using Mg and its alloys are being used for such a purpose [46] due to the similarity of the stiffness between

natural bone and Mg, which helps to reduce the stress shielding induced by the implanted device. Additionally, Mg is reported to have a non-toxic contribution to the human body's metabolism and the bone healing process, which makes the release and absorption of metallic ions safe and biocompatible [47].

Accumulation of mechanistic understanding of Mg degradation achieved by experimental approaches over the years gradually provided a mechanistic understanding of the biodegradation process. Combining these insights with *in silico* modeling approaches enables researchers to study the biodegradation properties and behavior of the implant in a virtual environment prior to conducting any *in vitro* or *in vivo* tests. When fully validated, computational modeling can (in part) replace certain stages of costly and time-consuming experiments verifying the expected degradation behavior of the designed implants. Additionally, the developed models can be efficiently combined with existing computational models to examine other related phenomena such as tissue growth or mechanical integrity.

### 3.1.2 Computational modeling of Mg degradation

Previous contributions to the computational modeling of the degradation process include a wide range of different approaches, from the basic phenomenological implementations to comprehensive mechanistic models that take into account various aspects of the degradation and resorption process.

Continuous damage (CD) modeling has always been a common approach for corrosion simulation, but from a physicochemical point of view, it focuses on the mechanical integrity of the degradation and neglects the diffusion process. As a result, its application in the degradation modeling of biomaterials, which includes various fundamental phenomena such as mass transfer through diffusion and reaction, is relatively limited. Despite this issue, a CD model proposed by Gastaldi et al. showed a good performance for simulation of bioresorbable Mg-based medical devices [48], in which geometrical discontinuities were interpreted as the reduction of material.

Alternatively, mathematical modeling using transport phenomena equations has shown great flexibility in capturing different mechanisms involved in the biodegradation process. As an example, in Ahmed et al., a set of mathematical equations in cylindrical and spherical coordinates was derived to model the chemical reactions of Mg degradation [49]. Despite the simplicity of

their approach from the computational perspective, their model was able to demonstrate the contribution of various chemical components to the *in vitro* degradation of Mg. Similarly, Grogan et al. developed a mathematical model based on the Stefan problem formulation in 1D space to correlate the mass flux of metallic ions into the solution to the velocity of shrinkage of the material during degradation [50]. This was done by considering the mass diffusion and change of the concentration of Mg<sup>2+</sup> ions, and then, employing an arbitrary Eulerian-Lagrangian (ALE) approach to extend the model to 3D on an adaptive mesh. A similar approach was taken by Shen et al. to develop a theoretical model of the degradation behavior of Mg-based orthopedic implants showing great consistency with *in vitro* test results [51].

An ultimate application of the computational modeling of the biodegradation process of biomaterials can be the prediction of how biodegradation affects the shape of the bulk material, medical device, or implant over time. One of the ways to achieve such a prediction is to capture the movement of the corrosion front mathematically using an appropriate method. The level set method (LSM) is a widely used example in this regard, which is an implicit mathematical way of representing the moving interfaces. This approach was used in Wilder et al. to study galvanic corrosion of metals [52]. They employed LSM on an adaptive mesh to track the moving corrosion interface, but their model lacked a thorough validation using experimental data. Gartzke et al. also worked on a simplified representation of the interface movement by developing a mechanochemical model of the biodegradation process, which helped them to study the effect of degradation on the mechanical properties [53]. They performed a basic qualitative validation on the predictions made by the model. Another similar study in this regard is the Sun et al. work [54], in which a detailed mathematical model was derived and validated to study the deposition of corrosion products on the surface of materials. This mathematical approach was also employed in the biomedical field by Bajger et al. to study the mass loss of Mg biomaterials during biodegradation [55]. They used LSM as well as a set of reaction-diffusion equations to track the change of geometry, which can be directly correlated to the loss of material. The derived equations were also able to capture the formation of the corrosion film that decreases the rate of degradation. Another comprehensive mathematical model was developed by Sanz-Herreraa et al. to investigate the role of multiple chemical components involved in the *in vitro* degradation of Mg implants [56]. One important drawback of this study was its 2D nature. Although the computational model was capable of studying the effect of multiple

components, due to the high number of derived equations, it would be difficult to extend and use the same model for real 3D implants. Additionally, a 2D model cannot capture the full phenomenon of corrosion, and as a result, the validation of the model will be more qualitative. It was shown in the study conducted by Gao et al. [57], where they compared the results of a multi-dimension model of the degradation of cardiovascular stents with those of a single-dimension model, that the number of considered dimensions had an important effect on the model predictions. In the end, it is worth mentioning that no dedicated experiments were performed in the aforementioned studies to validate the constructed mathematical and computational models.

The current study focuses on developing a physicochemical model of the biodegradation process of commercially-pure (CP) Mg biomaterials by continuing the work of Bajger et al. [55]. In this model, a set of partial differential equations (PDE) was derived according to the underlying chemistry of biodegradation, described as reaction-diffusion processes taking place at the interface of the biomaterial and its surrounding environment. The formation of a protective layer, effects of the ions in the solution, and the change in the pH due to the corrosion phenomenon were taken into account in the mathematical model. The corresponding computational model was implemented in a fully parallelized manner. Model calibration and validation were executed using data obtained from the immersion tests performed in saline (NaCl) and simulated body fluid (SBF) solutions.

## 3.2 Background theory

### 3.2.1 Biodegradation as a reaction-diffusion system

The biodegradation process can be considered as a reaction-diffusion system [58], in which the ions are released due to the chemical reactions on the surface, and the released ions diffuse through the surrounding solution and materials. These ions can interact with other ions and form new compounds [21]. As the reaction-diffusion systems have been studied in science and engineering for a couple of decades, the analogy with a reaction-diffusion system makes it convenient to construct a mathematical model of the biodegradation process based on the well-established transport phenomena equations [59]. From the mathematical perspective, a reaction-diffusion system is expressed by a set of

parabolic PDEs that describe the conservation of contributing chemical species in the studied system.

### 3.2.2 Moving boundary - Stefan problems

Moving boundary problems, also called Stefan problems, are the general class of mathematical problems in which the boundary of the domain should also be calculated in addition to the solution of the other equations [60]. Coupling the reaction-diffusion system of biodegradation with a moving boundary problem constructs a mathematical model in which the change of the domain geometry due to the material loss can be correlated to the underlying reaction and diffusion processes of corrosion. As the geometry can be determined accurately, this approach provides a way to measure the mass loss directly by computing the change in the volume of the material. In such a system, the moving boundary is the material-solution interface (corrosion front).

For a 1D corrosion diffusion system, the position of the diffusion interface can be determined by [60]:

$$s(t) = s_0 + 2\alpha\sqrt{t}, \quad (3.1)$$

in which the  $s(t)$  represents the position at any given time, and  $s_0$  is the initial interface position.  $\alpha$  coefficient can be calculated using:

$$\alpha = \frac{[Mg]_0 - [Mg]_{sat}}{[Mg]_{sol} - [Mg]_{sat}} \sqrt{\frac{D}{\pi}} \frac{\exp\left(\frac{-\alpha^2}{D}\right)}{\operatorname{erfc}\left(\frac{-\alpha}{\sqrt{D}}\right)} \quad (3.2)$$

where  $[Mg]_{sol}$  is the concentration in the solid bulk (i.e. materials density) and  $[Mg]_{sat}$  is the concentration at which the material is released to the medium.  $[Mg]_0$  represents the initial concentration of the metallic ions in the medium, which is usually zero for most corrosion cases.

Eqs. 3.1 and 3.2 can be used to simply track the movement of the corrosion front, which is the employed method in studies like the Gorgan et al. work [50], but apparently, the real-world corrosion problems are 3D and much more complex than the described system.

As will be described later, Eq. 3.1 is used strictly for the first time step of the simulations in low diffusion regimes for calculating the initial velocity of the

interface. Generally speaking, a more sophisticated approach, such as the level set method, is required for tracking the interface of complex 3D geometries.

### 3.2.3 Level set method

In the current study, the corrosion front is tracked using an implicit function such that the zero iso-contour of the function represents the metal-solution interface. As a common practice, this implicit function is expressed as a signed distance function that defines the distance of each point of space (the domain of interest) to the interface. Such a definition implies that the zero iso-contour of the function belongs to the interface. The level set method provides an equation to declare such an implicit function,  $\phi = \phi(\mathbf{x}, t)$ ,  $\mathbf{x} \in \Omega \subset \mathbb{R}^3$ , which can be obtained by solving [61]:

$$\frac{\partial \phi}{\partial t} + \vec{V^E} \cdot \nabla \phi + V^N |\nabla \phi| = b\kappa |\nabla \phi| \quad (3.3)$$

in which  $\vec{V^E}$  is the external velocity field, and  $V^N$  is the value of the normal interface velocity. The last term is related to the curvature-dependent interface movement and is omitted. As the effect of perfusion is neglected in the current study, the term containing the external velocity is also eliminated, resulting in the following simplified form of the level set equation:

$$\frac{\partial \phi}{\partial t} + V^N |\nabla \phi| = 0. \quad (3.4)$$

By having the normal velocity of the interface ( $V^N$ ) at each point and solving Eq. 3.4, the interface can be captured at the zero iso-contour of the  $\phi$  function.

## 3.3 Materials and methods

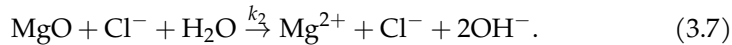
### 3.3.1 Underlying chemistry

The chemistry of biodegradation of Mg depends considerably on the surrounding solution and the presence of certain ions [21]. In NaCl solutions, the anodic and cathodic reactions as well as the formation and elimination of side

corrosion products can be considered as follows [7]:



Reaction 3.6 is not fully correct from the chemical point of view. In fact, Mg surface is always covered by MgO layer, and Mg(OH)<sub>2</sub> forms on top of that either at atmospheric conditions or during the immersion. The integrity of this MgO layer is undermined by Cl<sup>-</sup> ions, leading to an increase in degradation rate:



Although Cl<sup>-</sup> formally does not participate in reaction 3.7, it reflects the dependence of Mg corrosion rate on Cl<sup>-</sup> concentration. This effect on the rate of degradation has been widely expressed as the effect of Cl<sup>-</sup> on the Mg(OH)<sub>2</sub> in the literature [7, 10]. In the developed model, this effect is used interchangeably by omitting the MgO component, so the protective film formed on the corrosion interface is assumed to contain Mg(OH)<sub>2</sub> only. Moreover, it has been shown recently that oxygen reduction reaction also takes place during corrosion of Mg [43, 62, 38]. However, this is a secondary reaction (complementing water reduction) contributing to 1-20% of the total cathodic current depending on the conditions. Hence, it is not taken into consideration in this model. Additionally, the involved chemical reactions are more complicated in SBF solutions due to the presence of further inorganic ions and the formation of a layered precipitate structure [21], but the effect of these ions is currently encapsulated in the reaction rates and the diffusion coefficients of the developed mathematical model. The summary of the considered chemistry to develop the mathematical model is depicted in Fig. 3.1.

### 3.3.2 Mathematical modeling

To keep track of the concentration changes of various contributing chemical components, we define four state variables for the concentration of Mg<sup>2+</sup> ions, protective film (Mg(OH)<sub>2</sub>), chloride (Cl<sup>-</sup>) ions, and the hydroxide (OH<sup>-</sup>)

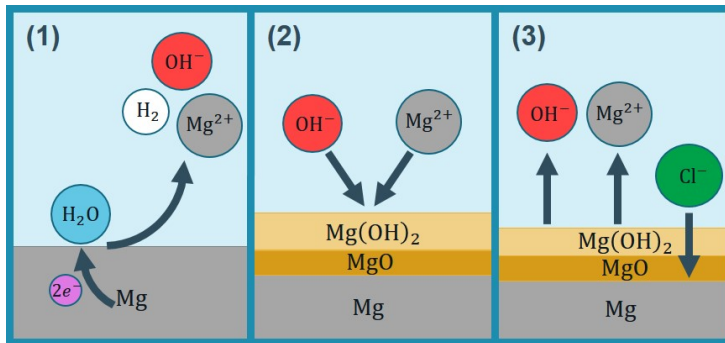


Figure 3.1: The chemistry of biodegradation of Mg considered in the current study: 1) Mg oxidation and water reduction processes accompanied by releasing  $Mg^{2+}$  and  $OH^-$  ions as well as  $H_2$  gas, 2) formation of a partially protective precipitation layer, 3) dynamic solubility equilibrium and contribution of  $Cl^-$ .

ions:

$$\begin{aligned} C_{Mg} &= C_{Mg}(\mathbf{x}, t), \quad C_{Film} = C_{Film}(\mathbf{x}, t) \\ C_{Cl} &= C_{Cl}(\mathbf{x}, t), \quad C_{OH} = C_{OH}(\mathbf{x}, t) \quad \mathbf{x} \in \Omega \subset \mathbb{R}^3' \end{aligned} \quad (3.8)$$

which are indeed 4 scalar functions of space and time.  $\Omega$  denotes the whole region of interest, including both the Mg bulk and its surrounding medium. By doing this, the value of pH at each point of  $\Omega$  can be calculated as:

$$pH = 14 + \log_{10} C_{OH}, \quad (3.9)$$

where  $C_{OH}$  implies the activity of  $OH^-$ . By having the definition of the state variables in Eq. 3.8, the biodegradation of Mg described by Eqs. 3.5 and 3.6 can be represented as a set of reaction-diffusion PDEs:

$$\frac{\partial C_{Mg}}{\partial t} = \nabla \cdot (D_{Mg}^e \nabla C_{Mg}) - k_1 C_{Mg} \left( 1 - \beta \frac{C_{Film}}{[Film]_{max}} \right) + k_2 C_{Film} C_{Cl}^2 \quad (3.10)$$

$$\frac{\partial C_{Film}}{\partial t} = k_1 C_{Mg} \left( 1 - \beta \frac{C_{Film}}{[Film]_{max}} \right) - k_2 C_{Film} C_{Cl}^2 \quad (3.11)$$

$$\frac{\partial C_{Cl}}{\partial t} = \nabla \cdot (D_{Cl}^e \nabla C_{Cl}) \quad (3.12)$$

$$\frac{\partial C_{\text{OH}}}{\partial t} = \nabla \cdot (D_{\text{OH}}^e \nabla C_{\text{OH}}) + k_2 C_{\text{Film}} C_{\text{Cl}}^2 \quad (3.13)$$

in which the maximum concentration of the protective film can be calculated according to its porosity ( $\epsilon$ ) [55]:

$$[\text{Film}]_{\text{max}} = \rho_{\text{Mg(OH)}_2} \times (1 - \epsilon). \quad (3.14)$$

$D^e$  is the effective diffusion coefficient for each component. Due to the formation of the protective film, the diffusion coefficient is not constant and varies from the actual diffusion coefficient of the ions to a certain fraction of it. This fraction can be defined as  $\epsilon/\tau$  [63, 64], in which  $\epsilon$  and  $\tau$  are the porosity and tortuosity of the protective film, respectively. The effective diffusion coefficient can be then calculated by interpolating the two aforementioned values:

$$D_i^e = D_i \left( \left( 1 - \beta \frac{C_{\text{Film}}}{[\text{Film}]_{\text{max}}} \right) + \beta \frac{C_{\text{Film}}}{[\text{Film}]_{\text{max}}} \frac{\epsilon}{\tau} \right). \quad (3.15)$$

The  $\beta$  coefficient is called momentum here and controls the effect of the saturation term  $(1 - \frac{C_{\text{Film}}}{[\text{Film}]_{\text{max}}})$ . The derivation of these equations is discussed in detail in our previous work [65].

### 3.3.3 Interface movement formulation

In order to take advantage of the level set method for tracking the corrosion front, the velocity of the interface at each point should be determined. Then, by solving Eq. 3.4, the interface is obtained at the points with a zero value of the  $\phi$  function. The interface velocity in mass transfer problems can be calculated using the RankineHugoniot equation [66], and by considering the transportation of  $\text{Mg}^{2+}$  ions, it can be written as:

$$\{\mathbf{J}(x, t) - ([\text{Mg}]_{\text{sol}} - [\text{Mg}]_{\text{sat}}) \mathbf{V}(x, t)\} \cdot n = 0 \quad (3.16)$$

where  $\mathbf{J}$  is the mass flux at the interface. Rearranging Eq. 3.16 and inserting the value of the normal interface velocity into Eq. 3.4 yields:

$$\frac{\partial \phi}{\partial t} - \frac{D_{\text{Mg}}^e \nabla_n C_{\text{Mg}}}{[\text{Mg}]_{\text{sol}} - [\text{Mg}]_{\text{sat}}} |\nabla \phi| = 0, \quad (3.17)$$

which is the final form of the level set equation to be solved. In the case of simulations with a low diffusion rate, the interface moves slowly in the

beginning, which results in a linear degradation, whereas based on the experimental results, the degradation rate is fast at the beginning and slows down eventually [22]. So, to mimic the same behavior in the low diffusion regimes, we took advantage of the theoretical Stefan formulation (Eqs. 3.1 and 3.2) to push the interface in the first time step. According to Eq. 3.1, the velocity of the interface can be calculated as  $(2\alpha/\sqrt{t})$ , but as we are dealing with a 3D model and not a 1D one, we pick a fraction (denoted by  $\gamma$ ) of this ideal value to be used as the driving force of the interface at the beginning of the simulation. So, the normal velocity of the interface can be written in the general form as:

$$V^N(x, t) = \begin{cases} \gamma \frac{2\alpha}{\sqrt{t}} & t = 0 \\ \frac{D_{Mg}^e \nabla_n C_{Mg}}{[Mg]_{sol} - [Mg]_{sat}} & t > 0 \end{cases} \quad (3.18)$$

in which the  $\alpha$  value should be calculated from Eq. 3.2. By selecting  $\gamma$  equal to zero, the Stefan formulation can be eliminated, and a value of 1 for  $\gamma$  restores the ideal 1D velocity definition.

### 3.3.4 Boundary conditions

The implementation of boundary conditions is relatively challenging and complex for the developed model as they should be imposed inside the domain of interest on virtual interfaces defined by mathematical expressions (i.e. on the moving interface defined by the zero iso-contour of the level set equation). The penalty method was used to overcome this issue and define the desired boundary conditions on the moving corrosion front.

Fig. 3.2 demonstrates a schematic presentation of the boundary conditions and general considerations of each PDE of the biodegradation mathematical model. This figure is divided into 5 different parts, presenting the 5 PDEs of the model. The Mg block is depicted in the center, and the interface separates it from the surrounding medium. There is no specific boundary condition for the level set and film formation equations, but in comparison to the other 3 transport equations, it should be noted that diffusivity is not considered for  $Mg(OH)_2$ , which is also reflected in Eq. 3.11. The level set function  $\phi$  is defined in a way that is positive inside and negative outside the solid region. For the  $Mg^{2+}$  ions transport equation, a Dirichlet boundary condition is applied on the mathematical interface to make the concentration equal to the saturation concentration of  $Mg^{2+}$  ions, a value that was already used in Eq. 3.17. For

the  $\text{Cl}^-$  and  $\text{OH}^-$  ions transport equations, a no-flux boundary condition is applied to the interface by making the diffusion coefficient equal to zero inside the Mg block, preventing ions to diffuse inside the solid material.

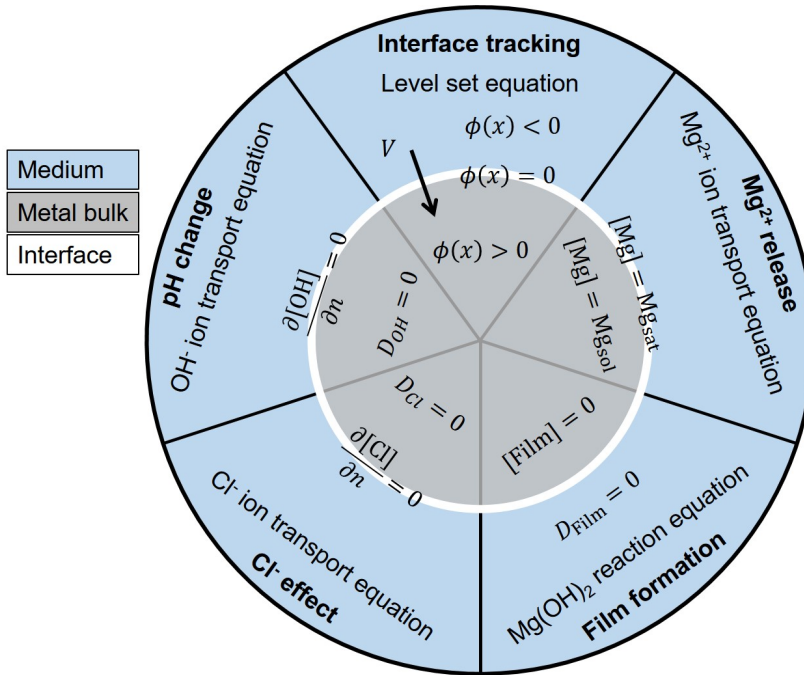


Figure 3.2: A schematic overview of the exposed boundary conditions and constraints required for the simulation of each equation of the developed mathematical model for Mg biodegradation.

### 3.3.5 Implementation

To simulate the developed mathematical model, which is comprised of Eqs. 3.10, 3.11, 3.12, 3.13, and 3.17, a combination of finite difference and finite element methods was used, leading to discrete forms of these equations, which were subsequently solved using appropriate linear solvers.

To discretize the temporal terms of the aforementioned parabolic PDEs, a first-order backward Euler finite difference scheme was used, whereas the spatial terms were converted to a weak form using a standard first-order finite

element scheme. Then, the open-source PDE solver FreeFEM [67] was used to implement the weak form and obtain a linear system of equations for each PDE. The obtained linear systems were solved in parallel using the HYPRE preconditioner [68] and the GMRES solver [69] via the open-source high-performance computing (HPC) toolkit PETSc [70]. Additionally, to increase the efficiency of the computation and decrease the simulation execution time, the computational mesh was decomposed and distributed among available computing resources using the interface of HPDDM package in FreeFEM [71]. The details of this implementation are presented in our previous work [65] as well as in the supplementary materials of this paper. A simple iterative solver based on the Newton method was also developed to solve Eq. 3.2 to obtain the value of  $\alpha$  parameter if it was required in the simulations.

The computational mesh was generated using a set of first-order tetrahedral elements and was adaptively refined on the metal-solution interface to increase the numerical accuracy of the simulation of the level set equation (Eq. 3.17). The Netgen mesh engine [72] in the SALOME platform [73] was used to generate the mesh.

Similar to the technique employed by Bajger et al. [55], the gradient of concentration of  $Mg^{2+}$  in Eq. 3.17 was calculated at a distance  $h$  in the normal direction from the interface, with  $h$  being the smallest element size of the mesh:

$$\nabla_n C = \frac{C(\mathbf{x} + h\mathbf{n}) - C(\mathbf{x} + 2h\mathbf{n})}{h} \quad \mathbf{x} \in \Omega \subset \mathbb{R}^3. \quad (3.19)$$

Considering the adaptively refined mesh, the  $h$  value is very small, so the gradient is computed at the regions close enough to the interface. In addition to this technique, the mass lumping feature of FreeFEM was used to prevent the oscillation of concentration values on the diffusive metal-medium interface.

### 3.3.6 Experimental setup

The degradation rate of CP Mg was evaluated based on the hydrogen evolution tests performed either in NaCl or SBF solutions with eudiometers. The composition of the electrolytes is shown in the following table (Table 3.1). 0.5 g metallic chips (with a surface area of  $47.7 \pm 5.0 \text{ cm}^2/\text{g}$  and chip thickness ca. 200 microns) of CP Mg were put in 500 ml electrolyte for 22-24 hours for monitoring the amount of evolved hydrogen. The method of measuring

evolved hydrogen was chosen for monitoring the degradation rate because although such a measurement is prone to experimental errors such as relatively high solubility of hydrogen in water and volume change due to temperature and pressure variations, it provides a continuous assessment of the process, resulting in a continuous and smooth curve. Additionally, as small metallic chips were used for the tests, it was not possible to clean these pieces in chromic acid without losing them to measure the mass loss directly. The drawback of choosing the evolved hydrogen as the monitoring method is that it is not the only occurring reaction since oxygen reduction also takes place during the process [43, 62, 38]. As a result, measuring only hydrogen does not capture the totality of the degradation reactions. However, for CP Mg, the contribution of oxygen reduction is low (in contrast to high-purity Mg [43]) and can simply be ignored, meaning that the evolved hydrogen is an accurate equivalent for the mass loss. The bulk pH of electrolytes before and after corrosion was measured by a pH meter (Metrohm-691, Switzerland). Local pH was measured by positioning pH microprobes (Unisense, Denmark, pH-sensitive tip size 10x50 micron) 50 micron above the surface of Mg and monitoring the pH values either in one spot or by horizontal or vertical line-scans or mapping by following a horizontal grid. The electrolytes were not pH buffered additionally since SBF contains carbonates and phosphates that stabilize the pH at the approximate value of 8.5 instead of the 10.5 characteristic for pure NaCl solutions where pH is stabilized by precipitation of  $Mg(OH)_2$ . Meanwhile, synthetic pH buffers, such as TRIS and HEPES were proven to affect the degradation mechanism rather significantly and should not be used for this purpose [21]. The measurements were performed at room temperature of  $22 \pm 2^\circ C$  maintained by the laboratory climate control system. More detailed information about experimental set up and procedures can be found elsewhere [22, 26].

### 3.3.7 Parameter estimation

The constructed mathematical model contains some parameters that need to be calibrated prior to final validation of the model: diffusion coefficient of  $Mg^{2+}$  and  $Cl^-$  ions ( $D_{Mg}$  and  $D_{Cl}$  to be inserted into Eq. 3.15 to get effective diffusion coefficients), the reaction rates of Eqs. 3.5 and 3.6 ( $k_1$  and  $k_2$ ), the momentum parameter,  $\beta$ , for controlling the saturation term behavior (in Eqs. 3.10, 3.11, and 3.15), and the  $\gamma$  parameter for the initial interface velocity (Eq.

Table 3.1: Chemical composition of NaCl and SBF electrolytes used to perform hydrogen evolution tests, weight loss, local and bulk pH measurements.

	Concentration/ mM	
	0.85 wt. % NaCl	SBF
Na <sup>+</sup>	145.4	142.0
K <sup>+</sup>	-	5.0
Mg <sup>2+</sup>	-	1.5
Ca <sup>2+</sup>	-	2.5
Cl <sup>-</sup>	145.4	147.8
HCO <sub>3</sub> <sup>-</sup>	-	4.2
HPO <sub>4</sub> <sup>2-</sup> / H <sub>2</sub> PO <sub>4</sub> <sup>-</sup>	-	1.0
SO <sub>4</sub> <sup>2-</sup>	-	4.2
Synthetic pH buffer (i.e. Tris/HCl, HEPES)	No	No
Initial pH value	5.6-5.9	7.35-7.45

3.18). An inverse problem setup was required to estimate the proper value of these parameters.

Performing a parameter estimation requires running the computational models several times. Considering the computationally-intensive model of the current study, a sensitivity analysis was performed prior to the parameter estimation to exclude non-essential parameters and reduce the time required to complete the inverse problem run. This sensitivity analysis was accomplished separately in the low diffusion (similar to the SBF solution) and high diffusion (similar to NaCl solution) regimes.

After determining the essential parameters to include, a Bayesian optimization approach [74] was used to construct the inverse problem and calibrate the parameters. The reason for choosing a Bayesian approach was to minimize the number of optimization iterations, in each of which the simulation should run once. The Bayesian optimization is a more efficient option for such computational intensive cases in comparison to gradient-based or fully-stochastic methods as it takes into account all the preceding iterations in a probability tree [75].

The objective function of the optimization problem was the difference between the predicted and experimentally obtained values of evolved hydrogen. In the computational model, the evolved hydrogen can be computed directly at any

time through the mass loss as each mole of corroded Mg is correlated to one mole of released hydrogen (Eq. 3.5). The mass loss can be obtained using the following volume integral:

$$\text{Mg}_{\text{lost}} = \int_{\Omega_+(t)} [\text{Mg}]_{\text{sol}} dV - \int_{\Omega_+(0)} [\text{Mg}]_{\text{sol}} dV, \quad (3.20)$$

where  $\Omega_+(t) = \{\mathbf{x} : \phi(\mathbf{x}, t) \geq 0\}$ , and then, the amount of produced hydrogen is calculated using the ideal gas law:

$$H_f = \frac{\text{Mg}_{\text{lost}}}{\text{Mg}_{\text{mol}}} \frac{RT}{P} \quad (3.21)$$

in which  $R$ ,  $P$ ,  $T$ ,  $\text{Mg}_{\text{mol}}$  are the universal gas constant, the pressure, the medium temperature, and the molar mass of Mg, respectively.

### 3.3.8 Simulation setup

In order to simulate the developed mathematical model, the experimental setup was reconstructed *in silico* with some minor differences. As there is no perfusion in the solution chamber, the mixing effect was neglected, so, as can also be seen in the mathematical model, the advection terms were not considered. Furthermore, the experiments were conducted using small metallic chips, yet, as the biodegradation behavior heavily depends on the exposed surfaces, we represented these chips by a cuboid with the same surface-to-mass ratio. By considering the approximate surface-to-mass of  $50\text{cm}^2/\text{g}$  and the total mass of  $0.5\text{g}$ , the chips were replaced by a cuboid with the size of  $60\text{mm} \times 21\text{mm} \times 0.2\text{mm}$ , which approximately has the same ratio, surface area, volume, and mass. Also, the solution chamber with a capacity of  $500\text{ml}$  was represented by a cubic container with an edge size of  $80\text{mm}$ . Fig. 3.3 depicts the constructed geometry as well as the computational mesh generated to represent it. The mesh is refined on the interface and contains 18,049,471 elements, resulting in 3,077,227 degrees of freedom (DOF) for each PDE.

Simulations were carried out on the VSC (Flemish Supercomputer Center) supercomputer. Taking advantage of HPC techniques to parallelize the simulation is an inevitable aspect of such a computational-intensive model, so based on what described in the implementation section, the mesh was decomposed among 170 computing cores, i.e. 24,137 DOF per core (which includes the

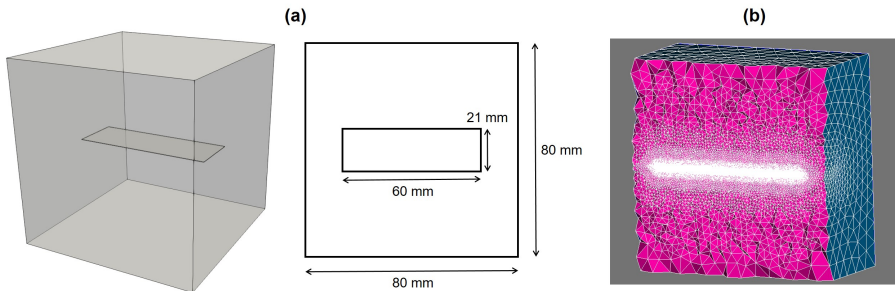


Figure 3.3: Computational representation of the experimental set-up, used to perform parameter estimation and numerical validation of the developed model. a) A cuboid of Mg ( $60\text{mm} \times 21\text{mm} \times 0.2\text{mm}$ ) inside a solution, b) a cross-section of the computational mesh, refined on the corrosion front to increase the required level set accuracy.

ghost nodes to satisfy the boundary condition in each sub-mesh). On the VSC supercomputer, we made use of 5 nodes, 36 cores each, each node holding CPUs with a clock speed of 2.6 GHz, with 960 GB of the total available memory.

The  $\text{OH}^-$  transport equation (Eq. 3.13) was not solved during the parameter calibration process. Afterwards, two full simulations (for the NaCl and SBF solutions) were conducted to calculate the pH changes based on the change of the concentration of  $\text{OH}^-$  ions in the medium. This acted as the validation of the numerical model because no calibration was performed on the output of this equation. The pH was calculated using Eq. 3.9, based on the solution of Eq. 3.13 and a reported value of  $7.00e \times 10^{-5}\text{cm}^2/\text{s}$  ( $25.2\text{mm}^2/\text{hour}$ ) for the diffusion coefficient of  $\text{OH}^-$  ions ( $D_{\text{OH}}$  to be used in Eq. 3.15) in aqueous solutions [76].

According to the experimental setup, the initial concentration of the  $\text{Mg}^{2+}$ ,  $\text{Cl}^-$ , and  $\text{OH}^-$  ions were set to 0 (no  $\text{Mg}^{2+}$  ions at the beginning), 146mM ( $5.175 \times 10^{-6}\text{g/mm}^3$ ), and  $1 \times 10^{-7}\text{g/mm}^3$ , respectively. The porosity ( $\epsilon$ ) and tortuosity ( $\tau$ ) of the protective film were considered to be 0.55 and 1, respectively [54]. The saturation concentration  $[\text{Mg}]_{\text{sat}}$  was set to the solubility of magnesium chloride in water, which is  $134 \times 10^{-6}\text{g/mm}^3$  at  $25^\circ\text{C}$  [77]. The density of Mg ( $[\text{Mg}]_{\text{sol}}$ ) and  $\text{Mg}(\text{OH})_2$  were set to  $1735 \times 10^{-6}\text{g/mm}^3$  and  $2344 \times 10^{-6}\text{g/mm}^3$ , respectively [55]. A time step convergence study was performed to determine the implicit time step size. Based on the results, a time step with a size of 0.025 hours was chosen. The overall simulated time is 22

hours in accordance with the experimental design of performed immersion tests.

### 3.3.9 Case study

To further investigate the predictions of the current model on more complex shapes, the biodegradation of a simple screw was studied in the SBF solution using the parameters obtained for the low diffusion regimes. Similar to the simulation of Mg cuboid, the mesh was refined on the metal-medium interface, and it consisted of 1,440,439 elements with 246,580 DOFs for each PDE. All the simulation parameters and materials properties were identical to the simulation of biodegradation in the SBF solution, and the target was to simulate 42 days (1008 hours) of the process. This was selected as a sufficiently long simulated time to observe the effects of biodegradation on larger time scales.

## 3.4 Results

### 3.4.1 Optimization results

Based on the performed sensitivity analysis, two parameter sets were obtained for the high diffusion (in NaCl solution) and low diffusion (in SBF solution) simulations, respectively. These parameters are listed in Table 3.2. According to the results, the reaction rate of Eq. 3.5 ( $k_1$ ), which demonstrates the rate of oxidation-reduction, has less contribution to the process in comparison to the rate of the weakening of the protective film ( $k_2$ ). Because of this, the parameter  $k_1$  was not selected for the parameter estimation. Also, the model was sensitive to the effect of parameter  $k_2$  in different ranges of values and not on a specific point, and as a result, three constant values were chosen as the delegates of these ranges in the optimization process. The model was not sensitive to the diffusion rate of  $\text{Cl}^-$  ions, which was also expected because although  $\text{Cl}^-$  has an important role in the weakening of the partially protective  $\text{MgO}$  film, its transport equation (Eq. 3.12) is purely diffusive and does not include any reaction term.

Table 3.2: The effective parameters as the result of the sensitivity analysis and their corresponding range to be considered in the Bayesian optimization for parameter calibration

	Parameter	Optimization range
Low diffusion (SBF solution)	$D_{\text{Mg}}$	[0.0001, 0.01]
	$k_2$	$10^{10}, 10^{15}, 10^{20}$
	$\beta$	[0.1, 10]
	$\gamma$	[0, 1]
High diffusion (NaCl solution)	$D_{\text{Mg}}$	[0.003, 0.1]
	$k_2$	$10^{10}, 10^{15}, 10^{20}$
	$\beta$	[0.1, 10]

Table 3.3: Values used to evaluate the model performance, obtained from the output of the optimization process and the literature.

Parameter	$D_{\text{Mg}}$	$D_{\text{Cl}}$	$D_{\text{OH}}$	$k_1$	$k_2$	$\beta$	$\gamma$
Unit	$\frac{\text{mm}^2}{\text{hour}}$	$\frac{\text{mm}^2}{\text{hour}}$	$\frac{\text{mm}^2}{\text{hour}}$	$\frac{1}{\text{hour}}$	$\frac{\text{mm}^6}{\text{g}^2 \text{hour}}$	-	-
SBF solution	0.000338	0.05	25.2	7	$10^{15}$	0.125	0.65
NaCl solution	0.06273	0.05	25.2	7	$10^{20}$	0.2	0

The parameter optimization process was performed on the specified range of selected parameters, while the rest of the parameter values were obtained from the literature [55, 76]. Table 3.3 shows the output of this process, which was used to simulate the full model. For two estimation processes, 120 optimization iterations were taken cumulatively, which took 276 hours of simulation execution time using 170 computing nodes for each simulation.

### 3.4.2 Degradation prediction

Fig. 3.4 shows the model output for the predicted produced hydrogen, protective film formation, and the pH changes. The graph of the evolved hydrogen is used as input during the parameter optimization process, but the pH results are produced by the simulations using the optimized parameters to demonstrate the validation of the developed mathematical and computational models. The predicted pH result (Fig. 3.4-d) shows a difference of 5.35% for the simulation in NaCl and 1.03% for SBF simulation. Each simulation took about 3 hours to complete.

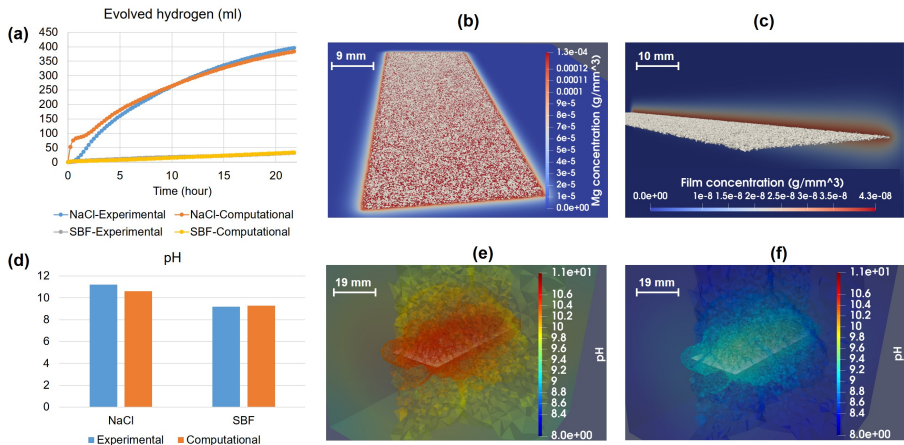


Figure 3.4: Comparing the quantitative output of the model for the rate of degradation and the pH changes in NaCl and SBF solutions with experimentally measured values as well as the simulation results for ion release, mass loss, protective film formation, and pH changes after 22 hours of simulated time: a) calibrated output of the formed hydrogen gas during the degradation (the SBF curves are overlapped), b) the simulation results of Mg<sup>2+</sup> ions release, c) the simulation results of protective film concentration at the end of the simulation (the color contour shows the concentration of species, and the gray surface is the zero iso-contour of the level set function, which indicates the surface of the Mg block), d) de novo prediction of the global pH changes in the medium, showing a good agreement between the model output and the experimental results, e) pH changes in different regions of the medium in NaCl solution, f) pH changes in SBF solution.

In Fig. 3.4, a post-processed view of the final shape of the Mg cuboid in the NaCl solution is presented, in which the degraded geometry is plotted on the Mg<sup>2+</sup> ions (Fig. 3.4-b) and protective film concentration (Fig. 3.4-c) contours. A transparent contour of the pH values in the solution is depicted for both the NaCl (Fig. 3.4-e) and SBF (Fig. 3.4-f) solutions. The range of colors is kept equal for both contours to make it easy to compare the change of pH in both solutions.

The concentration values of the state variables of the derived transport PDEs (Mg<sup>2+</sup>, Cl<sup>-</sup>, OH<sup>-</sup>, and Mg(OH)<sub>2</sub>) are plotted along a diagonal line in the solution container in Fig. 3.5, showing how they change in the zones close to

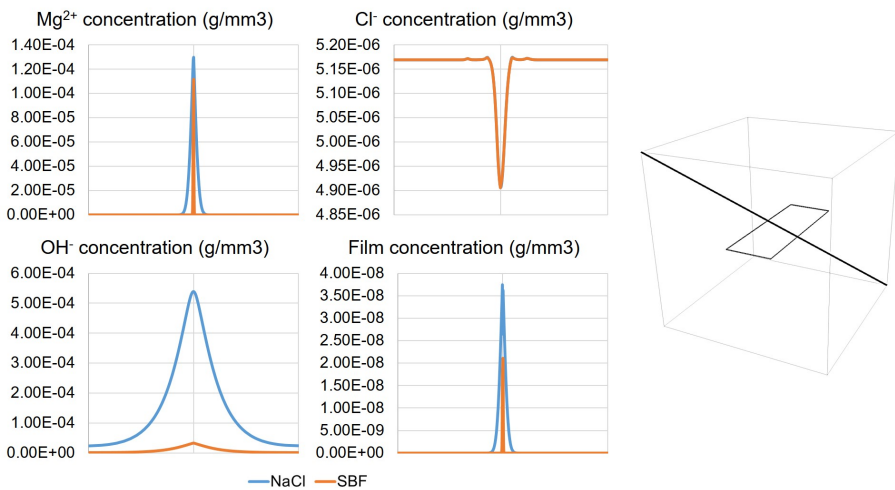


Figure 3.5: The change of concentration for the involved chemical components,  $Mg^{2+}$ ,  $Cl^-$ ,  $OH^-$  ions, and the protective precipitation structure (which can be correlated to the thickness of the layer) plotted over a diagonal line as shown in the right.

the corrosion surface and far from it. The animated output of the degradation of the Mg cuboid is presented as a set of movie files in the supplementary materials of this paper (post-processed using NVIDIA IndeX software on a GPU).

### 3.4.3 Example application

The simulation of 42 days (19,200 time steps) of the degradation of the simple screw took 9 hours to run using 170 computing cores. Fig. 3.6 depicts the post-processed interface and  $Mg^{2+}$  ions release (similar to Fig. 3.4-b) as well as the mass loss during the degradation of the screw in the SBF solution.

## 3.5 Discussion

In this study, a physicochemical model of the biodegradation process of commercially-pure Mg was developed by constructing a mathematical model

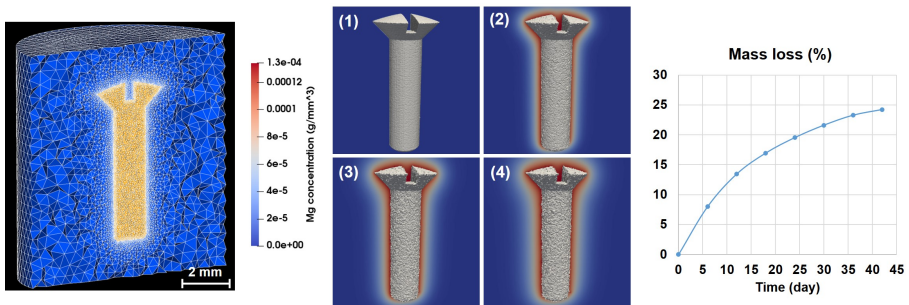


Figure 3.6: A cross-section of the computational mesh and simulation results of the degradation process of the use-case screw in SBF solution as well as the mass loss graph over time. The contours display the concentration of  $Mg^{2+}$  ions on a cross-section view of the medium beside the moving surface of the screw at 1) 1st day (initial state), 2) 6th day, 3) 12th day, and 4) 18th day.

formulating the mass transfer phenomena as well as tracking the location of the surface of the implant during degradation. For the mass transfer model, the equations were derived from the chemistry of biodegradation of the Mg in saline (NaCl) and buffered (SBF) solutions, which includes the oxidation of the metallic part, reduction of water, changes in pH, and formation of a protective film on the surface of the scaffold which contributes to a slower rate of degradation. Beside these aspects, it was also crucial to consider the effect of different ions in the medium on the rate of degradation. Additionally, investigating the structural changes of the scaffolds and implants in practical applications, like resorption of temporary fixation devices, requires tracking the movement of the corrosion surface. This was done by constructing an equation based on the level set principle, which captured the movement of the medium-metal interface by defining an implicit surface. The derived equations were coupled and solved using a combination of finite difference and finite element methods. The degradation data to validate the models was collected from immersion tests of small Mg chips, reconstructed as a single cuboid in the computational study with a similar surface over volume properties. The model parameters were calibrated using a Bayesian optimization algorithm, and the obtained parameters were used to simulate the pH changes in NaCl and SBF solutions.

The developed model falls in the categories of physical models of the corrosion process, which provide more insights of the process in comparison to the

phenomenological models. The reason is that the phenomenological models focus on the elimination of elements to capture the loss of materials, which makes it impossible to model the formation of new chemical compounds or interaction of species [78]. The physical models, like the one developed in this study, are capable of capturing the underlying chemical interactions. By doing this, processes like the effect of coating, the formation of a protective layer, and pH changes can be modeled. Adding an appropriate interface tracking method enables the physical models to act like the phenomenological models in capturing the corrosion interface movement. In the current study, this has been accomplished using a level set function. Technically speaking, this approach has certain benefits over the ALE method, which is the method used by several similar studies, including Grogan et al. [50]. In comparison to the ALE method, the level set function tracks the interface instead of a Lagrangian mesh, and elements can freely be marked as solid or liquid. Additionally, employing the ALE method for degradation simulation requires remeshing the geometry as the interface moves, which is not efficient for 3D models and is limited to the available features of the employed numerical solver.

One of the challenging aspects of validating physical models is getting the correct value for the parameters of said models, requiring dedicated experimental input. To overcome this challenge, an efficient inverse problem was constructed based on the Bayesian optimization approach to estimate the unknown parameters. To save time and resources, the parameter estimation process was performed on the most effective parameters, which were selected based on a sensitivity analysis. This selection process implied the importance of parameters in high and low diffusion rates.

The degradation rate is fast at the beginning, but then it slows down due to the formation of a partially protective film and also because of the saturation concentration. This phenomenon is well captured by the model at high diffusion rates, but in low diffusion rates (in SBF solution), this effect can be reproduced by pushing the corrosion front according to the Stefan formulation of the moving interface problems. This was controlled by the parameter  $\gamma$  (Eq. 3.18). It should be noted that the inclusion of the  $\gamma$  parameter is crucial for short-term simulations only, helping the model mimic the chemical behavior correctly. Defining and considering  $\gamma$  is necessary because from the computational costs perspective, performing the parameter calibration on simulations with thousands of time steps requires a lot more resources and time. For the high diffusion regime simulation, the results show a difference

between the experimental and computational data in the early stages of the degradation process (Fig. 3.4-a). The reason for this behavior lies within Eqs. 3.17 and 3.19, in which the interface velocity was correlated to the gradient of released ions. In high diffusion rates, the material release occurs very fast, so the calculated gradient (Eq. 3.19) vanishes for a short period until the diffusion becomes more uniform. As a result, the interface does not move, and according to Eq. 3.20, no mass loss gets calculated. This effect was automatically ignored in the parameter estimation process since the objective function considers the overall degradation behavior.

The degradation of the CP Mg was assumed to be mostly diffusion-based. As a result, the value of  $D_{Mg}$  plays an important role in the behavior of the model. Although it was possible to get the diffusion coefficient of  $Mg^{2+}$  from the previously conducted experiments in the literature (similar to what was done for  $D_{OH^-}$ ), we decided to not do so because of two reasons: 1) the values reported in the literature are mostly valid for saline solutions only, and 2) the reported values were not in a good agreement with one another [50, 54]. Thus, the diffusion coefficient was obtained using the parameter estimation process for both the NaCl and SBF solutions. The obtained value of  $D_{Mg}$  ( $0.06273\text{mm}^2/\text{hour}$ ) was in line with the values that Grogan et al. have already suggested ( $0.010575 - 0.50575\text{mm}^2/\text{hour}$ ) [50], showing that the constructed inverse problem was successful in reproducing previous results of similar studies. The obtained value of  $D_{Mg}$  in the Bajger et al. work [55] is  $0.00066\text{mm}^2/\text{hour}$ , which is mostly related to the simplicity of the employed parameter estimation method as well as having a 2D model instead of a 3D one.

In the *in vitro* biodegradation of Mg-based biomaterials, the local pH of the surrounding solution increases less than that in NaCl solution. This is because the  $Mg(OH)_2$  formed in NaCl stabilizes pH at 10.4 [79], while Mg-Ca-P-C containing products stabilize the pH at 7.8-8.5 since  $OH^-$  is consumed for the formation of this product [25, 22]. This phenomenon was captured in Eqs. 3.13 and 3.9 to calculate pH based on the concentration of  $OH^-$  ions, showing the local pH changes at any location (Fig. 3.4-e,f). In the current study, the global pH is considered as the validation criterion, which means that the average value of the solution pH is calculated using a volume integral and is compared with the ones obtained from the experiments. Fig. 3.4-d shows that such a prediction has a good agreement with the experimental data.

One of the biggest simplifications of the current study was made by ignoring

the contribution of pH changes to the biodegradation mechanism of Mg. Although doing that is relatively simple and straightforward in the approach taken by this study, it results in non-linear terms in the derived PDEs. This non-linearity inserts another level of complexity to the computational model as the order of the state variables are in the range of  $10^{-6}$  to  $10^{-10}$ , which makes it difficult to yield convergence in the iterative non-linear solvers. By developing a robust non-linear solver, this effect can be added simply by including more relevant terms as the effect of Eq. 3.13 into Eq. 3.10.

Additionally, buffered solutions and the physiological fluids inside the human and animal bodies contain more ions interacting with more complex chemistry [21]. In this study, this effect was encapsulated in a limited number of parameters (such as  $k_1$  and  $k_2$  in Eqs. 3.10, 3.11, and 3.13), but while the results show its success to reproduce experimental observations, it still needs additional elaboration to be able to capture more chemical interactions. For Example, SBF solutions contain phosphates, carbonates, and calcium that form hydroxyapatite-like compounds on the surface of Mg, acting as rather strongly blocking corrosion products. In the current state of the developed model, such an effect on the corrosion rate was captured by a low effective diffusion coefficient (Eq. 3.15) for the Mg transport. In future model developments, the effect of presented inorganic ions such as  $\text{HCO}_3^-$ ,  $\text{HPO}_4^{2-}/\text{H}_2\text{PO}_4^-$ , and  $\text{Ca}^{2+}$  can be added similar to the way the effect of  $\text{Cl}^-$  was considered. Additionally, formulating the effect of  $\text{HPO}_4^{2-}$  that exists in the physiological environments will make the model capable of making more accurate predictions for *in vivo* studies.

A common approach in mechanistic studies is to start with a pure material and gradually increasing complexity by adding impurities and alloying elements. This approach was followed in the current study by beginning with a model for pure Mg that captures the major reactions. The developed model can be further extended to Mg alloys by considering the effect of alloying elements on the reaction rates as well as adding more terms to the transport equations to capture the electrochemical potential changes, converting the PDEs into the NernstPlanck equation [80]. By doing so, more complex forms of the corrosion process, such as galvanic corrosion, can be predicted by the model. This will increase the applicability of the model for biomedical cases since pure Mg is not commonly used for medical-graded applications. As an additional future development, the corrosion layer can be considered to be heterogeneous, making it possible to simulate the cathodic reactions by randomly distributing

more active spots on the surface. Alternatively, a similar effect can be achieved by adapting the degradation rates using polarization curves and introducing an active spot for inhomogeneous anodic dissolution [81]. Applying this will enable the model to take into account additional corrosion products formed due to additional alloying elements such as Zn, Ca, Ag, rare-earth elements, and detrimental cathodic impurities such as Fe.

Although the pH simulations are not enough experimental input to call the model fully validated, the obtained validation results show that the derived mathematical model and the corresponding parallelized computational model give a correct *in silico* representation of the studied process. The performed predictive simulations, including the case study, demonstrate the potential of the developed computational model and software to study the biodegradation behavior of implants. This can be further combined with other computational models to provide a multidisciplinary environment to investigate the mechanical integrity of implants or induced neotissue growth for different applications in orthopedics and tissue engineering.

### 3.6 Conclusions

The use of biodegradable metals for designing medical devices and implants has the challenge of controlling the release and rate of degradation, which is usually investigated by conducting *in vitro* and *in vivo* tests requiring conducting multiple experiments for different scenarios and situations. In this study, we have developed a mathematical model to predict the biodegradation behavior of commercially pure Mg-based biomaterials, which makes it possible to study the corrosion of implants and scaffolds in a simulated environment. Despite the assumed simplifications, the model can serve as an important tool to find the biodegradable metals properties and predict the biodegradation behavior of Mg-based implants that improves current design workflows.

### Acknowledgment

This research is financially supported by the Prosperos project, funded by the Interreg VA Flanders The Netherlands program, CCI grant no. 2014TC16RFCB046 and by the Fund for Scientific Research Flanders (FWO), grant G085018N.

LG acknowledges support from the European Research Council under the European Union's Horizon 2020 research and innovation programme, ERC CoG 772418. The computational resources and services used in this work were provided by the VSC (Flemish Supercomputer Center), funded by the Research Foundation - Flanders (FWO) and the Flemish Government department EWI.



# Chapter 4

## Fluid flow and convection

### 4.1 Introduction

### 4.2 Methodology

#### 4.2.1 Navier-Stokes equations

In its general form, the Navier-Stokes equations describing the flow of an incompressible fluid with constant density  $\rho$  in the domain  $\Omega \subset \mathbb{R}^d$  (with  $d$  being the dimension so 2 or 3) can be written as [82]:

$$\begin{cases} \frac{\partial \mathbf{u}}{\partial t} - \nabla \cdot [\nu(\nabla \mathbf{u} + \nabla \mathbf{u}^T)] + (\mathbf{u} \cdot \nabla) \mathbf{u} + \nabla p = \mathbf{f}, & x \in \Omega, t > 0, \\ \nabla \cdot \mathbf{u} = 0, & x \in \Omega, t > 0, \end{cases} \quad (4.1)$$

in which  $\mathbf{u}$  is the fluid velocity,  $p$  is the pressure (which is actually pressure divided by the density),  $\nu = \frac{\mu}{\rho}$  is the kinematic viscosity (with  $\mu$  being the dynamic viscosity), and  $\mathbf{f}$  is a force term. The equations are that of conservation of linear momentum and conservation of mass (also called continuity equation), respectively. When  $\nu$  is constant, the diffusion term in Eq. 4.1 can be simplified as [83]:

$$\text{div}[\nu(\nabla \mathbf{u} + \nabla \mathbf{u}^T)] = \nu(\Delta \mathbf{u} + \nabla \text{div} \mathbf{u}) = \nu \Delta \mathbf{u}, \quad (4.2)$$

which turns Eq. 4.1 into the following form:

$$\begin{cases} \frac{\partial \mathbf{u}}{\partial t} - \nu \Delta \mathbf{u} + (\mathbf{u} \cdot \nabla) \mathbf{u} + \nabla p = \mathbf{f}, & x \in \Omega, t > 0, \\ \nabla \cdot \mathbf{u} = 0, & x \in \Omega, t > 0, \end{cases} \quad (4.3)$$

Eq. 4.3 satisfies the incompressibility condition  $\nabla \cdot \mathbf{u} = 0$  and needs proper initial and boundary conditions to be well posed. The initial condition can be defined as:

$$\mathbf{u}(\mathbf{x}, 0) = \mathbf{u}_0(\mathbf{x}) \quad \forall \mathbf{x} \in \Omega, \quad (4.4)$$

where  $\mathbf{u}_0$  is a divergence-free fluid field. Various types of boundary conditions can be applied, but the ones we deal with in this chapter are described here. If  $\partial\Omega$  is the boundary of  $\Omega$ , it can be split into 3 distinct boundaries  $\partial\Omega = \Gamma_1 \cup \Gamma_2 \cup \Gamma_3$  each of which with a different type. On  $\Gamma_1$ , the inlet can be defined as a Dirichlet boundary condition for the velocity for a given velocity profile  $\mathbf{g}$ :

$$\mathbf{u} = \mathbf{g} \quad \text{on } \Gamma_1 \quad (4.5)$$

On  $\Gamma_2$ , a wall boundary no-slip condition can be considered:

$$\mathbf{u} = 0 \quad \text{on } \Gamma_2 \quad (4.6)$$

On  $\Gamma_3$ , for the outlet condition, a homogeneous Neumann conditions on velocity and a zero pressure condition can be defined like:

$$\frac{\partial \mathbf{u}}{\partial n} = 0, \quad p = 0, \quad \text{on } \Gamma_3 \quad (4.7)$$

with  $n$  being the normal direction on the boundary  $\partial\Omega$ . Broadly speaking, these boundaries can be grouped into 2 sets:  $\Gamma_D = \Gamma_1 \cup \Gamma_2$  and  $\Gamma_N = \Gamma_3$  for boundaries with Dirichlet and Neumann conditions, respectively.

The Navier-Stokes equations can be written componentwise for individual components of the flow vector field in the Cartesian coordinates. Denoting  $u_i, i = 1, \dots, d$  (with  $d = 2$  in 2D and  $d = 3$  in 3D), Eq. 4.3 can be presented as:

$$\begin{cases} \frac{\partial u_i}{\partial t} - \nu \Delta u_i + \sum_{j=1}^d u_j \frac{\partial u_i}{\partial x_j} + \frac{\partial p}{\partial x_i} = f_i, & i = 1, \dots, d, \\ \sum_{j=1}^d \frac{\partial u_j}{\partial x_j} = 0. \end{cases} \quad (4.8)$$

#### 4.2.2 Weak formulation of the Navier-Stokes equations

For deriving the weak formulation, the first equation of 4.3 is multiplied by a test function  $v$  defined on a proper function space  $V$  in which the test functions vanishes on the Dirichlet boundary:

$$V = [\mathbf{H}_{\Gamma_D}^1(\Omega)]^d = \{\mathbf{V} \in [\mathbf{H}^1(\Omega)]^d : \mathbf{v}|_{\Gamma_D} = \mathbf{0}\}. \quad (4.9)$$

yielding to:

$$\int_{\Omega} \frac{\partial \mathbf{u}}{\partial t} \cdot \mathbf{v} d\omega - \int_{\Omega} \nu \Delta \mathbf{u} \cdot \mathbf{v} d\omega + \int_{\Omega} [(\mathbf{u} \cdot \nabla) \mathbf{u}] \cdot \mathbf{v} d\omega + \int_{\Omega} \nabla p \cdot \mathbf{v} d\omega = \int_{\Omega} \mathbf{f} \cdot \mathbf{v} d\omega. \quad (4.10)$$

Applying Green's divergence theory results in:

$$-\int_{\Omega} \nu \Delta \mathbf{u} \cdot \mathbf{v} d\omega = \int_{\Omega} \nu \nabla \mathbf{u} \cdot \nabla \mathbf{v} d\omega - \int_{\partial\Omega} \nu \frac{\partial \mathbf{u}}{\partial \mathbf{n}} \cdot \mathbf{v} d\gamma \quad (4.11)$$

and

$$\int_{\Omega} \nabla p \cdot \mathbf{v} d\omega = - \int_{\Omega} p \nabla \cdot \mathbf{v} d\omega + \int_{\partial\Omega} p \mathbf{v} \cdot \mathbf{n} d\gamma \quad (4.12)$$

Substituting Eqs. 4.11 and 4.12 into Eq. 4.10 yields to:

$$\begin{aligned} \int_{\Omega} \frac{\partial \mathbf{u}}{\partial t} \cdot \mathbf{v} d\omega + \int_{\Omega} \nu \nabla \mathbf{u} \cdot \nabla \mathbf{v} d\omega + \int_{\Omega} [(\mathbf{u} \cdot \nabla) \mathbf{u}] \cdot \mathbf{v} d\omega - \int_{\Omega} p \nabla \cdot \mathbf{v} d\omega \\ = \int_{\Omega} \mathbf{f} \cdot \mathbf{v} d\omega + \int_{\partial\Omega} \left( \nu \frac{\partial \mathbf{u}}{\partial \mathbf{n}} - p \mathbf{n} \right) \cdot \mathbf{v} d\gamma \quad \forall \mathbf{v} \in V. \end{aligned} \quad (4.13)$$

The last term of Eq. 4.13 is expressed in accordance to the defined Neumann boundary condition, which vanishes on  $\Gamma_3$  due to the defined condition in the current study (Eq. 4.7). Moreover, this term vanishes on the Dirichlet boundaries due to the properties of the function space  $V$  (Eq. 4.9).

Similarly, the second equation of 4.3 is multiplied by a test function  $q$  belonging to the function space  $Q$ , called the pressure space:

$$Q = \mathbf{L}_0^2(\Omega) = \{p \in L^2(\Omega) : \int_{\Omega} p \, d\omega = 0\}, \quad (4.14)$$

resulting in:

$$\int_{\Omega} q \nabla \cdot \mathbf{u} \, d\omega = 0 \quad \forall q \in Q. \quad (4.15)$$

Eqs. 4.13 and 4.15 are so called weak forms of the Navier-Stokes equations.

### 4.2.3 Stokes equations

For viscous flow, where the Reynolds number is less than 1 ( $Re = \frac{|\mathbf{U}|L}{\nu}$ , with  $L$  and  $\mathbf{U}$  being the representative length and velocity of the domain), the convection term of the Navier-Stokes equations can be neglected, simplifying Eq. 4.3 to [83]:

$$\begin{cases} \alpha \mathbf{u} - \nu \Delta \mathbf{u} + \nabla p = f & \text{in } \Omega, \\ \nabla \cdot \mathbf{u} = 0 & \text{in } \Omega, \end{cases} \quad (4.16)$$

with  $\alpha$  being a positive coefficient. Eq. 4.16 can be used to model laminar flow in low Reynolds regimes and is simpler to handle than Eq. 4.3 from the numerical computing perspective. The weak formulation of the Stokes equation can be derived by following the approach taken for the Navier-Stokes equations in Section 4.2.2. The final form of the weak formulation is:

$$\begin{cases} \int_{\Omega} (\alpha \mathbf{u} \cdot \mathbf{v} + \nu \nabla \mathbf{u} \cdot \nabla \mathbf{v}) \, d\omega - \int_{\Omega} p \nabla \cdot \mathbf{v} \, d\omega = \int_{\Omega} \mathbf{f} \cdot \mathbf{v} \, d\omega & \forall \mathbf{v} \in V, \\ \int_{\Omega} q \nabla \cdot \mathbf{u} \, d\omega = 0 & \forall q \in Q, \end{cases} \quad (4.17)$$

Eq. 4.17 can be written in the standard finite element variational form by defining 2 bilinear terms  $a : V \times V \mapsto \mathbb{R}$  and  $b : V \times Q \mapsto \mathbb{R}$ :

$$\begin{aligned} a(\mathbf{u}, \mathbf{v}) &= \int_{\Omega} (\alpha \mathbf{u} \cdot \mathbf{v} + \nu \nabla \mathbf{u} \cdot \nabla \mathbf{v}) d\omega, \\ b(\mathbf{u}, \mathbf{q}) &= - \int_{\Omega} q \nabla \cdot \mathbf{u} d\omega, \end{aligned} \quad (4.18)$$

which causes the variational problem of the Stokes equation becomes to find  $(\mathbf{u}, p) \in V \times Q$  such that

$$\begin{cases} a(\mathbf{u}, \mathbf{v}) + b(\mathbf{v}, p) = (\mathbf{f}, \mathbf{v}) & \forall \mathbf{v} \in V, \\ b(\mathbf{u}, \mathbf{q}) = 0 & \forall \mathbf{q} \in Q, \end{cases} \quad (4.19)$$

in which

$$(\mathbf{f}, \mathbf{v}) = \sum_{i=1}^d \int_{\Omega} f_i v_i d\omega. \quad (4.20)$$

#### 4.2.4 Implementation

Numerical implementation of the Stokes (Eq. 4.16) and Navier-Stokes (Eq. 4.16) equations can be tricky due to presence of certain sources of instability, which highly depends on the type of studied fluid regime [84, 85]. Various numerical models have presented for dealing with these equations, some of which are commonly used in CFD applications, such as the Newton-Raphson approximation of Navier-Stokes equataions and the Chorin's projection method.

In order to increase the stability and avoid some problems on the mathematical analysis of the numerical models (V-ellipticity property), a pseudo-compressibility assumption can be added to the continuity equation. The pseudo-compressible approximation appears as a pressure term  $\varepsilon p$  with  $\varepsilon$  being a very small coefficient, resulting to the following equation as the final form of the Navier-Stokes equations we consider in this study [86]:

$$\begin{cases} \frac{\partial \mathbf{u}}{\partial t} - \nu \Delta \mathbf{u} + (\mathbf{u} \cdot \nabla) \mathbf{u} + \nabla p = \mathbf{f}, \\ \nabla \cdot \mathbf{u} + \varepsilon p = 0. \end{cases} \quad (4.21)$$

Similarly, the Stokes equation can be written as:

$$\begin{cases} \alpha \mathbf{u} - \nu \Delta \mathbf{u} + \nabla p = \mathbf{f}, \\ \nabla \cdot \mathbf{u} + \varepsilon p = 0. \end{cases} \quad (4.22)$$

Another challenging part is to approximate the convection terms in the equations. One of the best approaches to do so is to take advantage of the method of characteristics, in which the characteristics curves of a PDE are used to convert it to an ODE, resulting to a simpler solution. By using the method of characteristics for the convection term and a backward Euler discretization for the temporal term, the weak form of the Navier-Stokes and continuity equations (Eq. 4.13 and 4.15) can be rewritten as:

$$\begin{aligned} \int_{\Omega} \frac{\mathbf{u}^{n+1} - \mathbf{u}^n \circ X^n}{\Delta t} \cdot \mathbf{v} d\omega + \nu \int_{\Omega} \nabla \mathbf{u}^{n+1} \cdot \nabla \mathbf{v} d\omega - \int_{\Omega} p^{n+1} \nabla \cdot \mathbf{v} d\omega &= \int_{\Omega} \mathbf{f} \cdot \mathbf{v} d\omega \\ \int_{\Omega} \nabla \cdot \mathbf{u}^{n+1} q d\omega + \varepsilon \int_{\Omega} p^{n+1} q d\omega &= 0 \end{aligned} \quad (4.23)$$

in which  $(\mathbf{u}^{n+1}, p^{n+1})$  are unknowns to be computed from the known state  $\mathbf{u}^n$  coming from the previous time step or the initial condition. In Eq. 4.23, the term  $\mathbf{u}^{n+1} - \mathbf{u}^n \circ X^n$  is corresponding to the convection term being approximated using the method of characteristics.

The weak form of the Stokes equations stays almost the same as Eq. 4.17 (because it doesn't contain transient and convection terms) but needs a slight modification to add the pseudo-compressible terms from Eq. 4.22:

$$\begin{aligned} \int_{\Omega} (\alpha \mathbf{u} \cdot \mathbf{v} + \nu \nabla \mathbf{u} \cdot \nabla \mathbf{v}) d\omega - \int_{\Omega} p \nabla \cdot \mathbf{v} d\omega &= \int_{\Omega} \mathbf{f} \cdot \mathbf{v} d\omega, \\ \int_{\Omega} q \nabla \cdot \mathbf{u} d\omega + \varepsilon \int_{\Omega} p q d\omega &= 0. \end{aligned} \quad (4.24)$$

Eqs. 4.23 and 4.24 can be easily implemented in FreeFEM thanks to the built-in support of the method of characteristics via the `convect` function. The model is implemented using P1 elements for the pressure and P2 elements for the velocity state variables.

#### 4.2.5 Considering the degrading object

In biodegradation simulations, a degrading object exists in the fluid domain, through which the flow should not pass because it is a solid part. One common approach to handle this situation is to remove the solid part from the fluid flow mesh, but since the part shrinks over time, this is not a feasible and efficient approach, needing tremendous mesh recreation and removal during simulation. As a result, in the current study, presence of the solid body as a barrier is taken into account by adding a Darcy term for the permeability to the Navier-Stokes and Stokes and equations. A penalization technique is then employed to implement it in the weak formulation. To couple the fluid flow model with the biodegradation model, a convection term is added to the ions transport equations, causing the ions be advected by the fluid velocity field.

Adding the Darcy term to Eq. 4.16 and considering no other acting force yields to:

$$-\nu \Delta \mathbf{u} + \nabla p + \frac{\nu}{K} \mathbf{u} = 0, \quad (4.25)$$

where  $K$  is the permeability function. The Darcy term vanishes in regions with high permeability, i.e. inside the fluid domain, resembling the Stokes equation, but when  $K$  is very small, i.e. inside the solid part, it dominates the flow and acts like a barrier. To avoid numerical perturbation for switching between these 2 regions, a heaviside function is defined to update  $K$  [87]:

$$H(\phi) = \begin{cases} 0, & \phi < -\varepsilon \\ \frac{1}{2} + \frac{\phi}{2\varepsilon} + \frac{1}{2\pi} \sin\left(\frac{\pi\phi}{\varepsilon}\right), & -\varepsilon < \phi < \varepsilon \\ 1, & \phi > \varepsilon \end{cases} \quad (4.26)$$

in which  $\phi$  is the level-set signed distance function used to separate the solid and solution parts (Eqs. 3.3 and 3.4), and  $\varepsilon$  is set to  $1.5h$ , with  $h$  being the minimum mesh element size. Then,  $K$  can be accordingly updated to have smooth transition between regions with big difference in permeability:

$$K(\mathbf{x}) = 10^{30}(1 - H) + K_0 H \quad (4.27)$$

where  $K_0$  is the permeability of metals in fluid regions ( $\sim 10^{-6}$  H/m). Similar to Eq. 4.25 the effect of the solid part can be added to the Navier-Stokes

equation (Eq. 4.3) by the Darcy term, leading to the following equation:

$$\frac{\partial \mathbf{u}}{\partial t} - \nu \Delta \mathbf{u} + (\mathbf{u} \cdot \nabla) \mathbf{u} + \nabla p + \frac{\nu}{K} \mathbf{u} = 0. \quad (4.28)$$

### 4.2.6 Simulation setup

#### Test case to compare with OpenFOAM

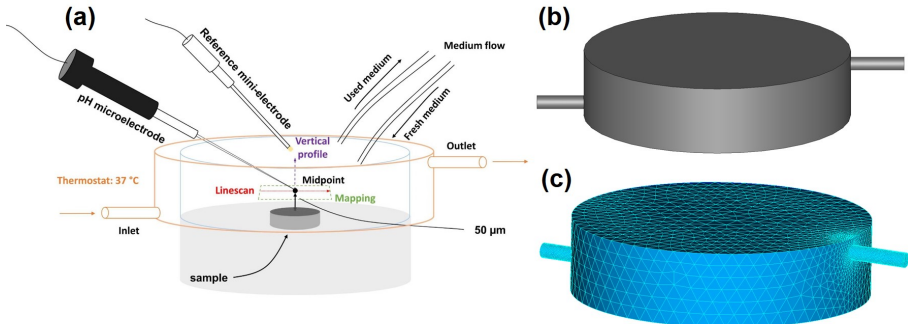


Figure 4.1: Fluid flow model construction for comparison with experimental setup

#### Test case to check coupling with degradation model

### 4.3 Results and discussion

To verify the robustness of the model predictions, the results of the CFD code was compared both quantitatively and qualitatively with an identical OpenFOAM model. The qualitative comparison is made via the streamlines, showing how the flow develops via drawing the trajectory lines of the fluid velocity field inside the domain of desired, which is the chamber in this case. Figs. 4.2 and 4.3 demonstrate such comparison between the developed model and OpenFOAM. Fig. 4.2 shows the streamlines for both model from a side view, in which the flow enters the chamber from the left inlet pipe and leaves it

from the top right outlet. The qualitative comparison shows a good agreement between the predictions of the models.

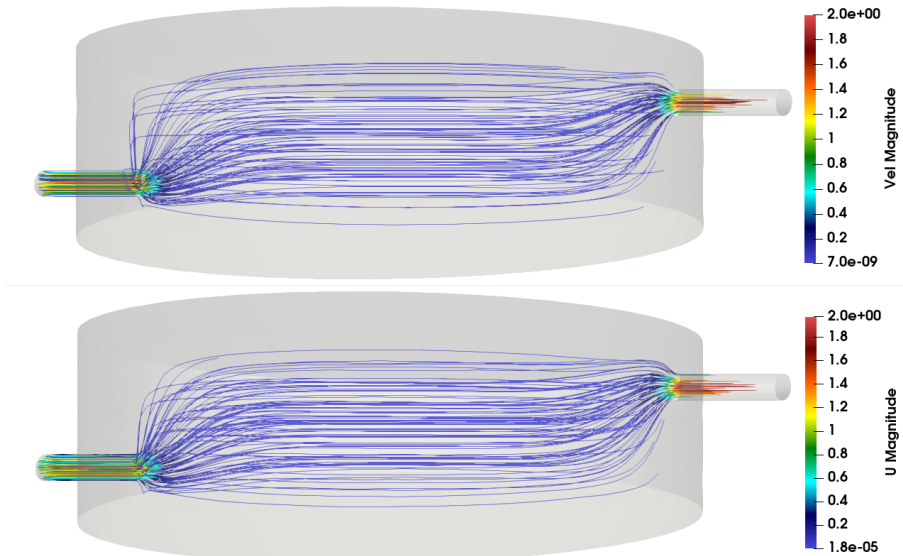


Figure 4.2: Comparing the results of the developed CFD model (top) with OpenFOAM (bottom) via plotting the streamlines of the fluid velocity field, depicted from the side view. The colors on the trajectory lines show the magnitude of the velocity vector.

Similarly, Fig. 4.3 depicts a comparison but from the top view, showing the good agreement between the predictions, although the OpenFOAM model (bottom) shows a slightly better performance on the boundaries.

Moreover, quantitative comparison is possible by comparing the numerical values predicted by the models in various regions of the domain of desired, including the regions close to the boundaries. Fig. 4.4 shows the comparison of the fluid velocity field visualization between the developed CFD code and OpenFOAM on a cross section in the center of the chamber, demonstrating that both models produce exactly the same results quantitatively.

A closer look at the center of Fig. 4.4 is depicted in Fig. 4.5, where color bar range is adapted to contain only the visible values. This close comparison also confirms the good agreement of the results between the CFD model and OpenFOAM. The employed mesh is relatively coarse in the center (regions far

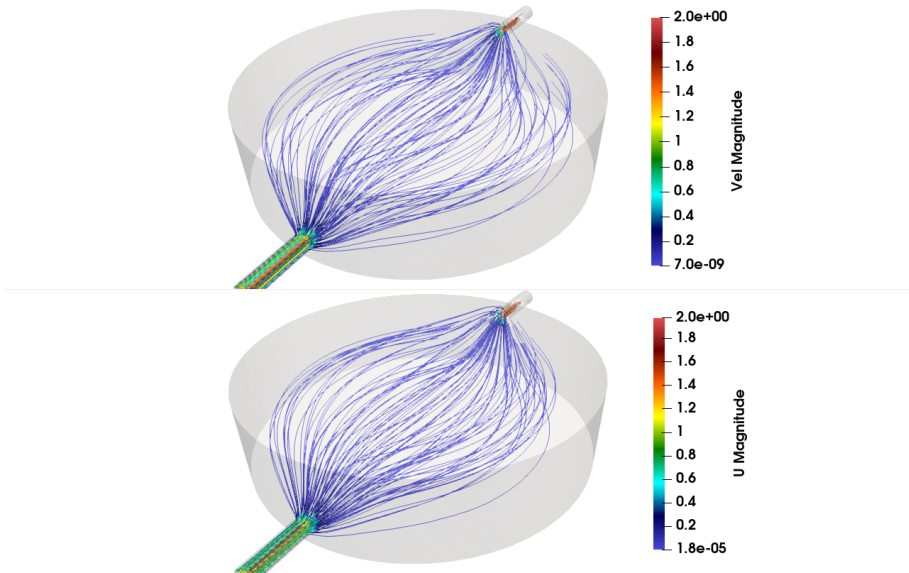


Figure 4.3: Streamlines of the fluid velocity field plotted from a top view to compare the output of the developed CFD model (top) and OpenFOAM (bottom) with colors showing the magnitude of the velocity vector at each point.

from the inlet and outlet), the effect of which can be seen as not smooth velocity profiles in Fig. 4.5. Still, both models handle this coarse mesh effect similarly.

Fig. 4.6 shows the result of a proof-of-concept simulation in which the biodegradation model [138] is coupled with the fluid flow model. This was done by solving Eq. 4.28 (or Eq. 4.25 for simpler cases) and adding a convection term to the equations of the biodegradation model to include the bidirectional effect of fluid flow on the degrading object. This effect can be seen in Fig. 4.6 with the released ions being advected to the right (the direction of the fluid flow) and the degrading object being slightly more degraded on the left.

Fig. 4.7 intended to demonstrate the effect of the degrading object on the fluid velocity field, depicted as streamlines passing over the solid part. As can be seen in the figure, the fluid velocity field evolves over time, demonstrating the response of the fluid flow, obtained from solving the Navier-Stokes equations (Eq. 4.28), to the change of the morphology of the obstacle.

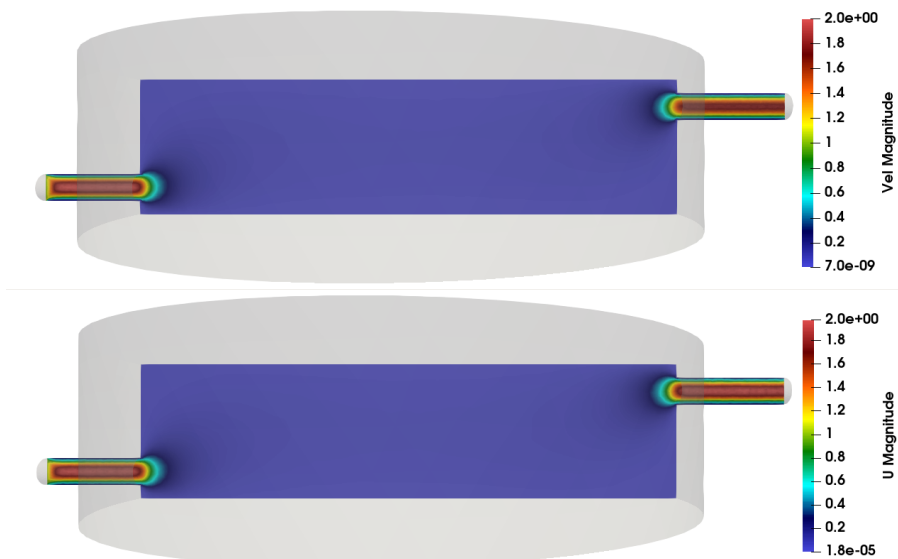


Figure 4.4: Comparison between the fluid velocity field predicted by the developed CFD code (top) and OpenFOAM (bottom), depicted on a vertical cross section in the center of the chamber. Fluid enters the chamber from left and leaves it from right. The colors show the magnitude of the velocity vector at each point.

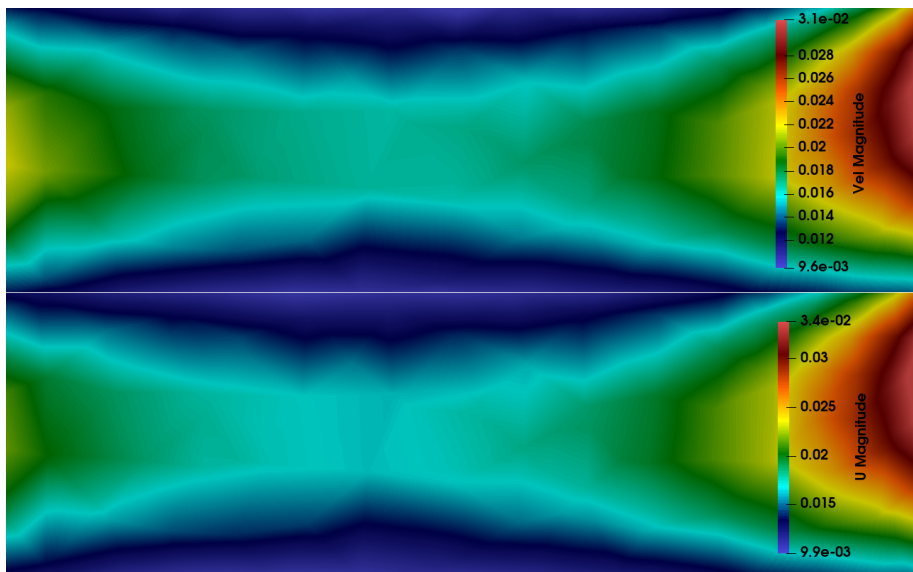


Figure 4.5: A closer look at the fluid velocity field for results predicted by the developed CFD code (top) and OpenFOAM (bottom) with colors showing the magnitude of the velocity vector at each point.

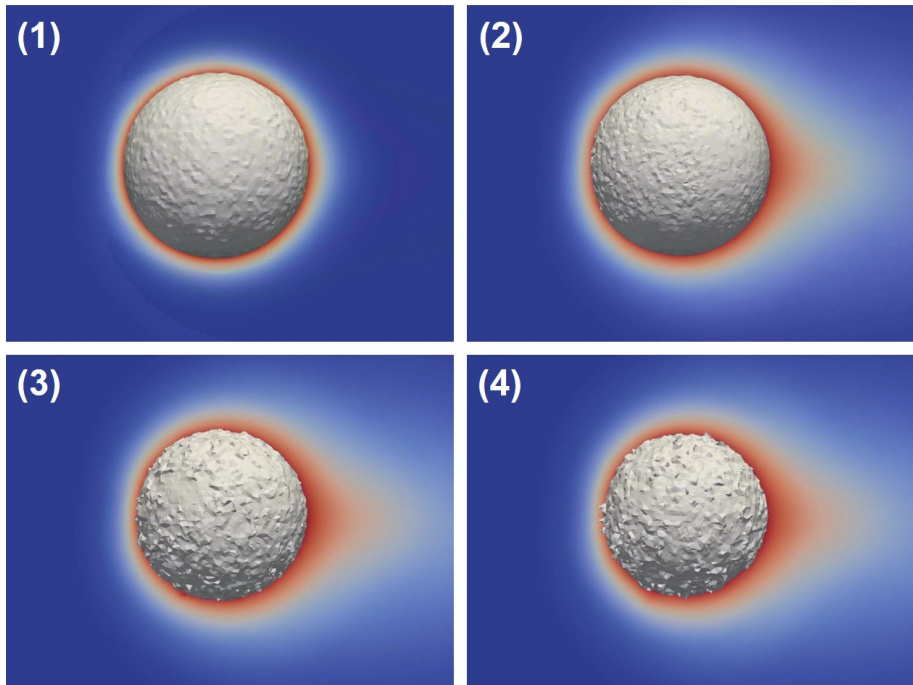


Figure 4.6: Biodegradation simulation results in the presence of fluid flow over time, showing the bidirection effect of fluid flow. The flow gets detoured due to presence of an obstacle, and the released ions get advected to the direction of fluid flow (left to right). The colors represent the concentration of Mg ions as they gets released to the surrounding environment and subsequently gets diffused/advecte. The gray surface shows the zero iso-contour of the used level-set function to track the interface of the degrading object, demonstrating the change of morphology of the solid part.

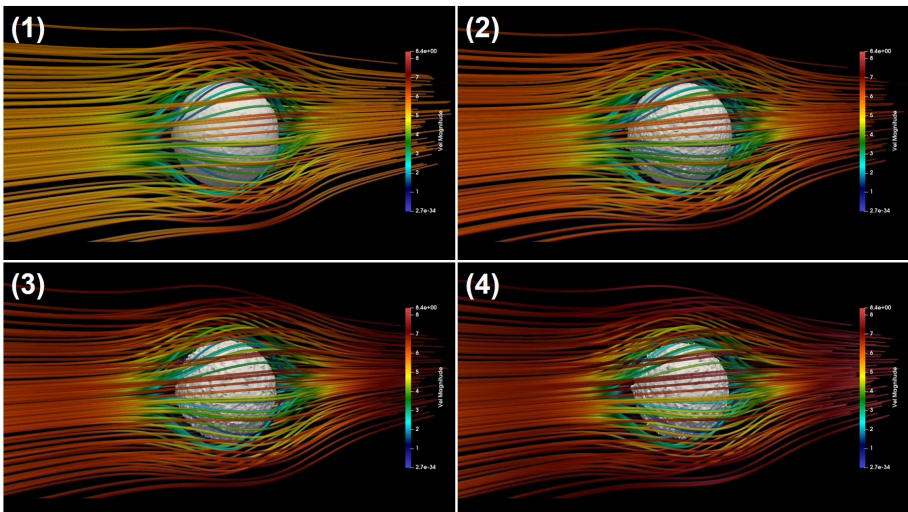


Figure 4.7: Visualization the evolution of the fluid velocity field depicted by streamlines passing over a degrading object. Colors show the magnitude of the velocity field projected on the streamlines.

# Chapter 5

## Advanced model with kinetics

This chapter is based on prepared manuscript to be submitted to *npj Computational Materials*:

M. Barzegari, C. Wang, S.V. Lamaka, G. Zavodszky, and L. Geris, “Interface-coupled multiphysics computational modeling of local pH changes during the biodegradation of magnesium biomaterials,” will be submitted to *npj Computational Materials*.

### 5.1 Introduction

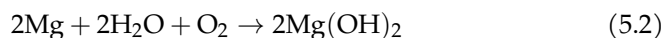
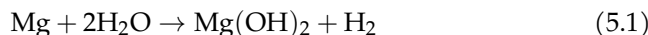
The biodegradation behavior of Mg is investigated in corrosion tests, in which the selection of the corrosive media plays an important role since it affects the underlying chemical reactions [21]. By considering the main application of the biomaterial, which can be tissue engineering scaffolds, vascular stents, or orthopedic fixation implants, the corrosive media can be selected to be a representative of the service environment. The most basic form of the medium is a saline (NaCl) solution, in which the degradation rate is the highest possible [21]. More complex solutions can be used to mimic the behavior of body environment by taking into account more body fluid components, the most

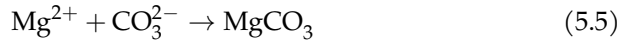
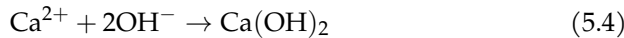
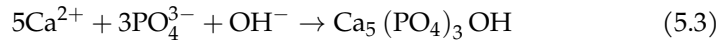
popular of which are the Ringer's solution, PBS (phosphate buffered saline), SBFs (simulated body fluids), HBSS (Hank's balanced salt solution), and Earle's balanced salt solution (EBSS) [21]. Adding more organic components to the solution will make it ready to simulate cell culture conditions. The common media for this purpose are MEM (Minimum Essential medium) and DMEM (Dulbecco's modified Eagle's medium) [21].

A wide range of various studies have already investigated the effect of different components in the aforementioned corrosive media on the degradation behavior of Mg materials [22, 23, 24, 25, 26]. A typical composition of "simulated body fluid" solutions (such as SBF, HBSS, and EBSS) is chloride, carbonate, phosphates, sulfate, and calcium. The individual effect of these components on the rate of degradation of Mg has been extensively studied, in which it has been observed that carbonate and phosphate slow down the rate while the effect of sulfate is negligible [24, 26]. The concentration of  $\text{HCO}_3^-$  affects the pH buffering capacity and the degradation rate of Mg simultaneously [33].

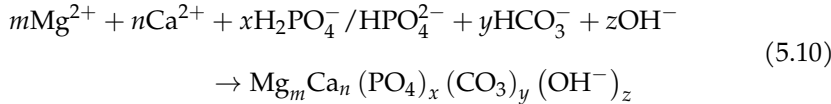
The effect of calcium ion is more complex because it has been found that  $\text{Ca}^{2+}$  doesn't contribute to the Mg corrosion directly [12], but a mixed effect of  $\text{Ca}^{2+}$ ,  $\text{Mg}^{2+}$ ,  $\text{HCO}_3^-$ , and  $\text{H}_2\text{PO}_4^- / \text{HPO}_4^{2-}$  forms a co-precipitation layer on the corroded surface of Mg, slowing down the corrosion rate of commercially pure Mg as well as some of the Mg alloys [22, 25]. It has been also reported that although various Mg alloys show different intrinsic degradation behavior in NaCl solution, they possibly behave similarly in simulated body fluids [34, 26]. Since the humoral regulations inside the human body control the changes in pH of body fluids, it's common to use pH buffers to mimic a similar condition, but it should be taken into account that buffering solution may affect the degradation rate of Mg [35, 36]. pH buffers may also delay the formation of the precipitate layer [25]. An alternative solution to address this issue is to use natural pH buffers such as  $\text{HCO}_3^- / \text{CO}_2$ , a technique that is commonly used for immersion tests under cell culture conditions. In this situation, an equilibrium between  $\text{H}_2\text{CO}_3$  ( $\text{CO}_2$ ),  $\text{HCO}_3^-$ , and  $\text{CO}_3^{2-}$  keeps the pH constant. As a result, using simulated body fluids for corrosion tests without additional synthetic pH buffer is still acceptable [25, 26].

The major reactions occurring in simulated body fluids can be written as:





Then, the aforementioned protection layer is formed on the corroded surface as a hydroxyapatite-like precipitation according the following reaction [30, 37, 38, 39]:



In fact, the similarity in corrosion behavior of various Mg alloys in SBF solutions is because of the similar composition of this quasi-protective layer, a mechanism that doesn't occur in NaCl solution, leading to more apparent difference of degradation rate between Mg alloys. The composition of the formed hydroxyapatite-like precipitation layer is close to the ones found *in vivo* [21]. Additionally, local pH measurements in HBSS and SBF shows that in contrast to saline solutions, the local pH value is not alkaline [25, 40]. This has been reported for hydrodynamics situation, under which the medium composition is kept constant by replacing the consumed ions by means of fluid flow.

## 5.2 Results

### 5.2.1 Thermodynamics-based simulation

Inputting the experimental conditions in the Hydra-Medusa software, including the initial composition and the contributing chemical components, results in a huge and complex output containing all the possible occurring chemical

reactions. Out of this output, relevant reactions for the current biodegradation systems were filtered out, and the filtered reactions were converted to desired concentration units. Fig. 5.1 depicts the output of this process separately for simulations performed at 25°C (RT) and 37°C, showing how the concentration of relevant components vary with changing the environment pH. The solubility products of these simulations were taken from Table 5.1, and equilibrium concentrations were set to be equal to the composition of the electrolyte, listed in Table 5.2.

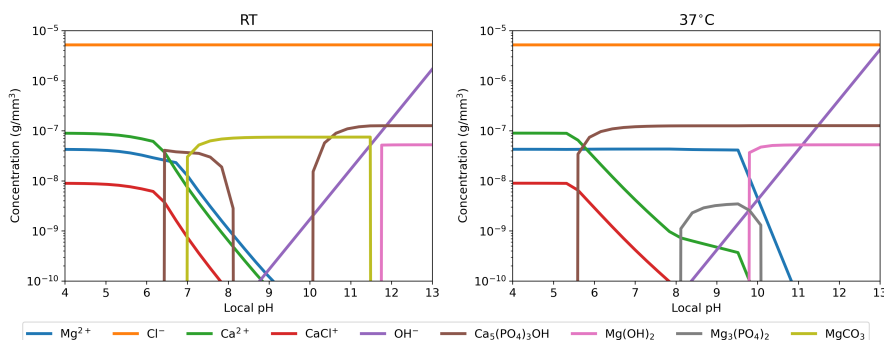


Figure 5.1: Selected relevant components from the Hydra-Medusa software output for given experimental conditions, showing how the concentration of various components vary with changing local pH

## 5.2.2 Biodegradation simulations

Fig. 5.2 shows a visualization of the local pH profiles from the top and side views for simulations performed at 25°C (RT) and 37°C after 12 hours. These profiles are comparable with the local pH distribution measured in the experiments as shown in Fig. 5.3. In these figures, the flow is from left to right, advecting the released ions in the flow direction.

Quantitative profiles provide a more accurate comparison between the computational predictions and experimentally-obtained values. The horizontal profiles, also called linescans, are depicted in Fig. ??, in which the local pH changes are plotted across a horizontal line 50 $\mu$ m above the surface of the sample for experiments using CP and UHP Mg and the computational model.

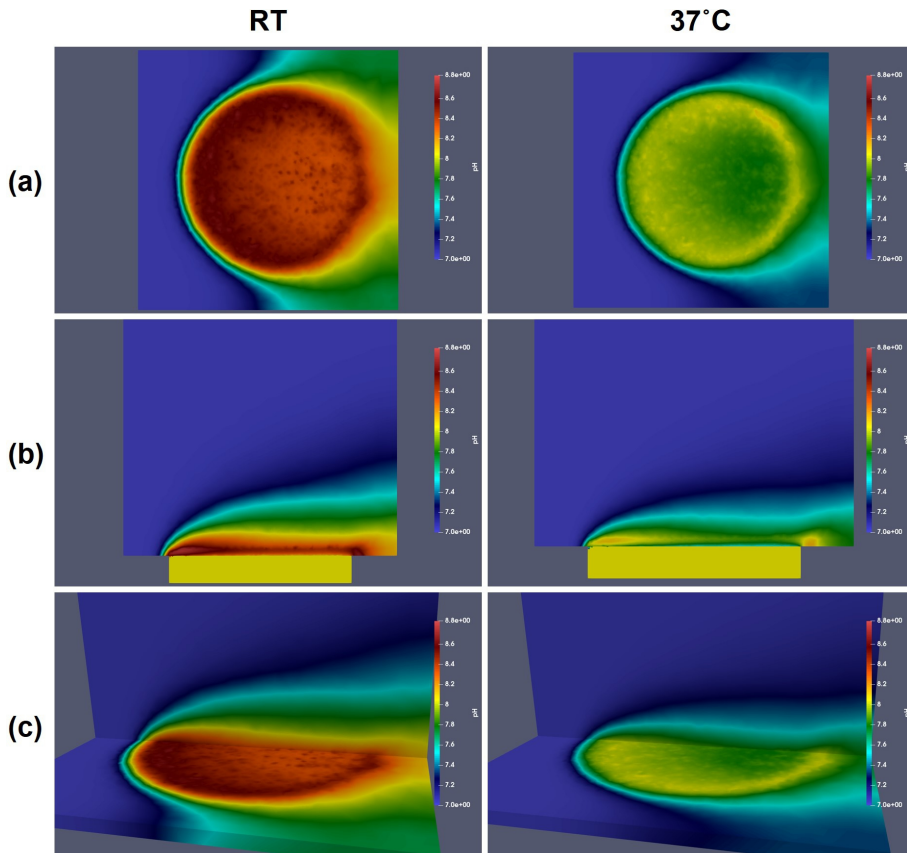


Figure 5.2: Simulation results for local pH predictions, depicting the local pH in a) top view from a horizontal cross section, b) side view from a vertical cross section, and c) perspective view with both the top and side cross sections, for simulations performed at 25°C (RT) and 37°C.

The data is recorded after 12 hours of immersion, which was also the final time of the simulations.

Similarly, Fig. 5.5 demonstrates the vertical pH profile after 12 hours of degradation, where the local pH is measured over a distance of 0.5mm vertically, starting from 50 $\mu$ m above the sample.

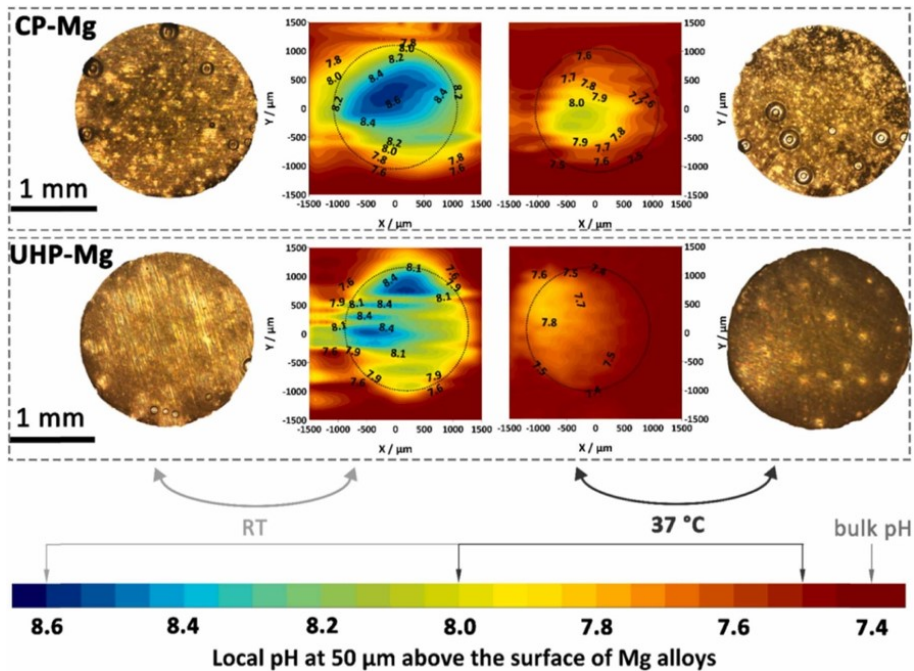
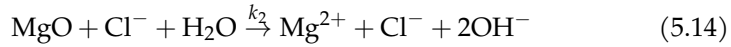
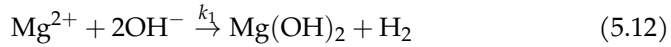
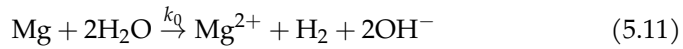


Figure 5.3: Experimental results for distribution of local pH above the surface of the sample, measured after 12 hours of degradation.

## 5.3 Discussion

## 5.4 Methods



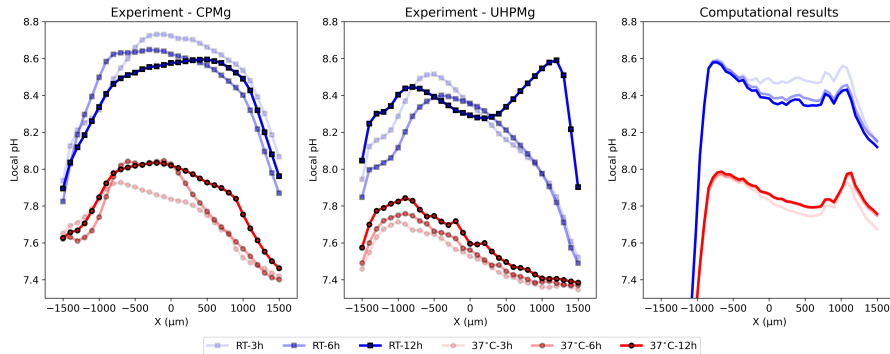


Figure 5.4: Comparing computational predictions and experimentally-obtained horizontal line scans of local pH changes, measured 50 $\mu\text{m}$  above the surface of the sample after 12 hours of degradation.

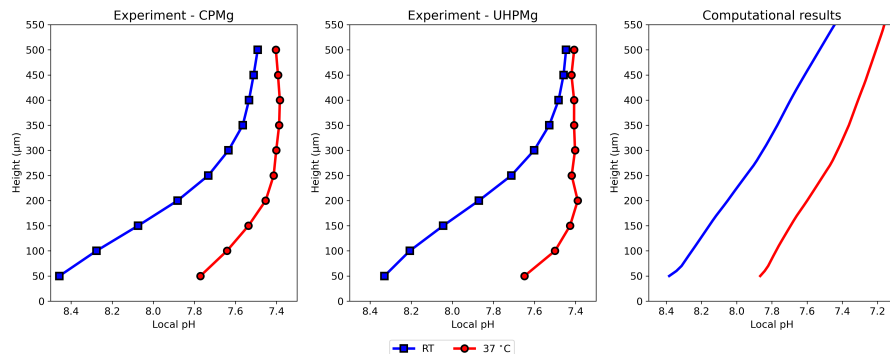


Figure 5.5: Comparing computational and experimental results for the local pH profiles, measured over a vertical line above the center of the sample after 12 hours of immersion.

$$\begin{aligned} C_{\text{Mg}} &= C_{\text{Mg}}(\mathbf{x}, t), \quad C_{\text{Mg}_{[s]}} = C_{\text{Mg}_{[s]}}(\mathbf{x}, t), \quad C_{\text{Film}} = C_{\text{Film}}(\mathbf{x}, t) \\ C_{\text{Cl}} &= C_{\text{Cl}}(\mathbf{x}, t), \quad C_{\text{OH}} = C_{\text{OH}}(\mathbf{x}, t) \quad \mathbf{x} \in \Omega \subset \mathbb{R}^3 \end{aligned} , \quad (5.15)$$

$$\frac{\partial C_{\text{Mg}_{[s]}}}{\partial t} = -k_0 C_{\text{Mg}_{[s]}} \quad (5.16)$$

$$\frac{\partial C_{\text{Mg}}}{\partial t} = \nabla \cdot (D_{\text{Mg}}^e \nabla C_{\text{Mg}}) - \nabla \cdot (\mathbf{u} C_{\text{Mg}}) + k_0 C_{\text{Mg}_{[\text{s}]}} - k_1 \alpha C_{\text{Mg}} C_{\text{OH}}^2 + k_2 C_{\text{Film}} C_{\text{Cl}}^2 \quad (5.17)$$

$$\frac{\partial C_{\text{Film}}}{\partial t} = k_1 \alpha C_{\text{Mg}} C_{\text{OH}}^2 - k_2 C_{\text{Film}} C_{\text{Cl}}^2 \quad (5.18)$$

$$\frac{\partial C_{\text{Cl}}}{\partial t} = \nabla \cdot (D_{\text{Cl}}^e \nabla C_{\text{Cl}}) - \nabla \cdot (\mathbf{u} C_{\text{Cl}}) \quad (5.19)$$

$$\frac{\partial C_{\text{OH}}}{\partial t} = \nabla \cdot (D_{\text{OH}}^e \nabla C_{\text{OH}}) - \nabla \cdot (\mathbf{u} C_{\text{OH}}) + k_0 C_{\text{Mg}_{[\text{s}]}} - k_1 \alpha C_{\text{Mg}} C_{\text{OH}}^2 + k_2 C_{\text{Film}} C_{\text{Cl}}^2 \quad (5.20)$$

where  $\alpha$  is defined as:

$$\alpha = \left(1 - \beta \frac{C_{\text{Film}}}{[\text{Film}]_{\text{max}}} \right), \quad (5.21)$$

in which the protective film maximum concentration is calculated using its porosity ( $\epsilon$ ) [55]:

$$[\text{Film}]_{\text{max}} = \rho_{\text{Mg(OH)}_2} \times (1 - \epsilon). \quad (5.22)$$

In Eqs. 5.17, 5.19, and 5.20,  $\mathbf{u}$  is the velocity field from the surrounding fluid flow governed by the Stokes equation:

$$\begin{cases} -\nu \Delta \mathbf{u} + \nabla p + \frac{\nu}{K} \mathbf{u} = 0 \\ \nabla \cdot \mathbf{u} + \epsilon p = 0. \end{cases} \quad (5.23)$$

in which  $\mathbf{u}$  is the fluid velocity,  $\mathbf{p}$  is the pressure (which is actually pressure divided by the density),  $\nu = \frac{\mu}{\rho}$  is the kinematic viscosity (with  $\mu$  being the dynamic viscosity), and  $K$  is the permeability function.

## 5.5 Data Availability

The data used in the paper are available from the authors upon request.

## 5.6 Code Availability

The source code of the programs used in this paper is available from the authors upon request.

Table 5.1: Solubility products of related chemical reactions at 25°C (RT) and 37°C

A	0.85 wt. % NaCl	SBF
$\text{Ca}_5(\text{PO}_4)_3\text{OH} \rightarrow 5\text{Ca}^{2+} + 3\text{PO}_4^{3-} + \text{OH}^-$	54.46	58.77
$\text{Mg}(\text{OH})_2 \rightarrow \text{Mg}^{2+} + 2\text{OH}^-$	11.25	11.25
$\text{Ca}(\text{OH})_2 \rightarrow \text{Ca}^{2+} + 2\text{OH}^-$	5.20	5.38
$\text{MgCO}_3 \rightarrow \text{Mg}^{2+} + \text{CO}_3^{2-}$	8.03	5.51
$\text{CaCO}_3 \rightarrow \text{Ca}^{2+} + \text{CO}_3^{2-}$	8.48	8.44
$\text{Mg}_3(\text{PO}_4)_2 \rightarrow 3\text{Mg}^{2+} + 2\text{PO}_4^{3-}$	23.28	27.62
$\text{H}_2\text{O(l)} \rightarrow \text{H}^+(\text{aq}) + \text{OH}^-(\text{aq})$	14.00	13.61
$\text{HCO}_3^-(\text{aq}) \rightarrow \text{CO}_3^{2-}(\text{aq}) + \text{H}^+(\text{aq})$	10.33	10.24
$\text{HPO}_4^{2-}(\text{aq}) \rightarrow \text{PO}_4^{3-}(\text{aq}) + \text{H}^+(\text{aq})$	12.35	12.32

Table 5.2: Chemical composition of the HBSS electrolytes used to perform corrosion tests for local pH measurements.

Components	mM
KCl	5.33
$\text{KH}_2\text{PO}_4$	0.44
$\text{NaHCO}_3$	4.17
NaCl	137.9
$\text{Na}_2\text{HPO}_4$	0.34
$\text{CaCl}_2$	1.26
$\text{MgCl}_2 \cdot 6\text{H}_2\text{O}$	0.49
$\text{MgSO}_4 \cdot 7\text{H}_2\text{O}$	0.41
D – Glucose	5.56

## 5.7 Acknowledgements

## 5.8 Author Contributions

## 5.9 Competing Interests

Table 5.3: The elemental composition of ultra high pure and commercial pure Mg used for performing corrosion experiments

	Fe	Si	Mn	Al	Cu	Ni
CP-Mg	0.03420	0.0001	0.00237	0.00402	0.00037	<0.0002
UHP-Mg	0.0012	<0.0001	0.00037	0.00291	<0.0001	<0.0002

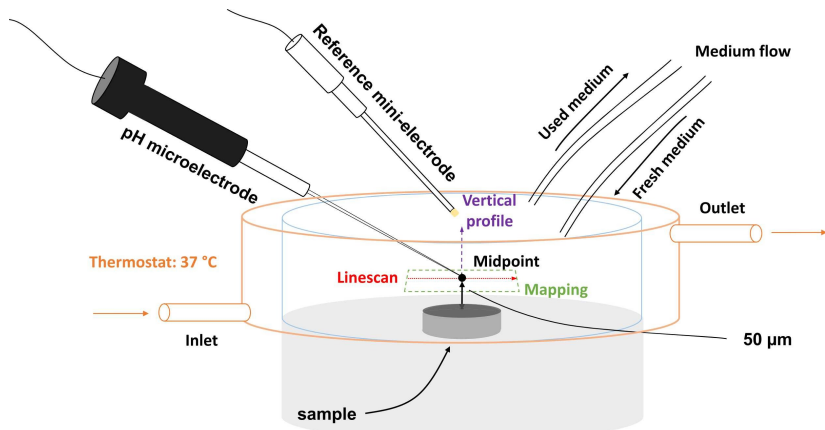


Figure 5.6: Experimental setup for validating the coupled biodegradation model

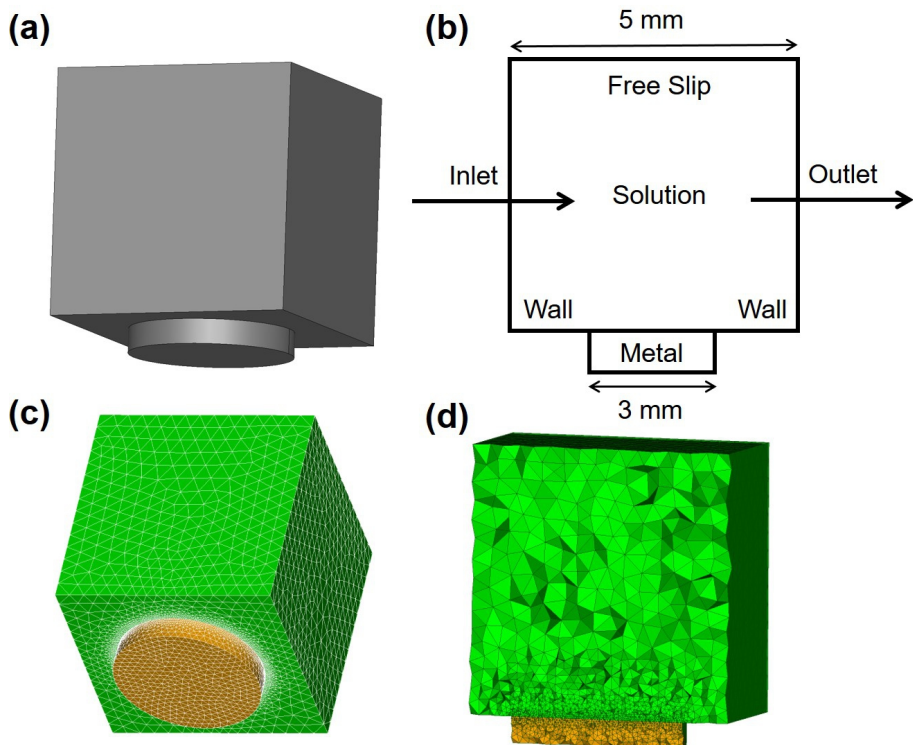


Figure 5.7: Computational model setup for local pH simulations



# Chapter 6

## Tissue growth modeling

### 6.1 Introduction

Numerical tracking of interface movement has been used for certain modeling applications in science and engineering for multi-material and multiphase problems such as solidification, melting, corrosion, and grain growth to name a few [88]. The most popular Eulerian methodologies in this regard are the level-set [89, 90, 61], volume-of-fluid (VOF) [91], and phase-field methods [92, 93].

The basic idea of the level-set method is to employ the Hamilton-Jacobi (HJ) algorithm for solving the general interface advection equation. The independent variable in the level-set method is a signed distance function, called the level-set function  $\psi$  [61]. The level-set function should be re-initialized as the interface evolves, which is the reason behind an inadvertent mass loss, one of the most prominent shortcomings of the level-set method. Although the VOF method is not vulnerable to the mass loss issue, calculating the interface curvature is difficult from the volume fraction [88].

To overcome these challenges, diffuse interface methods [?] have gained attentions in recent decades, among which the phase-field method has shown potential for solving complex moving interface problems. Contrary to the level-set method, in diffuse interface methods, the interface is considered as a smooth transition between phases, which usually has a finite width. In the phase-field method, a non-conserved (or conserved) order parameter  $\phi$  is

defined such that  $\phi = 1$  in one bulk phase and  $\phi = -1$  in the other. Then, the smooth transition between these two phases ( $-1 < \phi < 1$ ) is marked as the interface. One of the advantages of the phase-field method is that the derived equation can be solved over the entire domain of desired without considering the location of the interface. Moreover, although the curvature and interface normal vectors are not formulated explicitly, the phase-field method is suitable for problems in which the evolution of the interface depends on the local curvature or a field acting normal to the interface [88]. The phase-field method keeps a constant thickness for the smooth transition region normal to the interface, and as a result, no re-initialization as for the level-set method is needed.

The phase-field method has been already proved to be an efficient interface tracking technique for various problems in micro/meso scales such as solidification [94, 92], microstructural evolution [95], grain growth [96], crack propagation [97, 98], electromigration [99], and extractive metallurgy [93]. However, it has been used recently for dealing with problems described in macro level, such as corrosion [100, 101, 102, 103, 104, 105, 106] and cell/tissue growth [107, 108]. In this work, a phase-field model of the tissue growth process was developed to describe the cell growth behavior on 3D surfaces as a moving-boundary problem. Additionally, a similar model was developed based on the level-set method to compare the performance and results of both interface tracking methods. Both models were implemented using the finite element method.

## 6.2 Deriving the model

In this section, the derivation of the phase-field and level-set equations from the general advection equation is demonstrated. This shows the similarities and differences of these interface tracking techniques for moving boundary problems.

### 6.2.1 General equation of interface motion

The general interface advection equation for an Eulerian description of interface movement can be written as [88]:

$$\frac{\partial \phi}{\partial t} + \mathbf{u} \cdot \nabla \phi = 0 \quad (6.1)$$

where  $\phi$  is the phase field and  $\mathbf{u}$  is the interface velocity. The velocity  $\mathbf{u}$  can be divided into normal ( $u_n$ ) and external velocity components ( $u_e$ ):

$$\mathbf{u} = u_n \mathbf{n} + \mathbf{u}_e \quad (6.2)$$

in which  $\mathbf{n} = \nabla \phi / |\nabla \phi|$  is the unit vector normal to the interface. So, Eq. 6.1 can be rewritten as:

$$\frac{\partial \phi}{\partial t} + u_n |\nabla \phi| + \mathbf{u}_e \cdot \nabla \phi = 0 \quad (6.3)$$

The normal velocity can be decomposed into more components to take into account the effect of interface curvature ( $\kappa$ ) such that the terms are independent and proportional to the curvature, respectively:

$$u_n = a - b\kappa \quad (6.4)$$

where the coefficients  $a$  and  $b$  have units of m/s and m<sup>2</sup>/s. Substituting this into Eq. 6.2 yields to the final form of the interface motion equation:

$$\frac{\partial \phi}{\partial t} + a |\nabla \phi| + \mathbf{u}_e \cdot \nabla \phi = b\kappa |\nabla \phi| \quad (6.5)$$

### 6.2.2 Phase-field formulation

To further proceed with the phase-field formulation, a proper kernel should be selected for the phase field variable, which can be done based on Beckermann et al. [109]:

$$\phi = -\tanh\left(\frac{n}{\sqrt{2}W}\right) \quad (6.6)$$

in which  $W$  is the thickness of the transition profile ( $\phi$  varies from  $-0.9$  to  $+0.9$  in a narrow layer with the width of  $3\sqrt{2}W$ ), and  $n$  is the coordinate normal to the interface. The curvature can be written as a function of the phase field variable:

$$\kappa = \nabla \cdot \mathbf{n} = \nabla \cdot \left( \frac{\nabla \phi}{|\nabla \phi|} \right) = \frac{1}{|\nabla \phi|} \left[ \nabla^2 \phi - \frac{(\nabla \phi \cdot \nabla) |\nabla \phi|}{|\nabla \phi|} \right] \quad (6.7)$$

Using the defined kernel, the terms in Eq. 6.7 can be expressed as:

$$|\nabla\phi| = -\frac{\partial\phi}{\partial n} = \frac{1-\phi^2}{\sqrt{2}W} \quad \text{and} \quad \frac{(\nabla\phi \cdot \nabla)|\nabla\phi|}{|\nabla\phi|} = \frac{\partial^2\phi}{\partial n^2} = -\frac{\phi(1-\phi^2)}{W^2} \quad (6.8)$$

Substituting Eq. 6.8 into Eq. 6.7 yields to the following definition of interface curvature:

$$\kappa = \frac{1}{|\nabla\phi|} \left[ \nabla^2\phi + \frac{\phi(1-\phi^2)}{W^2} \right] \quad (6.9)$$

which subsequently changes Eq. 6.5 into:

$$\frac{\partial\phi}{\partial t} + a|\nabla\phi| + \mathbf{u}_e \cdot \nabla\phi = b \left[ \nabla^2\phi + \frac{\phi(1-\phi^2)}{W^2} \right] \quad (6.10)$$

Eq. 6.10 is the derived form of phase-field equation for tracking of an evolving interface, containing terms corresponding for normal interface motion, advection by an external field, and curvature-driven movement. The  $|\nabla\phi|$  term in Eq. 6.10 can be replaced by its definition in Eq. 6.8 to form another version of the equation:

$$\frac{\partial\phi}{\partial t} + a\frac{1-\phi^2}{\sqrt{2}W} + \mathbf{u}_e \cdot \nabla\phi = b \left[ \nabla^2\phi + \frac{\phi(1-\phi^2)}{W^2} \right] \quad (6.11)$$

which is an easier version to be implemented using numerical methods. The unique term on the right-hand side of Eq. 6.11 is a characteristic of the phase-field method.

### 6.2.3 Level-set formulation

From the mathematical perspective, the level set equation has a direct connection to the phase-field equation and can be derived by replacing the phase field variable by a sign distance function. To this end, Eq. 6.5 can be rewritten to be a level set equation:

$$\frac{\partial\psi}{\partial t} + a|\nabla\psi| + \mathbf{u}_e \cdot \nabla\psi = b\kappa|\nabla\psi|, \quad (6.12)$$

with  $\psi$  being a sign distance function that describes the distance of each point of the computational domain to the interface. This implies that the zero iso-contour of the level-set function defines the interface.

## 6.3 Dimensionless forms for various cases

### 6.3.1 Stationary interface

A stationary interface, where there is no interface motion ( $a = 0$  and  $u_e = 0$ ), is a primary problem to examine the formulation and select proper grid spacing parameters. For a 1-D case, Eq. 6.11 can be simplified as:

$$\frac{\partial \phi}{\partial t} = b \left( \frac{\partial^2 \phi}{\partial x^2} + \frac{\phi (1 - \phi^2)}{w^2} \right) \quad (6.13)$$

To scale this equation, the following dimensionless variables can be defined:

$$x' = \frac{x}{x_c} \quad \text{and} \quad t' = \frac{t}{t_c} \quad (6.14)$$

So, Eq. 6.13 can be rewritten using these new variables:

$$\frac{1}{t_c} \frac{\partial \phi}{\partial t'} = \frac{b}{x_c^2} \frac{\partial^2 \phi}{\partial x'^2} + \frac{b}{w^2} f(\phi) \quad (6.15)$$

Defining  $x_c = w$  and  $t_c = w^2/b$  leads to the following dimensionless form of Eq. 6.13:

$$\frac{\partial \phi}{\partial t'} = \frac{\partial^2 \phi}{\partial x'^2} + \phi (1 - \phi^2) \quad (6.16)$$

Numerical results for Eq. 6.16 is depicted in Fig. 6.1, and the phase field profile is compared with the level set distance function profile. An appropriate value for grid spacing and the layer width should be selected such that  $0.25w < \Delta x' < 0.5w$ . Additionally, the selected value of  $w$  should satisfy  $w < R/4.2$ , in which  $R$  is the local radius of curvature [88].

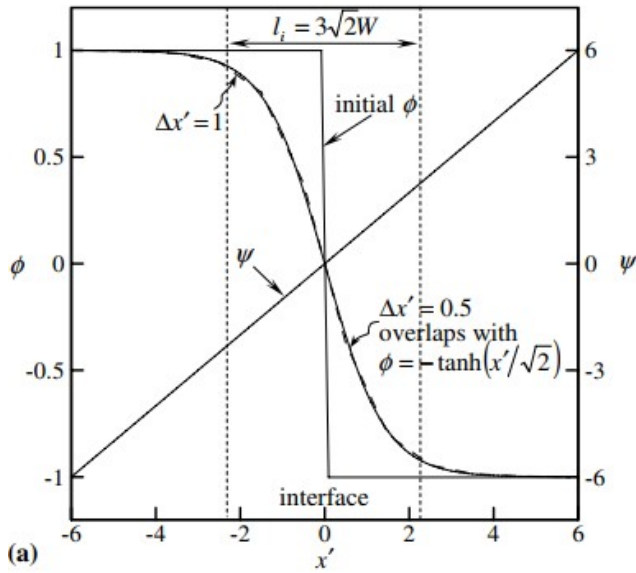


Figure 6.1: Comparison of phase field variable and level set function on the interface of a stationary interface with step function like initial condition [88]

### 6.3.2 Evolution under constant normal speed

For a problem in which the interface moves with constant velocity exclusively, Eq. 6.11 can be simplified according to the condition of  $a = \text{const.}$ ,  $u_e = 0$ , and  $b = 0$  ( $b$  exists in the equation as a numerical parameter for smoothing the interface and relaxation behavior of the phase-field profile):

$$\phi_t + a \frac{1 - \phi^2}{\sqrt{2}w} = b\phi_{xx} + b \frac{f(\phi)}{w^2} \quad (6.17)$$

Defining dimensionless variables according to Eq. 6.14 yields to:

$$\frac{1}{t_c}\phi_{t'} + \frac{a}{w} \frac{1 - \phi^2}{\sqrt{2}} = \frac{b}{w^2}\phi_{x'x'} + \frac{b}{w^2}f(\phi) \quad (6.18)$$

which can be reordered to:

$$\phi_{t'} + \frac{1 - \phi^2}{\sqrt{2}} = b' (\phi_{x'x'} + f(\phi)) \quad (6.19)$$

with  $b' = b/aw$ . For a stable numerical implementation,  $\Delta t'/\Delta x' < 0.1$  and  $b' < 1.2$  should be met roughly [88].

### 6.3.3 Curvature-driven interface evolution

A curvature-driven motion, which is desired for the current study, is straightforward to formulate using the phase-field method. In this specific case,  $b$  is not a numerical parameter anymore. A dimensionless form of Eq. 6.11 can be derived using a similar method for the stationary interface for a multidimensional case with  $u_n = -b\kappa$ ,  $a = 0$ , and  $u_e = 0$ :

$$\frac{\partial \phi}{\partial t'} = \nabla'^2 \phi + \phi (1 - \phi^2) \quad (6.20)$$

in which  $t'$  and  $\nabla'$  are defined similar to Eq. 6.14 as  $t' = t/(w^2/b)$  and  $\nabla' = \nabla/w$ , respectively.

## 6.4 Numerical implementation

Numerical solution of the phase-field equation involves dealing with the non-linearity of the equation. Additionally, in the case of dimensional form (Eq. 6.11), small coefficients of the state variable in the PDE leads to numerical difficulties. As a result, numerical implementation of the phase-field equation, especially for the spectral methods such as finite element method, is still tricky and an active field of research [110, 111].

In the finite element method, the solution of a PDE is calculated based on a sum of a set of certain basis functions, which are commonly piecewise polynomial functions that are non-zero only on a small element. For doing this, the PDE is first written in a weak formulation, and then the weak form is projected on a discretized space (a set of elements) to be written as the summation of the basis functions.

In this section, the numerical solution of the stationary form (Eq. 6.13) and its corresponding considerations are elaborated as an example of employing the finite element formulation for simulating the phase-field equation. So, by assuming  $b = 1$  and  $f(\phi) = \phi(1 - \phi^2)$ , the problem can be summarized as:

$$\begin{cases} \frac{\partial\phi}{\partial t} - \Delta\phi + \frac{1}{w^2}f(\phi) = 0, & (x, t) \in \Omega \times (0, T] \\ \frac{\partial\phi}{\partial n} \Big|_{\partial\Omega} = 0 \\ u|_{t=0} = u_0 \end{cases} \quad (6.21)$$

which demonstrates the PDE, the boundary condition, and the initial condition of the phase field variable where  $\Omega$  is the domain of interest,  $\partial\Omega$  is its boundary, and  $T$  is the final time. Deriving the weak formulation of Eq. 6.21 is relatively straightforward as it can be seen as a time-dependent diffusion-reaction PDE, but the difficulty arises for choosing the numerical stability scheme for discretizing the temporal derivative and dealing with the non-linearity of  $f(\phi)$  while normally the  $\frac{1}{w^2}$  coefficient is a small number.

Incorporating a first-order semi-explicit scheme for Eq. 6.21 yields to:

$$\frac{1}{\Delta t} (\phi^{n+1} - \phi^n, v) + (\nabla\phi^{n+1}, \nabla v) + \frac{1}{w^2} (f(\phi^n), v) = 0, \quad \forall v \in H^1(\Omega) \quad (6.22)$$

where  $\Delta t$  is the time step,  $(\cdot, \cdot)$  denotes the inner product, and  $H^1(\Omega)$  is the Sobolev space of the domain  $\Omega$ , which is a space of functions whose derivatives are square-integrable functions in  $\Omega$ . The main issue with this discretization scheme is its restrictive time step condition which should satisfy:

$$\Delta t < \frac{2w^2}{L} \quad (6.23)$$

where  $L$  is a limit related to the non-linear part:

$$\max |f'(\phi)| \leq L \quad (6.24)$$

Obviously, as  $\Delta t \sim w^2$ , a very small time step is required to achieve stability in this scheme.

Taking advantage of a fully implicit scheme improves the stability as it will be unconditionally stable, but it results to an equation that is difficult to implement as it needs solving a fixed point problem at each step. For example, a modified second-order implicit Crank-Nicolson scheme for Eq. 6.21 can be

written as:

$$\left( \frac{\phi^{n+1} - \phi^n}{\Delta t}, v \right) + \left( \nabla \frac{\phi^{n+1} + \phi^n}{2}, \nabla v \right) + \frac{1}{w^2} \left( \tilde{f}(\phi^{n+1}, \phi^n), v \right) = 0, \quad \forall v \in H^1 \quad (6.25)$$

where:

$$\tilde{f}(u, v) = \begin{cases} \frac{F(u) - F(v)}{u - v} & \text{if } u \neq v \\ f(u) & \text{if } u = v \end{cases} \quad (6.26)$$

in which  $F$  is the potential term ( $f(\phi) = F'(\phi)$ ).

An alternative can be deriving a stabilized semi-implicit scheme by adding a stabilization term to Eq. 6.22. A first-order version of such a scheme can be written as:

$$\left( \frac{1}{\Delta t} + \frac{S}{w^2} \right) (\phi^{n+1} - \phi^n, v) + \left( \nabla \phi^{n+1}, \nabla v \right) + \frac{1}{w^2} (f(\phi^n), v) = 0, \quad \forall v \in H^1(\Omega) \quad (6.27)$$

which is unconditionally stable for every  $S \geq \frac{L}{2}$ .

## 6.5 Adapting the formulation for curvature-driven tissue growth

In order to adapt Eq. 6.20 for the curvature-driven process of neo-tissue growth, one can consider the following equation:

$$\frac{\partial \phi}{\partial t'} = \left( \nabla'^2 \phi + \phi (1 - \phi^2) \right) . H \left( \nabla'^2 \phi + \phi (1 - \phi^2) > 0 \right) \quad (6.28)$$

in which  $H$  denotes a heaviside step function. Eq. 6.28 implies that the growth is only allowed for regions with a positive curvature (right hand side of Eqs. 6.11 and 6.20).

Using the same approach, a similar level set formulation can be obtained based on Eq. 6.12 by omitting the normal velocity and curvature terms and embedding the effect of the curvature in the velocity field. Doing this yields to a convection equation for the distance function:

$$\frac{\partial \psi}{\partial t} + \mathbf{u} \cdot \nabla \psi = 0, \quad (6.29)$$

in which the convection velocity field can be defined as:

$$\mathbf{u} = \begin{cases} -\kappa \mathbf{n} & \text{if } \kappa > 0 \\ 0 & \text{if } \kappa \leq 0 \end{cases} \quad (6.30)$$

with  $\kappa$  being calculated similar to Eq. 6.7 for a distance function  $\psi$ . In practical implementations, the distance function is not differentiable at every location of the domain due to discontinuities in the gradients, so one can consider taking advantage of artificial diffusion terms to overcome this issue, leading to the following equations for the normal vector and curvature calculation:

$$\mathbf{n} = \frac{\nabla \varphi}{|\nabla \varphi|} + \varepsilon \Delta \mathbf{n} \quad (6.31)$$

$$\kappa = \nabla \cdot \mathbf{n} + \varepsilon \Delta \kappa \quad (6.32)$$

in which  $\varepsilon$  denotes the numerical diffusion coefficient.

## 6.A Implementing the phase-field model using physics-informed neural networks

## **Part III**

# **Code Implementation and Software Development**

# Chapter 7

## Model parallelization

This chapter is based on previously published content in *The International Journal of High Performance Computing Applications*:

M. Barzegari, and L. Geris, "Highly scalable numerical simulation of coupled reaction-diffusion systems with moving interfaces," *The International Journal of High Performance Computing Applications*, vol. 36, pp. 198-213, 2022.

### 7.1 Introduction

Moving-boundary problems [60] are a subset of the general concept of boundary-value problems which not only require the solution of the underlying partial differential equation (PDE), but also the determination of the boundary of the domain (or sub-domains) as part of the solution. Moving-boundary problems are usually referred to as Stefan problems [60] and can be used to model a plethora of phenomena ranging from phase separation and multiphase flows in materials engineering to bone development and tumor growth in biology. Reaction-diffusion systems are the mathematical models in which the change of state variables occurs via transformation and spreading. These systems are described by a set of parabolic PDEs and can model a large number of different systems in science and engineering, for instance predator-prey models in biology and chemical components reactions in chemistry [59]. Combining the reaction-diffusion systems with moving-boundary problems

provides a way to study the systems in which the diffusion and reaction lead to the change of domain geometry. Such systems have great importance in various real-world scenarios in chemistry and chemical engineering as well as environmental and life sciences.

In this study, the material degradation phenomenon has been investigated as an example of a reaction-diffusion system with moving boundaries, in which the loss of material due to corrosion leads to movement of the interface of the bulk material and surrounding corrosion environment. More specifically, the degradation of magnesium (Mg) in simulated body fluid has been chosen as a case study. Magnesium has been chosen due to its growing usability as a degradable material in biomedicine, where it is usually used in biodegradable implants for bone tissue engineering and cardiovascular applications [44, 10]. The ultimate application of such a model can be then to study the degradation behavior of resorbable Mg-based biomaterials.

A wide range of different techniques has already been developed to study the moving interfaces in reaction-diffusion problems, which can be grouped into 3 main categories: 1) mesh elimination techniques, in which some elements are eliminated to simulate the interface movement (or loss of material in corrosion problems), 2) explicit surface representation, such as the arbitrary Lagrangian-Eulerian (ALE) method, which tracks the interface by moving a Lagrangian mesh inside an Eulerian grid, and 3) implicit surface tracking, in which an implicit criterion is responsible to define the moving interface during the reaction-diffusion process. Related to the aforementioned case study, studies performed by [57] and [48] are examples of the first group. [57] have constructed a simulation of degradation using the mesh elimination technique. [48] have developed a continuous damage (CD) model by using an explicit solver to study the degradation. The work of [50] is an example of the second group as they have developed one of the first models to correlate the mass flux of the metallic ions in the biodegradation interface to the velocity of said interface. This was used to build an ALE model to explicitly track the boundary of the material during degradation. Studies of the third category are based more on mathematical modeling rather than available models in simulation software packages. This approach results in more flexibility and control over the implementation of the computational model. For instance, [52] have derived a system of mathematical equations to study galvanic corrosion of metals, taking advantage of the level set method (LSM) to track the corrosion front. [55] have used the definition of velocity of the biodegradation interface

as the speed of the moving boundary in LSM, enabling them to track the geometrical changes of the material during degradation. Similarly, [112] have used a combination of LSM and extended finite element method (XFEM), a method to model regions with spatial discontinuities, to study the moving corrosion front in the pitting corrosion process. A very similar approach and formulation has been taken by [113] to model localized pitting corrosion. An alternative method for tracking the moving interface is the phase field method, which has been used in a wide range of relevant studies. A comparison between the behavior of phase-field and LSM formulations for an evolving solid-liquid interface has been performed by [114], showing that both methods lead to the same results for diffusion-reaction systems. The approach taken in this study was similar to the one from Bjger et al., where LSM was employed to correlate the diffusion and reaction processes to the movement of the solid-solution interface using continuous variables.

Tracking the moving front at the diffusion interface requires high numerical accuracy of the diffusive state variables, which can be achieved using a refined computational grid. This makes the model computationally intensive, and as a consequence, implementing parallelization is an inevitable aspect of simulating such a model. Such an approach enables the model to simulate large-scale systems with a large number of degrees of freedom (DOF) in 3D with higher performance and efficiency in high-performance computing (HPC) environments. In recent years, parallelization of diffusion-reaction systems simulation has been investigated, but the studies are mainly conducted for stochastic (statistical) models. For instance, [115] have developed a parallel stochastic model for large-scale spatial reaction-diffusion simulation, and similarly, [116] have developed a stochastic high-performance simulator for specific biological applications. Also as an example for massively parallel systems, [117] have conducted a simulation of reaction-diffusion processes in biology using graphics processing units (GPUs). Although stochastic models have more parallel-friendly algorithms, explaining the underlying process, especially when it involves reaction-diffusion processes of chemistry and biology, is less complex and more universal using mechanistic (deterministic) models, which are based on well-developed mathematical models of continuous systems [118]. To the best of authors' knowledge, none of the previous contributions to the topic of reaction-diffusion systems with moving interfaces has employed parallelization techniques to increase the performance and speed of execution of the model without compromising the accuracy of the interface tracking.

In the current study, we developed a mechanistic model of a reaction-diffusion system coupled with a moving interface problem. Improving the accuracy of the interface capturing requires a refined computational mesh, leading to a more computation-intensive simulation. To overcome this challenge and yield more interactable simulations, scalable parallelization techniques were implemented making the model capable of being run on massively parallel systems to reduce the simulation time. The investigated case-study is the material degradation process. The developed model captures the release of metallic ions to the medium, formation of a protective film on the surface of the material, the effect of presented ions in the medium on the thickness of this protection layer, and tracking of the movement of the corrosion front (Fig. 7.1). The interface tracking was performed using an implicit distance function that defined the position of the interface during degradation. This implicit function was obtained by constructing and solving a level set model. It is also worth noting that in a real-world application, such systems require a calibration (also called parameter estimation or inverse problem), in which the model should be simulated hundreds of times. This makes the parallelization even more crucial for these models.

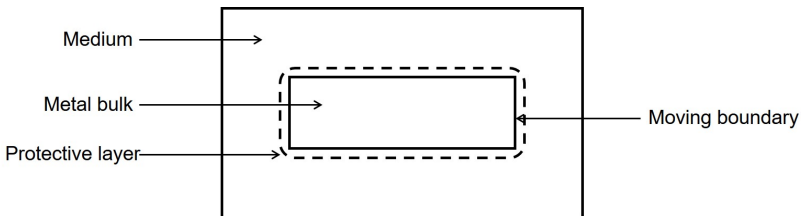


Figure 7.1: A schematic presentation of different components of the developed model for simulation of the degradation process with a moving front.

## 7.2 Background theory and model description

Before elaborating the parallel implementation strategy, the mathematical model is briefly described in this section. The model is constructed based on the chemistry of degradation, starting from the previous work by [55], in which the ions can diffuse to the medium and react with each other.

### 7.2.1 Chemistry of degradation

In metals, degradation occurs through the corrosion process, which usually consists of electrochemical reactions, including anodic and cathodic reactions as well as the formation of side products [7].

For Mg, the corrosion reactions comprise the following steps [7]: first, the material is released as metallic ions and free electrons, which causes the volume of the bulk material to be reduced:



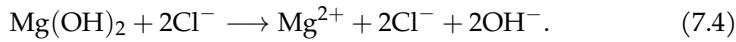
The free electron reduces water to hydrogen gas and hydroxide ions:



Then, with the combination of the metallic and hydroxide ions, a porous film is formed on the surface, slowing down the degradation rate by protecting the material underneath:



With the presence of some specific ions in the surrounding medium, such as chloride ions in a saline solution, the protective film might be broken partially, which contributes to an increase of the rate of degradation:



The degradation process of metals is a continuous repetition of the above reactions.

### 7.2.2 Reaction-diffusion equation

A reaction-diffusion partial differential equation can describe the state of a reaction-diffusion system by tracking the change of the concentration of the different components of the system over time [59]. The equation is a parabolic

PDE and can be expressed as

$$\frac{\partial u}{\partial t} - \nabla \cdot [D \nabla u] = f(u) \quad (7.5)$$

in which the change of the state variable  $u = u(\mathbf{x}, t), \mathbf{x} \in \Omega \subset \mathbb{R}^3$  is described as a combination of how it diffuses and how it is produced or eliminated via reactions. The term  $f(u)$  is a smooth function that describes the reaction processes.

In the example used in this study, the state variable in Eq. 7.5 is the concentration of effective chemical components involved in the degradation process, namely magnesium ions and the protective layer, denoted by  $C_{\text{Mg}}$  and  $C_{\text{Film}}$  respectively.

$$C_{\text{Mg}} = C_{\text{Mg}}(\mathbf{x}, t), \quad C_{\text{Film}} = C_{\text{Film}}(\mathbf{x}, t) \quad \mathbf{x} \in \Omega \subset \mathbb{R}^3 \quad (7.6)$$

$\Omega$  is the whole domain of interest, including the bulk material and its surrounding medium. So, by assuming that the reaction rates of Eqs. 7.3 and 7.4 are  $k_1$  and  $k_2$  respectively, one can write the change of those state variables according to Eq. 7.3 and Eq. 7.4 as

$$\frac{\partial C_{\text{Mg}}}{\partial t} = \nabla \cdot (D_{\text{Mg}}^\epsilon \nabla C_{\text{Mg}}) - k_1 C_{\text{Mg}} + k_2 C_{\text{Film}} [\text{Cl}]^2 \quad (7.7)$$

$$\frac{\partial C_{\text{Film}}}{\partial t} = k_1 C_{\text{Mg}} - k_2 C_{\text{Film}} [\text{Cl}]^2. \quad (7.8)$$

We assumed that the concentration of the chloride ions is constant (denoted by  $[\text{Cl}]$  in the equation) and does not diffuse into the protective film. The missing part of the model described by Eqs. 7.7 and 7.8 is the effect of the protective film on the reduction of the degradation rate. To this end, we defined a saturation term,  $(1 - \frac{C_{\text{Film}}}{[C_{\text{Film}}]_{\text{max}}})$  for the concentration of Mg ions in the equations. By considering the film's porosity ( $\epsilon$ ), the maximum concentration of the protective layer can be calculated based on its density ( $\rho_{\text{Mg(OH)}_2}$ ):

$$[C_{\text{Film}}]_{\text{max}} = \rho_{\text{Mg(OH)}_2} \cdot (1 - \epsilon). \quad (7.9)$$

The defined saturation term acts as a function of space that varies between 0

and 1 in each point. By adding this term to the concentration of Mg ions, we can write

$$\frac{\partial C_{\text{Mg}}}{\partial t} = \nabla \cdot (D_{\text{Mg}}^e \nabla C_{\text{Mg}}) - k_1 C_{\text{Mg}} \left( 1 - \frac{C_{\text{Film}}}{[\text{Film}]_{\max}} \right) + k_2 C_{\text{Film}} [\text{Cl}]^2 \quad (7.10)$$

$$\frac{\partial C_{\text{Film}}}{\partial t} = k_1 C_{\text{Mg}} \left( 1 - \frac{C_{\text{Film}}}{[\text{Film}]_{\max}} \right) - k_2 C_{\text{Film}} [\text{Cl}]^2. \quad (7.11)$$

Since the film is a porous layer and allows the ions to diffuse through it, the diffusion coefficient in Eq. 7.10 is a function of space and not a constant value (which is the reason for being denoted as  $D_{\text{Mg}}^e$ ). We can calculate this effective diffusion function by interpolating two values at any point: 1)  $D_{\text{Mg}}^e = D_{\text{Mg}}$  when  $C_{\text{Film}} = 0$ , and 2)  $D_{\text{Mg}}^e = \frac{\epsilon}{\tau} D_{\text{Mg}}$  when  $C_{\text{Film}} = [\text{Film}]_{\max}$ , in which  $\epsilon$  and  $\tau$  are the porosity and tortuosity of the protective film, respectively. The interpolation leads to the effective diffusion function:

$$D_{\text{Mg}}^e = D_{\text{Mg}} \left( \left( 1 - \frac{C_{\text{Film}}}{[\text{Film}]_{\max}} \right) + \frac{C_{\text{Film}}}{[\text{Film}]_{\max}} \frac{\epsilon}{\tau} \right). \quad (7.12)$$

### 7.2.3 Level set method

The level set method is a methodology that allows moving interfaces to be described by an implicit function. In other words, the boundaries of domains can be tracked as a function instead of being explicitly defined. In the level set method, a signed distance function,  $\phi = \phi(x, y, z, t)$ , describes the distance of each point in space to the interface, and the zero iso-contour of this function implies the interface [61]. In the current study, this function was defined in a way that divides the domain into two subdomains: 1) the bulk material, in which the implicit function is positive ( $\phi > 0$ ), and 2) the medium, in which the function is negative ( $\phi < 0$ ). The interface is defined as the points in space where  $\phi = 0$ . Fig. 7.2 shows a schematic representation of the solid-medium interface in the current study, in which the interface moves as the material degrades over time.

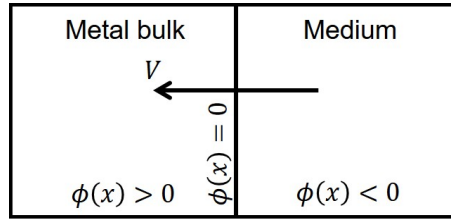


Figure 7.2: A schematic representation of the implicit function definition in the current study.  $V$  denotes the shrinkage speed of the interface due to degradation.

The level set equation defines this implicit function. The full level set equation can be written as [61]:

$$\frac{\partial \phi}{\partial t} + \underbrace{\vec{V^E} \cdot \nabla \phi}_{\text{External velocity field}} + \underbrace{V^N |\nabla \phi|}_{\text{Normal direction motion}} = \underbrace{b\kappa |\nabla \phi|}_{\text{Curvature - dependent term}} \quad (7.13)$$

in which the terms correspond to temporal changes, external velocity field effect, normal direction motion, and curvature-dependent interface movement, respectively.  $\vec{V^E}$  is the external velocity field, and  $V^N$  is the magnitude of the interface velocity along the normal axis. In practical usage, some of the terms are neglected. In this study, perfusion (rotation of the liquid around the bulk sample) is not considered, and the degradation rate does not depend on the curvature of the interface. As a result, by assuming that the interface moves in normal direction only, Eq. 7.13 can be simplified to

$$\frac{\partial \phi}{\partial t} + V^N |\nabla \phi| = 0 \quad (7.14)$$

where  $V^N$  is depicted in Fig. 7.2. The RankineHugoniot equation can be used to calculate the interface velocity in mass transfer problems [66]:

$$\{\mathbf{J}(x, t) - (c_{\text{sol}} - c_{\text{sat}}) \mathbf{V}(x, t)\} \cdot n = 0 \quad (7.15)$$

in which  $\mathbf{J}$  is the mass flux,  $c_{\text{sol}}$  is the concentration of the material in the bulk part (i.e. its density), and  $c_{\text{sat}}$  is the concentration at which the material (here, the ions) saturates through the medium. So, for the investigated Mg

degradation problem, Eq. 7.15 will be:

$$D_{\text{Mg}}^e \nabla_n C_{\text{Mg}} - ([\text{Mg}]_{\text{sol}} - [\text{Mg}]_{\text{sat}}) V^N = 0. \quad (7.16)$$

Inserting the obtained velocity of Eq. 7.16 into Eq. 7.14 and considering the direction of the shrinkage velocity, which is in the opposite direction of the surface normal vector, yields

$$\frac{\partial \phi}{\partial t} - \frac{D_{\text{Mg}}^e \nabla_n C_{\text{Mg}}}{[\text{Mg}]_{\text{sol}} - [\text{Mg}]_{\text{sat}}} |\nabla \phi| = 0. \quad (7.17)$$

Eq. 7.17 is the final formulation of the level set equation in the current study, which alongside Eqs. 7.10 and 7.11 forms the mathematical model of degradation of Mg with a moving interface. Eq. 7.17 contributes indirectly to the evolution of Eqs. 7.10 and 7.11 as it defines the boundary, the zero iso-contour of the  $\phi$  function, on which the boundary conditions of the equations are applied.

### 7.3 Methodology of model implementation

The developed mathematical model comprised of Eqs. 7.10, 7.11, and 7.17 cannot be solved using analytical techniques. The alternative approach in these scenarios is solving the derived PDEs numerically. In this study, we used a combination of finite element and finite difference methods to solve the aforementioned equations. In the developed numerical model, the PDEs are solved one by one, each of which is a linear equation, so the model implementation follows the principles of solving linear systems. In the following section, only the process to obtain the solution of Eq. 7.10 is described in detail, but the other PDEs were solved using the same principle. Although the adopted finite element method is standard, we elaborate on its derivation to clarify the bottlenecks of the later-discussed implementation.

### 7.3.1 Finite element discretization (bottleneck of the algorithm)

In order to solve Eq. 7.10 numerically, we used a finite difference scheme for the temporal term and a finite element formulation for the spatial terms. For simplicity of writing, notations of variables are changed, so  $C_{\text{Mg}}$  is represented as  $u$  (the main unknown state variable to find),  $C_{\text{Film}}$  is denoted by  $p$ ,  $[\text{Cl}]$  is denoted by  $q$ , and the saturation term  $(1 - \frac{F}{F_{\max}})$  is denoted by  $s$ . By doing this, Eq. 7.10 can be written as

$$\frac{\partial u}{\partial t} = \nabla \cdot (D \nabla u) - k_1 s u + k_2 p q^2. \quad (7.18)$$

To obtain the finite element formulation, the weak form of derived PDE is required. In order to get this, we define a space of test functions and then, multiply each term of the PDE by any arbitrary function as a member of this space. The test function space is

$$\mathcal{V} = \left\{ v(\mathbf{x}) | \mathbf{x} \in \Omega, v(\mathbf{x}) \in \mathcal{H}^1(\Omega), \text{ and } v(\mathbf{x}) = 0 \text{ on } \Gamma \right\} \quad (7.19)$$

in which the  $\Omega$  is the domain of interest,  $\Gamma$  is the boundary of  $\Omega$ , and  $\mathcal{H}^1$  denotes the Sobolev space of the domain  $\Omega$ , which is a space of functions whose derivatives are square-integrable functions in  $\Omega$ . The solution of the PDE belongs to a trial function space, which is similarly defined as

$$\mathcal{S}_t = \left\{ u(\mathbf{x}, t) | \mathbf{x} \in \Omega, t > 0, u(\mathbf{x}, t) \in \mathcal{H}^1(\Omega), \text{ and } \frac{\partial u}{\partial n} = 0 \text{ on } \Gamma \right\}. \quad (7.20)$$

Then, we multiply Eq. 7.18 to an arbitrary function  $v \in \mathcal{V}$ :

$$\frac{\partial u}{\partial t} v = \nabla \cdot (D \nabla u) v - k_1 s u v + k_2 p q^2 v. \quad (7.21)$$

Integrating over the whole domain yields:

$$\int_{\Omega} \frac{\partial u}{\partial t} v d\omega = \int_{\Omega} \nabla \cdot (D \nabla u) v d\omega - \int_{\Omega} k_1 s u v d\omega + \int_{\Omega} k_2 p q^2 v d\omega. \quad (7.22)$$

The diffusion term can be split using the integration by parts technique:

$$\int_{\Omega} \nabla \cdot (D \nabla u) v d\omega = \int_{\Omega} \nabla \cdot [v(D \nabla u)] d\omega - \int_{\Omega} (\nabla v) \cdot (D \nabla u) d\omega \quad (7.23)$$

in which the second term can be converted to a surface integral on the domain boundary by applying the Green's divergence theory:

$$\int_{\Omega} \nabla \cdot [v(D \nabla u)] d\omega = \int_{\Gamma} Dv \frac{\partial u}{\partial n} d\gamma. \quad (7.24)$$

For the temporal term, we use the finite difference method and apply a first-order backward Euler scheme for discretization, which makes it possible to solve the PDE implicitly:

$$\frac{\partial u}{\partial t} = \frac{u - u^n}{\Delta t} \quad (7.25)$$

where  $u^n$  denotes the value of the state variable in the previous time step (or initial condition for the first time step). Inserting Eqs. 7.23, 7.24, and 7.25 into Eq. 7.22 yields:

$$\int_{\Omega} \frac{u - u^n}{\Delta t} v d\omega = \int_{\Gamma} Dv \frac{\partial u}{\partial n} d\gamma - \int_{\Omega} D \nabla u \cdot \nabla v d\omega - \int_{\Omega} k_1 s u v d\omega + \int_{\Omega} k_2 p q^2 v d\omega. \quad (7.26)$$

The surface integral is zero because there is a no-flux boundary condition on the boundary of the computational domain (defined in the trial function space according to Eq. 7.20). By reordering the equation, we get the weak form of Eq. 7.18:

$$\int_{\Omega} u v d\omega + \int_{\Omega} \Delta t D \nabla u \cdot \nabla v d\omega + \int_{\Omega} \Delta t k_1 s u v d\omega = \int_{\Omega} u^n v d\omega + \int_{\Omega} \Delta t k_2 p q^2 v d\omega. \quad (7.27)$$

So, the problem is finding a function  $u(t) \in \mathcal{S}_t$  such that for all  $v \in \mathcal{V}$  Eq. 7.27 would be satisfied. By defining a linear functional  $(f, v) = \int_{\Omega} f v d\omega$  and encapsulating the independent concentration terms into  $f^n = pq^2$ , Eq. 7.27 can be simplified as:

$$(u, v)[1 + \Delta t k_1 s] + \Delta t (D \nabla u, \nabla v) = (u^n, v) + \Delta t (f^n, v) \quad (7.28)$$

which can be further converted to the common form of the weak formulation of time-dependent reaction-diffusion PDEs by multiplying to a new coefficient

$$\alpha = \frac{1}{1 + \Delta t k_1 s}:$$

$$(u, v) + \alpha \Delta t (D \nabla u, \nabla v) = \alpha (u^n, v) + \alpha \Delta t (f^n, v). \quad (7.29)$$

One can approximate the unknown function  $u$  in Eq. 7.29 by  $u(x) \approx \sum_{i=0}^N c_i \psi_i(x)$ , where the  $\psi_i$  are the basis functions used to discretize the function space, and  $c_0, \dots, c_N$  are the unknown coefficients. The finite element method uses Lagrange polynomials as the basis function and discretizes the computational domain using a new function space  $\mathcal{V}_h$  spanned by the basis functions  $\{\psi_i\}_{i \in \mathcal{I}_s}$ , in which  $\mathcal{I}_s$  is defined as  $\mathcal{I}_s = \{0, \dots, N\}$ , where  $N$  denotes the degrees of freedom in the computational mesh. The computational mesh discretizes the space into a finite number of elements, in each of which the  $\psi_i$  is non-zero inside the  $i$ th element and zero everywhere else. In this study, 1st order Lagrange polynomials were used as the basis functions to define the finite element space.

For 1D elements, a 1st order Lagrange polynomial for the  $i$ th element with the width of  $h$  can be written as:

$$\psi_i(x) = \begin{cases} 0 & x < x_{i-1} \\ (x - x_{i-1}) / h & x_{i-1} \leq x < x_i \\ 1 - (x - x_i) / h & x_i \leq x < x_{i+1} \\ 0 & x \geq x_{i+1} \end{cases}. \quad (7.30)$$

A similar approach can be applied to define the basis function space in 2D and 3D spaces.

In order to derive a linear system of equations for obtaining the unknown coefficients  $c_j$ , we define

$$u = \sum_{j=0}^N c_j \psi_j(x), \quad u^n = \sum_{j=0}^N c_j^n \psi_j(x) \quad (7.31)$$

as the definition of the unknown function  $u$  and its value in the previous time step  $u^n$ . We then insert it into Eq. 7.29, which yields the following equation for each degree of freedom  $i = 0, \dots, N$ , where the test functions are selected as

$$v = \psi_i:$$

$$\sum_{j=0}^N (\psi_i, \psi_j) c_j + \alpha \Delta t \sum_{j=0}^N (\nabla \psi_i, D \nabla \psi_j) c_j = \sum_{j=0}^N \alpha (\psi_i, \psi_j) c_j^n + \alpha \Delta t (f^n, \psi_i). \quad (7.32)$$

Eq. 7.32 is a linear system

$$\sum_j A_{i,j} c_j = b_i \quad (7.33)$$

with

$$A_{i,j} = (\psi_i, \psi_j) + \alpha \Delta t (\nabla \psi_i, D \nabla \psi_j) \quad (7.34)$$

$$b_i = \sum_{j=0}^N \alpha (\psi_i, \psi_j) c_j^n + \alpha \Delta t (f^n, \psi_i) \quad (7.35)$$

which can also be rewritten as

$$(M + \alpha \Delta t K) c = \alpha M c_1 + \alpha \Delta t f. \quad (7.36)$$

$M$  (which traditionally is called the mass matrix),  $K$  (which traditionally is called the stiffness matrix),  $f$ ,  $c$ , and  $c_1$  are defined as

$$\begin{aligned} M &= \{M_{i,j}\}, \quad M_{i,j} = (\psi_i, \psi_j), \quad i, j \in \mathcal{I}_s \\ K &= \{K_{i,j}\}, \quad K_{i,j} = (\nabla \psi_i, D \nabla \psi_j), \quad i, j \in \mathcal{I}_s \\ f &= \{f_i\}, \quad f_i = (f(x, t_n), \psi_i), \quad i \in \mathcal{I}_s \\ c &= \{c_i\}, \quad i \in \mathcal{I}_s \\ c_1 &= \{c_i^n\}, \quad i \in \mathcal{I}_s \end{aligned} \quad (7.37)$$

By solving Eq. 7.33 and substituting the obtained  $c$  in Eq. 7.31,  $u$  ( $C_{\text{Mg}}$  in the example in this study) can be calculated in the current time step. As stated before, the same approach can be applied to Eq. 7.11 and Eq. 7.17 to get  $C_{\text{Film}}$  and  $\phi$ . This procedure is repeated in each time step to compute the values of  $C_{\text{Mg}}$ ,  $C_{\text{Film}}$ , and  $\phi$  over time.

A common practice to save time for solving Eq. 7.33 for a constant time step size is to compute the left-hand side matrix ( $A$  in Eq. 7.34) once and compute only

the right-hand side vector of the equation at each time iteration. But in this case, although the time step size is fixed, due to the presence of the  $\alpha$  coefficient, the matrix changes along the time. The  $\alpha$  coefficient is not constant and should be updated in each time step because it depends on the penalization term  $s$  (which is a function of the concentration of the film as can be seen by comparing Eq. 7.10 and Eq. 7.18). In addition to this, the diffusion coefficient is not constant (Eq. 7.12), making the second term in Eq. 7.34 non-constant even in the absence of  $\alpha$  coefficient. Consequently, the left-hand side matrix of the Eq. 7.33 cannot be computed before the start of the main time loop, and computing it in each time step is an extra but inevitable computational task in comparison to similar efficient and high-performance finite element implementations. This contributes to a slower algorithm for solving the aforementioned PDEs.

### 7.3.2 Implementation and parallelization

The model was implemented in FreeFEM [67], which is an open-source PDE solver to facilitate converting the weak formulation (Eq. 7.27) to a linear system  $Ax = b$  (with  $A$  from Eq. 7.34 and  $b$  from Eq. 7.35). The computational mesh was generated using Netgen [72] in the SALOME platform [73] by a set of linear tetrahedral elements, and all the other preprocessing steps were performed in FreeFEM. The mesh was adaptively refined on the material-medium interface in order to increase the accuracy of the level set model. Postprocessing of the results was carried out using Paraview [119].

Computing the diffusion solely in the medium domain causes oscillations close to the interface, and to prevent this, the mass lumping feature of FreeFEM was employed. In this technique, the desired mass matrix is handled node-wise and not element-wise. Technically speaking, this means that the state variable is stored in the mesh nodes, and although this is the natural formulation in the finite difference method, it requires artificial modification in the standard finite element formulation [120]. The mass lumping feature of FreeFEM applies a quadratic formula at the vertices of elements to make the mass matrix diagonal, which contributes positively to the convergence of the solution.

The main parallelization approach for the current study was domain decomposition, in which the mesh is split into smaller domains (can be overlapping or non-overlapping), and the global solution of the linear system is achieved by solving the problem on each smaller local mesh. What really matters in this approach is providing virtual boundary conditions to the smaller sub-

domains by ghost elements, transferring neighboring sub-domain solutions [121]. As a result, a high-performance parallelism is feasible by assigning each sub-domain to one processing unit.

In computational science, preconditioning is widely used to enhance the convergence, which means instead of directly working with a linear system  $Ax = b$ , one can consider the preconditioned system [122]:

$$M^{-1}Ax = M^{-1}b \quad (7.38)$$

in which the  $M^{-1}$  is the preconditioner. In the current study, we considered this approach for both the domain composition and the solution of the linear system. We opted to use an overlapping Schwarz method for domain decomposition, in which the mesh is first divided into a graph of  $N$  non-overlapping meshes using METIS (or ParMETIS) [123]. Then, by defining a positive number  $\delta$ , the overlapping decomposition  $\{\mathcal{T}_i^\delta\}_{1 \leq i \leq N}$  can be created recursively for each sub-mesh  $\{\mathcal{T}_i\}_{1 \leq i \leq N}$  by adding all adjacent elements of  $\mathcal{T}_i^{\delta-1}$  to it. Then, the finite element space  $\mathcal{V}_h$  (Eq. 7.19) can be mapped to the local space  $\{\mathcal{V}_i^\delta\}_{1 \leq i \leq N}$  by considering the restrictions  $\{R_i\}_{1 \leq i \leq N}$  and a local partition of unity  $\{D_i\}_{1 \leq i \leq N}$  such that:

$$\sum_{j=1}^N R_j^\top D_j R_j = I_{n \times n} \quad (7.39)$$

where  $I$  and  $n$  denote identity matrix and the global number of unknowns, respectively [124].

In this study, we decomposed the mesh by using the one-level preconditioner Restricted Additive Schwarz (RAS):

$$M_{\text{RAS}}^{-1} = \sum_{i=1}^N R_i^\top D_i A_i^{-1} R_i \quad (7.40)$$

in which  $\{A_i\}_{1 \leq i \leq N}$  is the local operator of the sub-matrices [124]. For this purpose, we took advantage of the HPDDM (high-performance domain decomposition methods) package interface in FreeFEM [71]. The partitioned mesh is shown in Fig. 7.3. The effect of the construction of these local sub-domains on the sparsity pattern of the global matrix is also depicted in Fig. 7.4. The global matrix is a sparse matrix according to Eq. 7.34 and the definition of the basis function  $\psi$ .

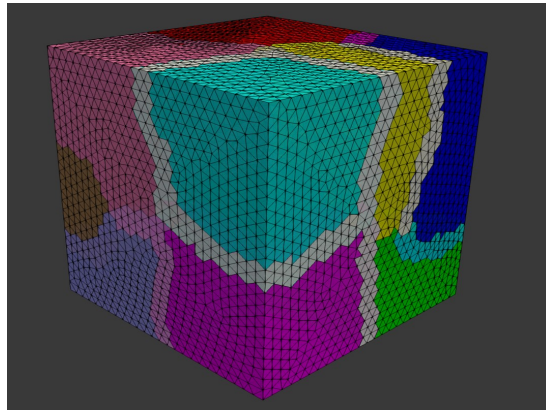


Figure 7.3: Overlapping domain decomposition in the current study. Each color shows a separate sub-domain, and the narrow lighter bands are the overlapped regions.

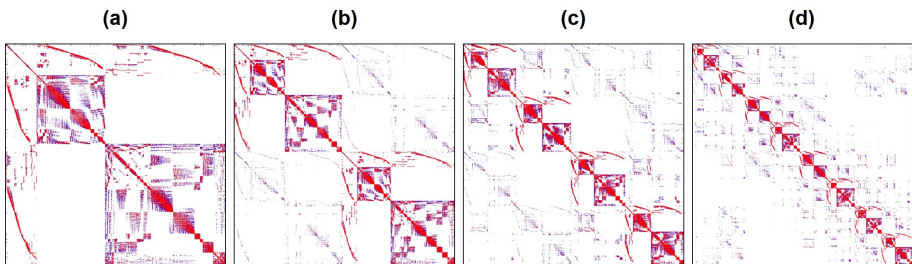


Figure 7.4: Comparison of the sparsity patterns (highlighting non-zero elements) of the global matrix  $A$  for a different number of decomposed domains a: 1 domain b: 2 sub-domains c: 4 sub-domains d: 8 sub-domains.

Generally, two categories of methods have been used to solve a large linear system of equations on parallel machines: direct solvers (e.g. Multifrontal Massively Parallel Sparse, MUMPS [125]) and iterative solvers (e.g. Generalized Minimal Residual Method, GMRES [69]). While direct solvers are quite robust, they suffer from the memory requirement problem on large systems. Inversely, iterative solvers are quite efficient on memory consumption, but similar to other iterative approaches, they are not very reliable in some cases [126]. Direct solvers modify the matrix by factorization (e.g. Cholesky

decomposition), but an iterative solver does not manipulate the matrix and works solely using basic algebraic operations. However, for an efficient usage of iterative solvers, a proper preconditioner is crucial [126]. By evaluating and comparing the performance of the aforementioned methods for the current model, we decided to use an iterative approach using the Krylov subspaces (KSP) method, in which we preconditioned the equation using a proper preconditioner (Eq. 7.38) and then solved it with an iterative solver.

Krylov methods have been frequently used by researchers as robust iterative approaches to parallelism [127]. What matters in this regard is ensuring proper scaling of the parallelized algorithm for both the assembling of the matrices and the solution of the linear system of equations. One good solution to this challenge is taking advantage of HPC-ready mathematical libraries to achieve efficient distributed-memory parallelism through the Message Passing Interface (MPI). In the current study, we used the PETSc (Portable, Extensible Toolkit for Scientific Computation) library [70], which provides a collection of high-performance preconditioners and solvers for this purpose.

In order to yield the highest performance, a variety of different combinations of KSP types and preconditioners were evaluated, such as Conjugate Gradients (CG) [128], Successive Over-Relaxation (SOR) [129], block Jacobi, and Algebraic Multigrid (AMG) [130], to name a few. The performance tests results are presented in the supplementary materials of this paper. The best performance for the reaction-diffusion system model was achieved using the HYPRE preconditioner [68] and the GMRES solver [69]. This was the combination used for all the performance analysis tests.

### 7.3.3 Level set issues

As mentioned before, in order to track the interface of the bulk material and the surrounding fluid, an implicit signed distance function is defined as the solution of Eq. 7.17. This equation can be solved using the aforementioned finite element discretization, but in a practical implementation, there are usually a couple of problems associated with this PDE.

The first issue is defining  $D_{\text{Mg}}^e$  and  $\nabla_n C_{\text{Mg}}$  on the moving interface. To ensure correct boundary conditions for Eq. 7.16, the value of  $C_{\text{Mg}}$  is set constant on the whole bulk material by using the penalty method. As a result, the implicit interface is not necessarily aligned on the computational mesh. Although

this is a beneficial fact for the interface tracking, it inserts the problem of overestimation of  $C_{\text{Mg}}$  on the nodes close to the interface, which makes it difficult to calculate  $\nabla_n C_{\text{Mg}}$  on these nodes correctly. The same problem exists for calculating  $D_{\text{Mg}}^e$ . To overcome this issue, the values of  $C_{\text{Mg}}$  and  $D_{\text{Mg}}^e$  are calculated at the distance  $h$  from the interface in the normal direction (towards the medium), where  $h$  is the edge size of the smallest element of the computational mesh.

The next issue is a well-known problem of the level set method: if the velocity of the interface is not constant (as in Eq. 7.13), the level set function  $\phi$  may become distorted by having too flat or too steep gradients close to the moving front. This could cause unwanted movements of the interface. The problem becomes even worse when the distance function is advected. A solution to this issue is re-initializing the distance function in each time step (re-distancing), but this operation requires solving a new PDE. From numerical investigations, it has been observed that this operation inserts new errors in the numerical computation of the level set equation [131]. This can be resolved by improving the method of reconstruction of the distance function [131].

However, re-initialization results in another issue on a massively parallel implementation: as the mesh is partitioned into smaller sub-meshes, it is not feasible anymore to evaluate the distance to the interface globally on each sub-domain. As a result, the inverse process of domain decomposition should be taken to assemble the mesh again. This can be done by the restriction matrix and the partition of unity (defined in Eqs. 7.39 and 7.40), but it is rather a very inefficient procedure regarding the parallelization of the simulation and results in a long execution time in each time step.

In the current study, the distance function  $\phi$  was initialized only once at the beginning of the simulation. The re-initialization process was unnecessary in this case because according to Eq. 7.17, the distance function is advected only in the regions where there is a gradient of the concentration of Mg ions, which means that advection is applied only on the regions close to the interface in the medium. This prevented the whole distance function of being distorted, and as a result, it was not required to re-initialize it in each time step. This also removed the need for inverting the decomposition process.

### 7.3.4 Simulation setup

In order to verify the performance of the developed model, a degradation experiment was reconstructed in-silico, in which the degradation of a block of Mg (with the size of  $13mm \times 13mm \times 4mm$ ) was investigated in a simulated body fluid solution. All the experimental parameter data (used to setup the simulation), as well as the degradation rates (used to calibrate and validate the numerical model) were extracted from [22].

As can be seen in Eqs. 7.1 and 7.2, each mole removed from the Mg block corresponds to one mole of the produced hydrogen. As a result, instead of a direct measurement of mass loss, one can collect and measure the amount of produced hydrogen to monitor the degradation rate. This is a common way of reporting degradation in this type of studies [132]. In order to get this quantity out of the developed model, we used the level set model output. The total mass loss of Mg at each desired time can be calculated based on the movement of the corrosion front:

$$\text{Mg}_{\text{lost}} = \int_{\Omega_+(t)} \text{Mg}_{\text{solid}} dV - \int_{\Omega_+(0)} \text{Mg}_{\text{solid}} dV \quad (7.41)$$

where  $\Omega_+(t) = \{\mathbf{x} : \phi(\mathbf{x}, t) \geq 0\}$ . It is worth noting that this integration should be performed by ignoring the ghost elements generated in the mesh partitioning process, otherwise the calculated material loss will be higher than the real value. Then, the amount of formed hydrogen gas can be calculated based on the ideal gas law:

$$H_f = \frac{\text{Mg}_{\text{lost}}}{\text{Mg}_{\text{mol}}} \frac{RT}{PA} \quad (7.42)$$

in which  $R$  is the universal gas constant,  $P$  is the pressure,  $T$  is the solution temperature,  $A$  is the exposed corrosion surface area (which can be computed using the level set function), and  $\text{Mg}_{\text{mol}}$  is the molar mass of Mg. Plotting a comparison of the predicted and experimentally obtained values of hydrogen can show the overall validity of the mathematical model because both the diffusion-reaction equations and the level set equation contribute to the prediction made by the computational model.

The geometry of the simulation experiment is depicted in Fig. 7.5. Based on this geometry, an Eulerian computational mesh was constructed by generating

tetrahedral elements on the whole domain, including the Mg block and the medium. This resulted in 830,808 elements with a total of 143,719 DOFs for each PDE (Eqs. 7.10, 7.11, and 7.17), which indicates the size of matrix  $A$  in Eq. 7.34. Model parameters and material properties were obtained from [55]. The diffusion coefficient of Mg was calculated using an inverse problem setup in which a Bayesian optimization process [74] was used to run the simulation code multiple times and minimize the difference of the model output and the experimental data reported by [22]. A time step convergence study was performed to measure the sensitivity of the model to the time stepping parameter, and based on the results, the time step value was set to 0.025 hours.

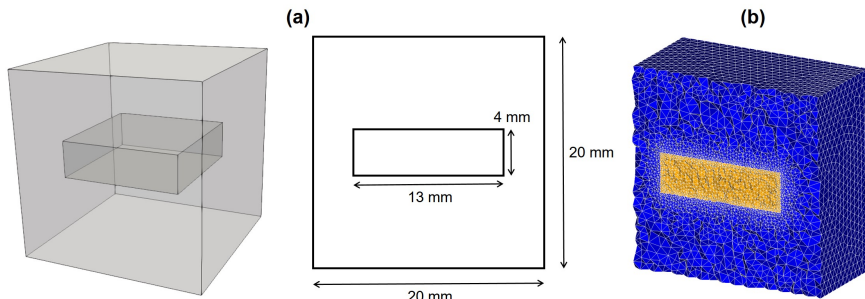


Figure 7.5: Representation of the experimental set-up simulated to perform numerical validation of the developed model and evaluate parallel performance. a) A cuboid of Mg (with the size of  $13\text{mm} \times 13\text{mm} \times 4\text{mm}$ ) is floating inside a simulated body fluid solution to investigate the degradation process, b) a cross-section of the computational mesh, refined on the metal-medium interface to increase the interface capturing accuracy.

### 7.3.5 Performance analysis

To investigate the performance and scaling behavior of the implemented parallel code, we conducted a set of weak-scaling and strong-scaling tests on the computational model. To do this, the time required to solve each PDE in each time step was measured in a simulation. This acted as a rough estimation of the time required in each time step because it ignores all the other factors contributing to speedup results such as communication costs, load imbalance, limited memory bandwidth, and parallelization-caused overhead.

Weak-scaling was evaluated by dividing the computational domain into smaller sub-domains (each of which was  $\frac{1}{16}$  of the whole domain, Fig. 7.6) and conducting simulation experiments with 1, 2, 4, and 8 computational cores in a way that the number of processors corresponded to the number of employed sub-domains. In Fig. 7.6 the upper row shows different domains as an accumulation of the smaller divisions, and the lower row shows the corresponding domain decomposition for parallel computing by depicting each processing unit in a different color. In fact, it demonstrates the concept of increasing the number of MPI processing units as we increase the size of the problem.

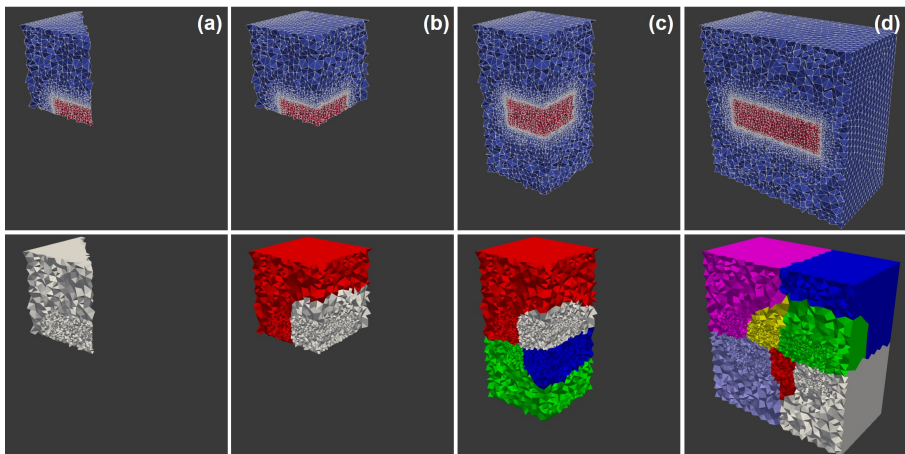


Figure 7.6: Models used for weak-scaling, in which the number of elements was doubled each time while doubling the number of computational cores. Upper row: actual computational domain in which colors show the medium (blue) and the material block (red). Lower row: domain decomposition for parallelization, colors show different decomposed mesh parts (distributed to different MPI processing units). Each column corresponds to a different simulation with a: 1 MPI unit, b: 2 MPI units, c: 4 MPI units, and d: 8 MPI units.

After calculating the speedup of each test (by comparing the differences in execution time), we can use Gustafsons law [133] to calculate the sequential and parallelizable portion of computation in the current implementation in weak-scaling evaluation:

$$\text{Speedup} = f + (1 - f) \times N \quad (7.43)$$

where  $N$  is the total number of computational cores,  $f$  is the fraction of operations in the computation that are sequential, and as a result,  $1 - f$  is the fraction of the execution time spent on the parallelizable part.

The strong-scaling evaluation was performed using the entire domain. The evaluation was done using 1, 8, 16, 40, 60, 90, 200, and 300 MPI cores. In strong-scaling, Amdahls law [134] is used to calculate the portion of the algorithm that runs in parallel:

$$\text{Speedup} = \frac{1}{f + \frac{1-f}{N}} \quad (7.44)$$

in which the parameters are the same as Eq. 7.43.

### 7.3.6 Compute environment

Simulations were conducted on the VSC (Flemish Supercomputer Center) supercomputer with the availability of Intel CPUs in three different micro-architectures: Ivy Bridge, Haswell, and Skylake. Due to a better performance, the strong and weak-scaling measurements were solely performed on the Skylake nodes. On this supercomputer, we made use of 3 nodes, 36 cores each, with 576 GB of the total memory, each node holding 2 Intel Xeon Gold 6132 CPUs with a base clock speed of 2.6 GHz. The supercomputer uses CentOS 7.6.1810 with kernel version 3.10.0. For interprocess communication, Intel's MPI implementation 2018 was used.

## 7.4 Results

### 7.4.1 Numerical simulation results

The performed numerical simulation produces the output of three main quantities: the concentration of the Mg ions in the medium (as the solution of Eq. 7.10), the concentration of the protective film (as the solution of Eq. 7.11), and the level set function values at each element (as the solution of Eq. 7.17). In addition to this, a quantitative prediction of the mass loss is also generated according to Eqs. 7.41 and 7.42.

In order to have quantitative predictions, the coefficients of Eqs. 7.10 and 7.11 (diffusion rates and reaction rates) should be calibrated using an inverse problem. Fig. 7.7 shows the results produced by the computational model after this parameter estimation stage. A narrow layer of the protective film is formed on the surface of the Mg block, and the volume of produced hydrogen gas is compared with values obtained from experiments. Additionally, by plotting the zero iso-contour of the level set function, we can obtain the shape of the material block as it degrades during the degradation process (i.e. tracking the moving corrosion front). This is depicted by the grey surface in Fig. 7.7.

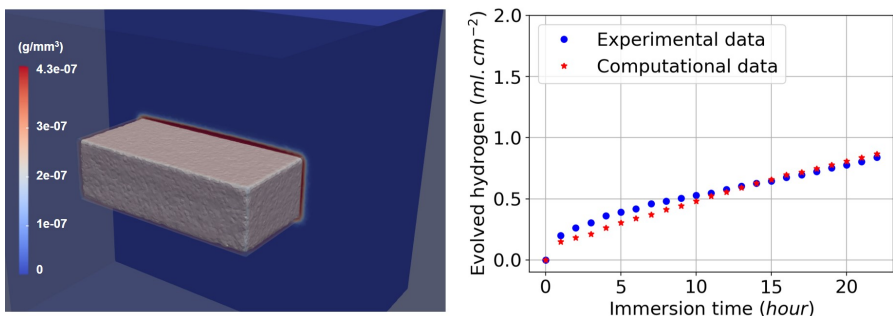


Figure 7.7: Numerical simulation result. Left: formation of a protective layer on the surface of the Mg block (red region). Right: comparison of the produced hydrogen (a surrogate for the material loss) in the computational model and the experimental data, which is a validation of the full model as both the reaction-diffusion equations and the level-set equation are involved in the computation of this quantity.

#### 7.4.2 Weak and strong scaling results

Weak-scaling results are plotted in Fig. 7.8, in which the execution time of each time step is broken down into the time spent on each PDE. The results show good scalability of the parallel implementation.

Speedup and parallel efficiency of the weak-scaling experiment is plotted in Fig. 7.9. By fitting a curve based on the Gustafson equation (Eq. 7.43) on the obtained results (Fig. 7.9), the sequential proportion of the current implementation was calculated to be 18%, which means that 82 percent of the code can be parallelized, which is a proper but not an ideal scalability.

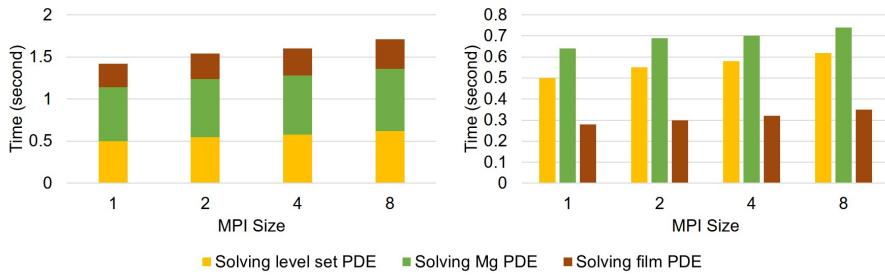


Figure 7.8: Weak-scaling test result. Results are broken down into contributions for each PDE, which are plotted cumulatively and separately in the left and right plot, respectively.

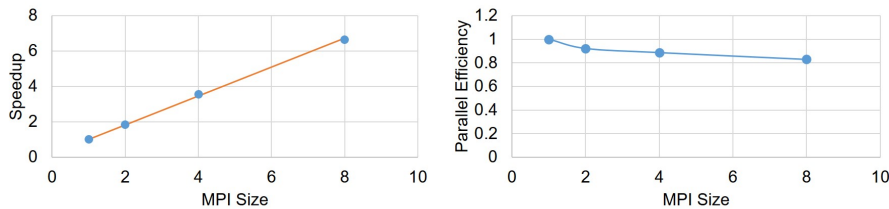


Figure 7.9: Speed-up and parallel efficiency of the weak-scaling experiment. The orange line in the left plot shows the fitted curve based on the Gustafson equation.

The strong-scaling results are plotted in Fig. 7.10, which shows a better scalability in comparison to the weak-scaling test. For a better representation, exact measured values are presented in Table 7.1.

Table 7.1: Strong-scaling test result, presented by the execution time of each PDE in simulations with a different number of employed MPI cores.

MPI Size	1	8	16	40	60	90	200	300
Solution time of each time step (s)	LS PDE	9	1.39	0.75	0.36	0.26	0.19	0.11
	Mg PDE	13.04	1.76	0.94	0.46	0.31	0.22	0.12
	Film PDE	6.38	0.84	0.45	0.21	0.14	0.09	0.05
Total time (s)	28.42	3.99	2.14	1.03	0.71	0.5	0.28	0.2

Similar to weak-scaling results, Fig. 7.11 demonstrates the speedup and parallel

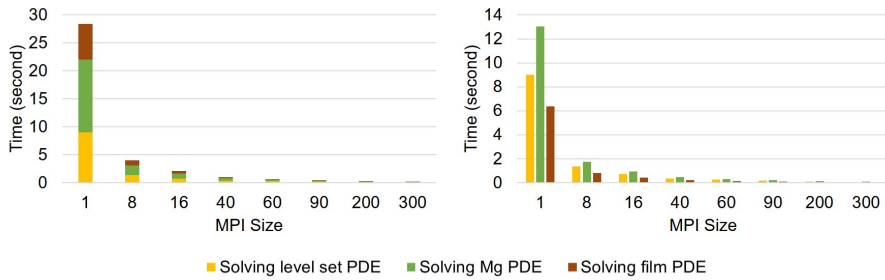


Figure 7.10: Strong-scaling test result. Results are broken down into contributions for each PDE, which are plotted cumulatively and separately in the left and right plot, respectively.

efficiency of the developed code for strong-scaling evaluation. From the results, it is obvious that increasing the number of cores leads to a better performance but a lower efficiency. By fitting Amdahls equation (Eq. 7.44) on the obtained speedup results (Fig. 7.11),  $f$  was obtained as 0.01, which means in strong-scaling terms that 99% of the code can run in parallel.

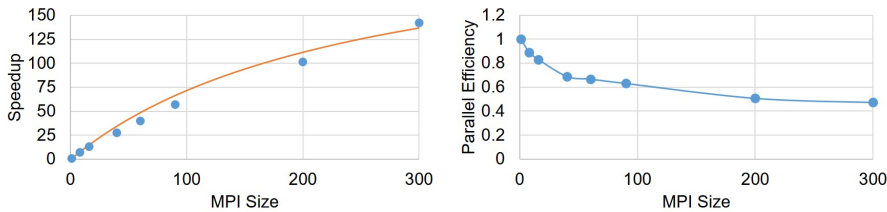


Figure 7.11: Speed-up and parallel efficiency of the strong-scaling experiment. The orange line in the left plot is the fitted equation based on the Amdahl rule.

## 7.5 Discussion

In this investigation, the derivation and implementation of a reaction-diffusion model with moving boundaries were presented. Such an approach finds application in many scientific and engineering problems. The target application in the current work was the degradation of a bulk metal cuboid in a liquid environment, specifically Mg in an aqueous ion solution as a representative

for temporary medical devices. The simulations were based on the corrosion of Mg metal to Mg ions to form a film of Mg hydroxide that partially protects the metal block from further degradation except where this film is impacted by reaction with other ions in the environment (such as chloride ion). The reactive moving boundary problem was cast in the form of equations in which the change of the concentrations of the different chemical components is represented by parabolic PDEs. The coupled equations depend on several kinetic constants that have been calibrated from experiments. The moving interface between the metal bulk and the liquid phase was described by an implicit function using the level set method. The derivation led to equations that require the use of numerical techniques for which a combination of finite difference and finite element methods was implemented. As the required high accuracy on the moving interface results in an increase in computation time, parallelization was crucial for the computational model to decrease the execution time of the simulations. The results of the total execution time in each time step (Table 7.1) clearly indicate that without the parallelization, the simulation of the model is slow and as a result, less interactable for real-world simulation analyses. Considering the properly employed parallelization, the computational time has been decreased noticeably for the investigated case-study.

The output of the conducted numerical simulation demonstrates that the developed mathematical model is capable of capturing the degradation interface movement and of modeling of the underlying chemical phenomena. The predicted mass loss is in line with the experimental results, and the simulated corrosion behavior is as expected for such a system. It is worth noting that the chosen system is highly idealized as a model for medical devices. A more realistic chemical environment would contain many more species that play a role in the formation of either soluble ions or the protective film. Moreover, in real-world scenarios, corrosion occurs in a more complex way than the simplified one described in this paper, which will have a significant influence on the local concentration of ions in the regions close to the solid surface. Nevertheless, the developed framework is capable of capturing these physical and chemical phenomena in the future by simply adding the appropriate terms to the base PDEs without any major changes in the computational model. Furthermore, although it requires some changes to the parallelization approach, the addition of the fluid flow around the block is feasible by adding convective terms to form a reaction-diffusion-convection system. Such a system can be used to model relevant systems such as experimental bioreactor setups

in biology and medical sciences.

The parallel algorithm was implemented using a domain decomposition method. Standard domain decomposition preconditioners, such as restricted additive Schwarz, are widely used for parallel implementation of computational models. In a parallel implementation, such preconditioners bring the benefit of relatively low communication costs [122]. Beside this, the formed linear system of equations in each partition of the mesh was solved using Krylov methods by taking advantage of the highly-efficient preconditioners and iterative solvers of the PETSc library. According to the obtained results, the employed parallelization approach of the current study yields reasonable scaling with respect to the available computational resources (or the number of sub-domains). Out of multiple evaluations, the best performance was achieved using the preconditioner/solver combination of HYPRE/GMRES, which is in agreement with findings in more specific studies in this regard [135].

To evaluate the scaling performance of the implemented parallelism, a set of weak and strong scaling tests was conducted. In weak-scaling, the main approach is changing the problem size proportional to the change in the available computing resources. In an ideal parallelization, we expect that the speedup remains the same for all the setups because we provide double resources as we double the size of the problem. In strong-scaling, the size of the problem remains constant, but the number of computing units increases. So, in an ideal case, we should observe a double speedup as the number of computing units doubles. By fitting Gustafson's and Amdahl's laws on the scaling test results (Figs. 7.9 and 7.11), the maximum parallelizable portion of the code was calculated to be 82% and 99% for the weak-scaling and strong-scaling tests, respectively. This is a reasonable theoretical scaling for both cases.

The obtained scaling behavior is similar to other conducted studies for diffusion or diffusion-convection systems [136, 137], in which the efficiency of the parallelization decreases with increasing the number of available computational resources. The reason behind this behavior in the current model lies in the mesh partitioning process. Indeed, the mesh is partitioned into semi-equal partitions, each of which has the same number of elements, but the main computation is only carried out on the nodes located outside the degrading material block (i.e. in the medium). In other words, the computational resources assigned to the nodes inside the material bulk do not contribute significantly to the simulation. This limitation can be prevented by modifying the mesh generation process in a way that a lower number

of elements be generated inside the material block, but doing this requires remeshing of the interior region as the moving interface approaches it, which imposes even more complexity to the algorithm due to the partitioned mesh. Another bottleneck of the current model, as discussed before, routed in the non-constant right-hand matrix of the linear system (Eq. 7.33), which requires computing the  $A$  matrix (Eq. 7.34) in each time step and leads to a slower execution time.

One important point in this regard is that the way that the results are interpreted does not necessarily imply the true scaling behavior of the system. Indeed, it is more like a surrogate model of the system performance. The correct methodology for obtaining true scaling factors is rather starting from an analysis of the code and time used in each routine for a non-parallel run. Then, based on the fraction of routines that are possible to execute in parallel, one can get a theoretical limit for the speedup. This will be reduced by practical limitations such as load balancing and communication costs of the network. Since it is a theoretical limit, it is not fully correct to ignore those extra parts and use the execution time to invert the relation to predict the fraction of the code that is parallel. However, for a complex computational model like the one that was developed in the current study, doing such a measurement of each routine is very difficult due to the complexity of the orchestrated libraries and tools. As a result, we were limited to use the roughly approximated speedup limit to evaluate the scaling of the constructed model. Regarding the scalability results, it is worth mentioning that although having studies with thousands of MPI ranks is more common in this field, due to the limitation we faced in accessing computational resources, the maximum number of employed cores were limited to 300. The goal of the current study was to demonstrate the scalability of the developed model on massively parallel systems, and the behavior of the model in moving from 90 cores to 300 shows the consistency in the performed performance analysis. As a result, we expect to see the same scalability behavior for problems in a larger scale with a higher number of employed computing nodes.

## 7.6 Conclusion

In this work, a mathematical model of a reaction-diffusion system with a moving front was constructed, and the corresponding computational model was implemented using the finite element method. In order to correlate the

diffusion phenomenon to the moving boundary position, high numerical accuracy is necessary at the diffusion interface, which requires a finer discretization of space near the moving front. This leads to an expensive computational model, which makes employing HPC techniques crucial in order to improve the simulation execution time. To this end, a high-performance domain decomposition approach was employed to partition the mesh and distribute the workload to available computing resources. Additionally, an efficient preconditioner/solver combination for reaction-diffusion PDEs was used to optimize the model to be used for the high-performance simulation of large scale systems in which the movement of system boundaries is controlled by reaction-diffusion phenomena.

The investigated problem was the degradation of a magnesium block inside a solution, in which the surface of the block moves due to the reaction-diffusion phenomena in the metal-medium interface. The implemented model showed a good agreement with the experimental data in terms of the degradation rate and chemical reactions, and the parallel efficiency and linear scalability were appropriate in performance evaluation tests. For the next stage of the study, it could be interesting to evaluate the model and its performance on a much larger system and tune the resources and memory usage by testing different preconditioners and solvers.

## 7.A Comparing the performance of different combinations of KSP types and preconditioners

In order to yield the highest performance, a variety of different combinations of KSP types and preconditioners were evaluated, such as Conjugate Gradients (CG), Successive Over-Relaxation (SOR), block Jacobi, and Algebraic Multi-grid (AMG), and Generalized Minimal Residual Method (GMRES). The tests were performed using 6 MPI cores on an Ubuntu machine with an Intel Core i7-8850H CPU (2.6 GHz of clock speed) and a total available memory of 32 GB.

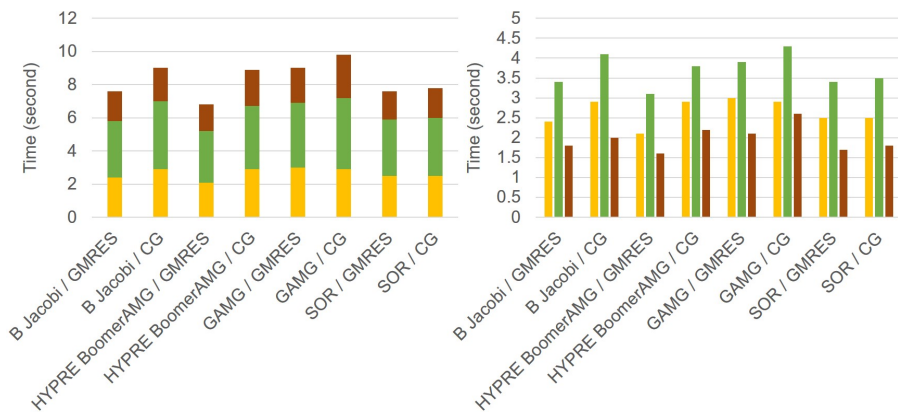


Figure 7.12: Performance test result for various combinations of preconditioners and solvers. Results are broken down into contributions for each PDE, which are plotted cumulatively and separately in the left and right plots, respectively.

Table 7.2: Performance test result for various combinations of preconditioners and solvers, presented by the execution time of each PDE.

		B Jacobi / GMRES	B Jacobi / CG	HYPRE / GMRES	HYPRE / CG	GAMG / GMRES	GAMG / CG	SOR / GMRES	SOR / CG
Solution time of each time step (s)	LS PDE	2.4	2.9	2.1	2.9	3.0	2.9	2.5	2.5
	Mg PDE	3.4	4.1	3.1	3.8	3.9	4.3	3.4	3.5
	Film PDE	1.8	2.0	1.6	2.2	2.1	2.6	1.7	1.8
Total time (s)		7.6	9.0	6.8	8.9	9.0	9.8	7.6	7.8



# Chapter 8

## BioDeg software

This chapter is based on previously published content in the *Journal of Open Source Software*:

M. Barzegari, and L. Geris, “BioDeg: A finite element software for the simulation of the corrosion and biodegradation process in metallic biomaterials,” *Journal of Open Source Software*, vol. 7, p. 4281, 2022.

### 8.1 Summary

BioDeg is an open-source software written in FreeFEM (a domain-specific language for finite element programming), C++, and Python for modeling the degradation of metallic biomaterials and simulating the biodegradation behavior of medical devices and implants in corrosion experiments. The underlying mathematical and computational models are already validated in the previous contributions [138, 139] by comparing the predictions made by the code with the experimentally obtained quantities. BioDeg supports simulating the change of morphology of the biodegradable part, release of materials, formation of surface corrosion products, the effect of the surrounding environment (such as various electrolyte solutions and chemical components as well as the presence of fluid flow), and change of other quantities (such as pH). It features command-line and graphical interfaces, being available on all major operating systems and platforms. BioDeg is

designed with open standards in mind and as a result, can be easily integrated into other established workflows such as topology optimization and tissue growth models.

## 8.2 Statement of need

Biomaterials, the substances we put inside the body to replace/repair a lost functionality, can be classified into two categories from a biodegradation perspective: bio-inert and biodegradable. While the former type has a few interactions with its surrounding environment, the latter gradually disappears and gets absorbed by the body [7, 44]. Although bio-inert biomaterials show a great performance especially in fixation applications, they bring an important problem into play: they remain in the body forever or require additional surgery to remove them. Biodegradable materials do not have this problem, and in the case of metallic biomaterials, they also provide a suitable mechanical stability profile. However, taking advantage of them requires tuning the degradation parameters and material release rate [10].

This problem is usually investigated by conducting *in-vitro* (in the lab) and *in-vivo* (in a living system) tests of biodegradable metallic implants, which requires conducting multiple experiments for different scenarios and situations and spending a lot of resources. Developing a quantitative mathematical model of the degradation process is a proper solution to this issue by allowing researchers to study the biodegradation behavior of any desired implant *in-silico* (in the computer) prior to conducting any *in-vitro* or *in-vivo* experiments. Developed mathematical models can be simulated using efficient numerical methods such as the finite element method.

Although there is a wide variety of relevant theoretical studies in the field of corrosion and biodegradation simulation [48, 52, 50, 55, 81, 140, 141], to the best of the authors' knowledge, none of the developed models has been publicly released together with their code to be evaluated by the scientific community. It means that none of the previous contributions are available as a software tool for relevant users such as researchers in biomaterials science, regenerative medicine (tissue engineering), and biomedical engineering.

Moreover, the available tools used to implement aforementioned models are not open-source or have the issue of restricted access. For example, COMSOL

multiphysics (COMSOL Inc., USA) has a module for mechanistic corrosion simulation, although it lacks certain research-related features like simulating the change of morphology of the corroding object and freedom in defining the chemical reactions. Another example in this regard is the MuPhyS software [81, 142] developed by the research group of Electrochemical and Surface Engineering (SURF), Vrije Universiteit Brussel, Brussels, Belgium. Despite being able to perform mechanistic biodegradation simulations, MuPhys is a closed-source software for in-house applications and is not publicly available to general users.

BioDeg is a fully open-source biodegradation and corrosion simulation software, currently validated for magnesium biomaterials [138]. A cross-platform and easy-to-use user interface makes it possible for anyone to use the program to simulate the biodegradation behavior of metallic implants with any shape of interest without concerning the technical aspects of the code. Technically speaking, BioDeg uses the finite element method to solve a set of partial differential equations derived mechanistically from the chemistry of biodegradation and utilizes high-performance computing (HPC) techniques to make the computation scalable to hundreds and thousands of computational nodes.

## 8.3 Overview of BioDeg

### 8.3.1 Basic concepts

From a general point of view, material modeling techniques are categorized as either stochastic or deterministic. In stochastic modeling, material state evolution is modeled by a set of semi-random rules, implying the conditions in which materials interact with their surrounding environment. On the other hand, deterministic modeling takes advantage of conservative laws in physics, formulating the interactions of materials by means of the rules such as the ones coming from transport phenomena [143].

BioDeg works based on the principles of deterministic modeling for predicting the biodegradation and corrosion of metallic materials. Several studies have demonstrated that this type of modeling has a high potential in representing the biodegradation and corrosion phenomena [81, 55, 141]. BioDeg is built upon a mechanistic formulation of the biodegradation process [138]. The developed model captures the release of metallic ions, changes in pH, the

formation of a protective film, the dissolution of this film in presence of different ions, and the effect of fluid flow of the surrounding solution. This has been accomplished by deriving a system of time-dependent reaction-diffusion-convection partial differential equations (PDEs) from the underlying oxidation-reduction reactions. The level set formalism [61] was employed to track the biodegradation interface between the biomaterial and its surroundings, enabling the model to monitor the morphological changes of the investigated implant/device during the biodegradation process. As an example of BioDeg output, figure 8.1 demonstrates the simulation results of the biodegradation of an orthopedics screw, in which the white body and the color contour show the degrading shape of the screw and concentration of metallic ions as they are released over time, respectively. The current model is able to simulate diffusion-based corrosion only, and localized corrosion is not supported yet, but further development is being done to make the model capable of simulating non-uniform corrosion as well.

### 8.3.2 Implementation

Implementing a parallel 3D computational model of the developed mathematical framework allows studying the corrosion and biodegradation behavior of medical implants and devices *in-silico* no matter the complexity of the implant shape. This has been achieved by solving the derived system of equations using the finite element method on any arbitrary 3D mesh.

The computational model (BioDeg-core) is implemented in FreeFEM [67], a domain-specific language for PDE solving and finite element computations. While having a syntax almost identical to C++, FreeFEM provides rich interfaces to well-known scientific computing libraries for performing relevant tasks such as mesh generation, solving linear system of equations, various IO operations, and HPC. This fact makes FreeFEM a perfect choice for the implementation of complex mathematical models, especially for resource-demanding applications. Additionally, a general preprocessor for embedding desired 3D shapes inside a container (the medium/electrolyte in biodegradation simulations) is implemented in FreeFEM using the ParMmg parallel mesh manipulation library [144]. This helps non-technical users to perform simulations on their desired geometries. The preprocessor performs mesh refinement on the interface of the implant and the medium to increase the numerical accuracy of interface tracking. This mesh refinement is based on

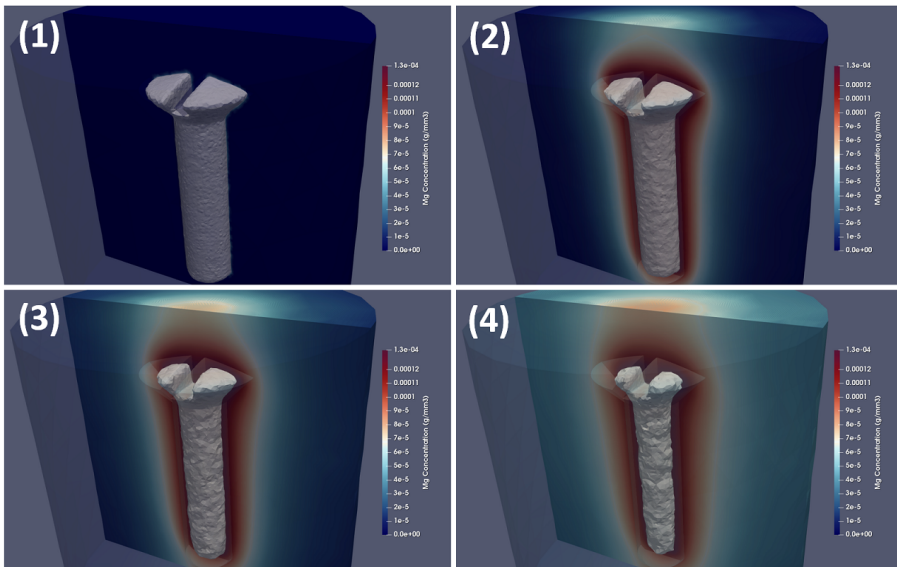


Figure 8.1: Simulation results of the degradation process of a screw made of magnesium inside a saline ( $\text{NaCl}$ ) solution, leading to a high rate of degradation. The contours display the concentration of magnesium ions on a cross-section view of the medium beside the moving surface of the screw. The screw was selected to be small (1 millimeter) so that the effect of degradation can be observed in a smaller time window. Each sub-figure shows a time difference of 24 hours. This example is provided along with the code.

the level-set function used to measure the distance of each element of the mesh to the biodegradable part surface. The preprocessor uses this function and a set of user-defined values (like the minimum and maximum element size) to refine the elements on the moving corrosion front. BioDeg supports tetrahedral elements only, which is a limitation rooted in supported element types in FreeFEM.

The user interface (BioDeg-UI) is implemented using C++ and Qt toolkit. A front-end using Qt and a back-end in FreeFEM enable BioDeg to be cross-platform and be able to run on major operating systems including Linux, Windows, and macOS. The postprocessing of the results is carried out by the open-source software ParaView [119], which is also a cross-platform postprocessor.

### 8.3.3 High-performance computing

Biodegradation simulations in BioDeg can become complex and resource-demanding. The reason lies within the refined mesh on the metal-electrolyte interface. This refined mesh is required to increase the accuracy of employed numerical schemes to track the moving corrosion front [138, 139]. This leads to an expensive computational model, and as a result, employing parallel computing and HPC techniques becomes crucial to make it possible to scale the simulations to hundreds or thousands of computational nodes and decrease the simulation execution time. To this end, a high-performance domain decomposition approach was employed to partition the mesh and distribute the workload to available computing resources [124]. Additionally, efficient preconditioners and solvers were used to solve the linear system of equations resulting from the finite element discretization. This was achieved by using the rich PETSc library [70], which provides a collection of efficient preconditioners and solvers for solving PDEs.

### 8.3.4 Installation

The main prerequisites of BioDeg are FreeFEM, PETSc, Mmg, and an MPI runtime (such as OpenMPI or MPICH). The PETSc library contains the rest of the dependencies. Since FreeFEM provides appropriate interfaces to Mmg and PETSc and includes installation scripts for building and installing them, all the requirements can be met by building/installing FreeFEM with the PETSc link enabled. While a set of pre-built binaries are available for download on the FreeFEM website, the user manual of BioDeg includes a section for instructing the users to build FreeFEM to achieve maximum flexibility on their systems.

The next step is to build or install the BioDeg UI, the graphical user interface of BioDeg. Stable binaries can be downloaded from the Release section of the GitHub repository for Windows and Linux, but if the user prefers to compile it from source code, the build process is straightforward as well. The prerequisites for building the UI are Qt framework and CMake, which need to be installed for the target operating system. The rest of the process is a standard CMake build routine, which can be followed from the installation instruction in the BioDeg User Manual or the GitHub repository. After building/installing BioDeg UI, the user can run it to setup and execute simulations.

In case the user does not need to work with the UI, like in HPC environments or for advanced users, the previous steps for building BioDeg-UI can be skipped, and the user can directly run the core model by executing `mpiexec -n N FreeFem++-mpi core/src/main.edp -v 0` to parallelize the computation into N MPI processes. In this way, the simulation can be configured by dozens of available command-line arguments, documented in the BioDeg User Manual.

For graphical output, the postprocessing of the simulation results is handled by ParaView, so the users should have it installed on the system. Stable binaries for various platforms can be found on the ParaView website, including portable versions which do not require installation and are ready to run immediately after download. BioDeg UI can help visualize the results by executing specific filtering processes in ParaView, which can also be done manually by following the postprocessing guideline provided in the BioDeg User Manual.

### 8.3.5 Documentation

A comprehensive user manual is provided for user-oriented documentation on installing the software, preparing the simulations, running the models, and postprocessing the results. As this is being developed in a separate repository (BioDeg-doc [145]), additional documents and supporting materials will be added eventually.

Since FreeFEM does not support developer-focused technical documentation (like Doxygen), the core code is fully commented for easier contribution. Further technical details regarding the development, like the theoretical foundations of the computational models, has been added to the BioDeg-doc repository [145]. Both the user manual and the theory guide are accessible from the Help menu on the BioDeg UI.

### 8.3.6 Contribution

BioDeg is developed using a wide range of open-source tools and is released under GPLv3, so unconstrained use and reuse are encouraged and welcome. The code has been initially developed as part of a PhD research project, but further contributions, either on the development of the core models or providing more supporting materials, are highly welcome. More guidelines for such contributions can be found in the CONTRIBUTING.md file in the

GitHub repository. Previous contributions are acknowledged in the BioDeg User Manual.

### 8.3.7 Published works

The code has been already used in publishing 2 scientific works so far, and there are several studies ongoing to be prepared for publication. In the published works, BioDeg was employed to simulate the behavior of high-pure magnesium (HP Mg) in immersion corrosion tests [138] as well as to evaluate the efficiency and scalability of the employed parallelization schemes for reaction-diffusion systems with moving boundaries [139]. Currently, the code is being used for simulating the degradation of magnesium in hydrodynamics (perfusion) conditions, in which the underlying phenomena are investigated in the presence of fluid flow. Moreover, BioDeg is being coupled with a topology optimization code for optimizing the shape of biodegradable structures for medical applications. Later, it will be integrated it with an optimization code and bone tissue growth models for improving the design process of biodegradable orthopedics implants.

## 8.4 Acknowledgements

The research in which the code is developed is financially supported by the Prosperos project, funded by the Interreg VA Flanders The Netherlands program, CCI grant no. 2014TC16RFCB046 and by the Fund for Scientific Research Flanders (FWO), grant G085018N. We also acknowledge support from the European Research Council under the European Union's Horizon 2020 research and innovation programme, ERC CoG 772418.

# Chapter 9

## Bayesian parameter estimation of the computational models

This chapter is based on previously published content in the *Journal of Open Source Education*:

M. Barzegari, and L. Geris, "An open source crash course on parameter estimation of computational models using a Bayesian optimization approach," *Journal of Open Source Education*, vol. 4, p. 89, 2021.

This publication included didactical and educational materials in Jupyter Notebooks format to make it possible for readers to follow the principles interactively. The introductory part of the Jupyter Notebook file is included in this chapter as well.

### 9.1 Summary

Parameter estimation is a crucial aspect of computational modeling projects, especially the ones that deal with ordinary differential equations (ODE) or partial differential equation (PDE) models. Well-known examples in this regard are models derived from a basic balance or conservation law, such

as mass balance or heat transfer problems. For real-world applications, these equations contain some coefficients that cannot be obtained directly from published scientific materials or experimental studies [146]. One of the best solutions to this challenge is constructing an inverse problem.

According to [147], inverse modeling is the use of the results of some measurements of observable parameters to infer the values of the model parameters. Put differently, what we want to do is estimate parameters that cannot be directly measured for our computational model. This is also called parameter estimation or model calibration [148]. Indeed, we calibrate our model to act similarly to available experimental data, and then this calibrated model can be used to simulate other scenarios that haven't been tested yet in the experiments. This is a common process in a lot of modeling problems in science and engineering.

Take a simple reaction-diffusion equation as an example, in which the change of the concentration of a sample chemical component  $C$  is studied over time. By assuming that the correlated chemical reaction is  $A + 2B \rightleftharpoons C$ , occurring in a diffusible medium (such as a chemical solution), the PDE to describe the mass transfer phenomenon over time can be written as [59]:

$$\frac{\partial[C]}{\partial t} = \nabla \cdot (D_C \nabla [C]) + k_1[A][B]^2 - k_2[C] \quad (9.1)$$

in which  $[X]$  denotes the concentration of the chemical component  $X$ , the  $D_C$  is the diffusion coefficient of  $C$  in the medium, and  $k_1$  and  $k_2$  are the rates of the forward and backward reactions, respectively. To solve this PDE numerically and get quantitative data (the goal of most of the scientific computing projects), we need to know the value of  $D_C$ ,  $k_1$ , and  $k_2$ , which is usually hard-to-find in the literature.

As mentioned above, one solution is to solve the inverse problem, in which we can use optimization techniques to minimize the difference between the model output and experimental data. Bayesian optimization is one of the most efficient approaches in this regard [74]. HyperOpt [149] is a Python package that provides easy-to-use interfaces to implement a Bayesian optimization problem, making it a good choice for both educational and practical purposes. In our educational module, we used this package to teach the principles of an efficient parameter estimation pipeline.

For demonstration purposes, an interpolation problem is solved by using the

parameter estimation techniques that a computational modeling researcher employs for model calibration. Indeed, the computationally intensive code is replaced with a simple function evaluator, which helps students to learn the core concepts without waiting too much for the process to finish. Students will be guided through several steps of refining the results inside the notebook, where the interactive computing environment of Jupyter facilitates exploring the implementation more efficiently in comparison to traditional educational materials.

## 9.2 Statement of Need

Despite its simplicity, building an inverse problem is hard for many students. The problem is that, although it is relatively simple to describe the process visually, implementing it for a practical application becomes challenging in its early stages. In this educational module, a simple optimization problem is implemented in a Jupyter notebook to teach students how to construct an inverse problem and tune it to get better results in such a problem. In this way, students can work on a real-world optimization problem in an interactive environment and learn the concepts behind taking advantage of a modern optimization method (Bayesian approach) for parameter estimation of a computational model.

Our notebook is a modern learning module for relatively old and frequently-used concepts (global optimization, Bayesian techniques, inverse problems). It has been designed to be useful for both teachers and students. Students can use it as a self-study guide for parameter estimation and inverse problem construction, while teachers can change the underlying problem to any other desired one easily and make the learning module compatible with their own teaching requirements.

## 9.3 Learning objectives

Upon completion, students will be able to:

- Understand the concept and necessity of parameter estimation in science and engineering

- Describe what the whole process of Bayesian optimization is all about
- Define and implement a Bayesian optimization workflow for parameter estimation of common use-cases
- Critically evaluate the output of the process and fine-tune the setup of the Bayesian optimization
- Apply the obtained knowledge to any kind of models that are commonly used in science and engineering

## 9.4 Prerequisites

In order to go through the learning module, the students should have a working knowledge of programming in Python. Additionally, a basic understanding of mathematics is required to get the concept of models in science and engineering. The given example is a mathematical model derived from differential equations, so knowledge of differential equations can help to understand the importance of parameter estimation in these widely-used models. However, in case of necessity, the example can be replaced by any other relevant one for the target learners.

## 9.5 Pedagogy and instructional design

The provided material is in the format of a crash course, which is suitable for being taught in one session of undergraduate or graduate courses for science and engineering students. Courses to which this material is relevant can be “optimization”, “scientific computing”, or “parametric design”. The material may also be useful for relevant educational projects for the target students, in which they can employ the learned techniques to construct efficient inverse problems for parameter estimation.

The teaching strategy is based on the worked-example effect [150], in which an example of parameter estimation is fully implemented to allow students to play with and modify the code to have their own reflection in class discussions. Basic prior knowledge of Python suffices as the problem doesn't involve students with complicated programming stuff. The student-centric

characteristic of this crash course helps teachers to adopt the material easily and integrate it into an existing syllabus of relevant courses in science and engineering.

## 9.6 Getting started

The learning material is provided as a single Jupyter notebook, in which all the steps of constructing an inverse problem are described in detail with accompanying Python codes. A very simple simulation code (in the context of an interpolation problem) is also provided and can be found in the repository. The code inside the notebook calls this external program at certain points to mimic the interaction of the parameter estimation routine and the main computational code that contains the unknown parameters.

To get started with the module, the user should set up the environment first. The setup instructions are provided in the `README.md` file of the repository. After setting up the Jupyter notebook and installing the required packages, the user can navigate to the `src` folder and run the notebook file. No further action is needed as the content of the notebook is self-explanatory and easy-to-follow.

## 9.7 Acknowledgements

This research is financially supported by the Prosperos project, funded by the Interreg VA Flanders The Netherlands program, CCI grant no. 2014TC16RFCB046 and by the Fund for Scientific Research Flanders (FWO), grant G085018N. We acknowledge support from the European Research Council under the European Union's Horizon 2020 research and innovation programmes, ERC CoG 772418.

## 9.A A glimpse of the Jupyter notebook

### 9.A.1 Introduction

As the name implies, the parameter estimation process deals with approximating unknown parameters, the factors that define a system or its operation. In science and engineering, this can be seen as a sub-category of optimization techniques since we seek to find the optimal state of a system. After finding the desired state, we look for the parameters contributing to such a state. It is indeed what parameter estimation is all about. Seems complex? Look at it as a calibration process, in which a machine, tool, or system is tuned to produce a correct output. Imagine you want to calibrate a machine with 3 knobs. How do you do the calibration? You compare the output with a reference, something you know the machine should produce, and then try to adjust the knobs such that the output matches the reference. It is how calibration works, no? Take a thermometer as an example. You have a reference temperature, like boiling water at 100 degrees Celsius, and 3 knobs on the device. You continue turning the knobs to see 100 appearing on the machine, and by doing that, you calibrate the thermometer. In this way, you have estimated the unknown parameters (the 3 knobs) of the device. After being calibrated, you can use the thermometer to measure any temperature.

Now, instead of the machine, assume you want to perform the same process on an engineering system. Each system (or, let's say, model) has a certain number of parameters to be tuned. After calibrating the system (model) with the reference data (a data we already know is correct), we can assure that the system's output is more or less valid if being used for another measurement (prediction). Real-world systems in science and engineering contain some parameters that cannot be obtained directly from published scientific materials or experimental studies. Thus, we should estimate them using a calibration (optimization) strategy, a process that is generally called an inverse problem.

An inverse problem in science is usually referred to the process of calculating the causal factors from a set of observations that have produced them. Inverse problems are important because they tell us about parameters that we cannot directly observe. That's exactly what we want to do: estimating parameters that we cannot directly measure for our model. Indeed, we calibrate our model to act similarly to available experimental data, and then this calibrated model can be used to simulate other scenarios that we have not tested in experiments. This

concept is similar to the training process of machine learning models. You train the model by making it fit to previously available data and asking it to predict unseen data.

To construct an inverse problem for computational models, we can take advantage of conventional optimization approaches. The goal is to minimize or maximize a function, or more technically speaking, an objective function. Mathematical optimization is selecting the best element (concerning some criterion) from some set of available alternatives. In the simplest case, an optimization problem consists of maximizing or minimizing an objective function by systematically choosing input values from an allowed set and computing the output of the system. More generally, optimization is the process of finding the optimum value of an objective function given a defined domain (or input). To wrap up, the essential concepts here are the objective function (what we want to minimize) and the domain space (values of the parameters over which we minimize the objective).

Back to our example problem, our objective function will be the difference between the produced output of our simulation and the experimental data of the exact condition, which is also called "loss". In other words, we change the coefficients such that the simulation output would be the same as (or close to) the experimental data that we already have. To this end, we can choose random values out of the domain space (the range that we search for appropriate values), evaluate the model with those values, and continue this process till we find the lowest loss possible. This can be a good approach as long as the cost function evaluation is cheap, which means the simulations run fast (because we need to run the simulation to evaluate the cost function). The problem is, for most of the real-world models, running each simulation takes quite long. As a result, each iteration of the optimization algorithm is not cheap anymore. To overcome this issue, we use a Bayesian optimization strategy, a method that is usually employed to optimize expensive-to-evaluate functions.

## 9.A.2 Bayesian optimization

To describe how the Bayesian optimization approach helps us to overcome the problem mentioned above, I use the great description made by @WillKoehrsen. I can't explain it better (you can find the full interactive document at <https://github.com/WillKoehrsen/hyperparameter-optimization>:

*Evaluating the objective function is the expensive part of optimization, so ideally, we want to limit calls to this function. One way we can limit calls is by choosing the next values to try in the objective function based on the past results. Bayesian optimization differs from random or grid search by doing exactly this: rather than just selecting from a grid uninformed by past objective function evaluations, Bayesian methods take into account the previous results to try more promising values. They work by constructing a probability model of the objective function (called a surrogate function)  $p(\text{score}|\text{parameters})$  which is much easier to optimize than the actual objective function.  $p(A | B)$ , the conditional probability, is the probability of A given B, i.e., A after B is observed.*

*After each evaluation of the objective function, the algorithm updates the probability model (usually given as  $p(y|x)$ ) incorporating the new results. Sequential Model-Based Optimization (SMBO) methods are a formalization of Bayesian optimization that updates the probability model sequentially: every evaluation of the objective function with a set of values updates the model with the idea that eventually the model will come to represent the true objective function. This is an application of Bayesian Reasoning. The algorithm forms an initial idea of the objective function and updates it with each new piece of evidence.*

*The next values to try in the objective function are selected by the algorithm optimizing the probability model (surrogate function), usually with a criterion known as Expected Improvement. Finding the values that will yield the greatest expected improvement in the surrogate function is much cheaper than evaluating the objective function itself. By choosing the next values based on a model rather than randomly, we hope that the algorithm would converge to the true best values much quicker. The overall goal is to evaluate the objective function fewer times by spending a little more time choosing the next values. Overall, Bayesian Optimization and SMBO methods:*

- Converge to a lower score of the objective function than random search
- Require far less time to find the optimum of the objective function

*So, we get both a faster optimization and a better result. These are both two desirable outcomes, especially when we are working with heavy computational models!*

According to this simplified description, Bayesian optimization is a great candidate to perform the parameter estimation of PDE-based computational models. If you are interested to know more about the mathematical aspects of the Bayesian optimization, you may have a look at the SigOpt Bayesian Optimization Primer.

In this notebook, we implement the whole process of a Bayesian optimization strategy, including constructing a cost function by calling the simulation code, performing the optimization, and postprocessing the results. To do this, we use Python and HyperOpt, an open-source Python library for Bayesian optimization that implements SMBO using the Tree-structured Parzen Estimator (TPE). TPE, along with Gaussian Processes and Random Forest Regression, are the algorithms that can be used in the SMBO method to construct the probability model (surrogate function). We don't need to worry about implementing the algorithm because Hyperopt takes care of that for us. We have to make sure we have correctly defined the objective function and the domain of values to search over.

### 9.A.3 Sample problem

Instead of a PDE model, we use a more straightforward problem to focus more on the optimization rather than the numerical simulation of the PDE. The problem with which the optimization algorithm interact is fitting a 4th-order polynomial equation on some experimental data. You should notice that the optimization algorithm is entirely unaware of the fitting problem behind the objective function.

The objective function is implemented in a general way: calling the external simulation code, gathering produced output, and computing the loss. To make this as real-world as possible, I implemented an external Python code that takes polynomial coefficients and computes the function values on desired points. This data is saved on the disk and then retrieved by the objective function of the main optimization code to calculate the loss. In a real-world application, the external simulation code takes the coefficients (such as the reaction rates in the above PDE example), performs the simulation, and writes the output to the disk. The rest of the process is the same. In the next step, the optimization algorithm changes the parameters and calls the external simulation code again to see the loss of the new parameters. This process continues iteratively to a certain number of iterations.

The experimental data, which are indeed 21 points of a 4th-order polynomial function in the range  $[0, 5]$ , are stored in a CSV file. Each line contains one point, better to say a pair of two values defining a point, and this exactly what it can be in a real scenario. For example, it can contain the value of a chemical

component concentration over time, in which the first and second values of each line would be time and concentration, respectively.

The optimization output of this sample problem will be similar to Fig. 9.1.

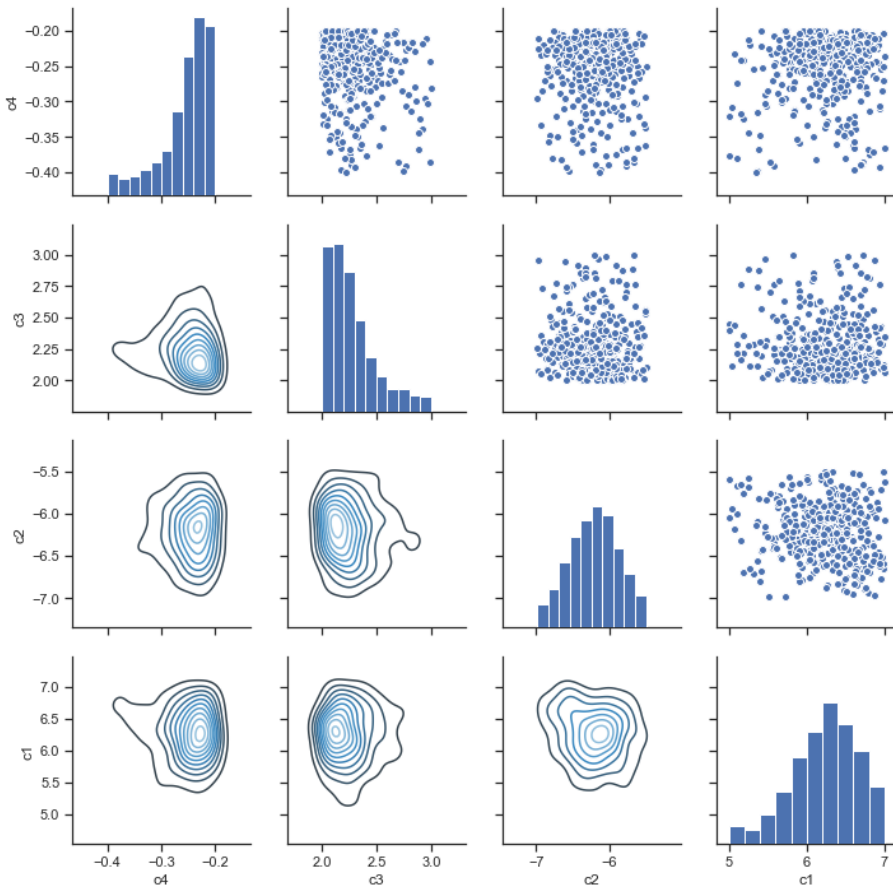


Figure 9.1: A typical output of the parameter estimation process, plotted using the Seaborn Python package, which shows how the optimization algorithm has chosen the values of different parameters in different iterations by comparing the distribution of points 2 by 2 for 4 unknown parameters of the polynomial model.

## **Part IV**

# **Model Applications**

# Chapter 10

## Applications: Mandible plate

This chapter is based on submitted content to the *Journal of the Mechanical Behavior of Biomedical Materials*:

P. Ansoms, M. Barzegari, and L. Geris, "Coupling biomechanical models of implants with biodegradation models: a case study for biodegradable mandibular bone fixation plates," submitted to *Journal of the Mechanical Behavior of Biomedical Materials*, 2022.

### 10.1 Introduction

In bone tissue engineering, biodegradable implants have gained in popularity over recent years. The main advantage of biodegradable implants over non-biodegradable implants is that no second surgery is needed to remove the implant after successful healing of the bone [7]. The removal of a non-biodegradable implant might be necessary to avoid complications in the long term and brings along an additional cost and risk of infection. Two other side effects of permanent implants are late thrombosis and chronic inflammation [1]. Late thrombosis is the formation of blood clots due to the presence of the metallic implant [151]. Chronic inflammation is induced by the persistence of inflammatory stimuli, being the physical presence of the implanted biomaterial or the ability of the implant to slightly move at the implant site [152]. Permanent metallic implants also distort diagnostic images

of the body [153]. Both in the short and long term, a biodegradable implant reduces stress shielding, which is the reduction in bone density as a result of removal of stress on the bone. The reduction of stress shielding in the long term is obvious since the the implant has disappeared in case of a biodegradable implant. The reduction of stress shielding in the short term results from the fact that biodegradable metals often have a Young's modulus that is much lower than that of inert metals (e.g. 44 GPa for WE43 vs. 118 GPa for Ti6Al4V). The stress shielding effect is directly proportional to the E-modulus of the implant material.

The use of biodegradable metals to support tissue regeneration is mentioned in various sources, describing different applications [1, 154, 155]. The material of the implant determines the rate of degradation. The goal is to provide stable mechanical support at the early stage of the tissue healing process and then have the material gradually degrade with the restoration of the defect tissue [155]. Fig. 10.1 qualitatively shows the degradation rate of three common biomaterials (magnesium, zinc, and iron) along with the healing rate of different tissues (hard, soft and vascular) as an illustration. By matching a material's degradation rate and a tissue's healing rate, a suiting material can be found for a certain application.

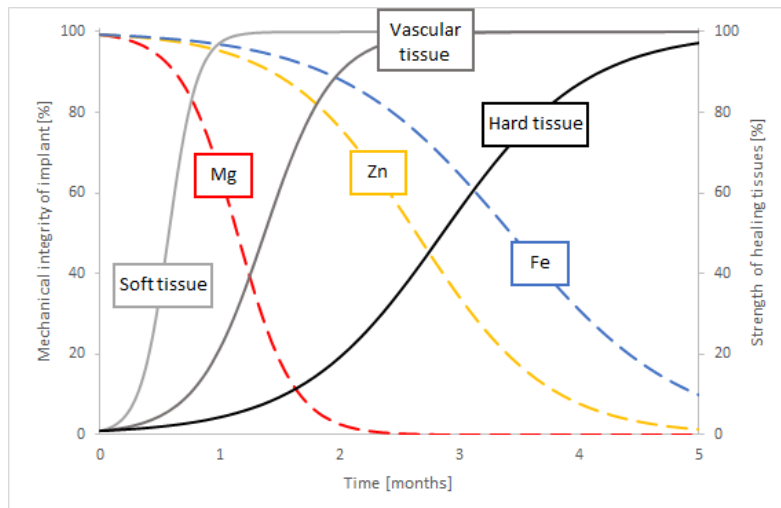


Figure 10.1: The change in mechanical integrity of the implant and tissue strength over time (Adapted from Chen et al. [1])

Studying the change of mechanical support of implants due to biodegradation has certain complexities. This case-study aimed to gain insight into the change in mechanical behavior of a biodegradable mandibular fixation plate. In order to do this, three different models should be combined: a biodegradation model to characterize the geometry change as a result of biodegradation, a model to characterize the loading on the jaw plate by considering the bone healing, and a model to predict the mechanical behavior of the plate.

The mandible is the second most frequently fractured bone of the face and the tenth most frequently fractured bone of the body [156]. Common causes for a mandible fracture are violence, car crashes and sports. It occurs more frequently for males than for females and most often between the ages of 16 and 30. The weakest section of the mandible is the angle because there is an abrupt change in direction between the body and ascending ramus, both in the sagittal and transverse planes, resulting in the involvement of the mandibular angle in jaw fractures in up to 28.5% of cases [157]. The treatment of mandible fractures is most commonly done with a mandibular fixation plate (further referred to as jaw plate) to stabilize the fracture and allow the healing process to take place. The plate is traditionally made of an inert implant material (e.g. titanium), which implies that it has minimal interaction with the surrounding tissues. Alternatively, the implant can be made from biodegradable materials to take advantage of the aforementioned benefits.

The outcome of different surgeries on the mandible has been modelled by several studies [158]. Zheng et al. were able to evaluate the impact of mandibular reconstruction surgery on the muscular functionality by developing a static FE model [159]. A topology optimization was performed by Wu et al. for a similar application, with the inclusion of a bone remodeling algorithm [160]. Boccaccio et al. studied distraction osteogenesis of the mandible with a focus on tissue differentiation [161]. These models incorporated the tissue regeneration, but did not incorporate a biodegradable fixation system. The combination of concurrent biodegradation and bone regeneration has been developed for long bones by Mehboob et al. [162] and by Ma et al. [163]. Vautrin et al. even developed a combined biodegradation and tissue regeneration model in the context of orthognathic surgery [158]. The bone healing algorithm was based on the model that Alierta et al. developed, but was generalized to be applicable to a larger fracture gap [164]. It modeled the growth of the contribution of cartilage and bone to the mechanical properties of each element within the fracture gap based on the principal element strains under

physiological loading. The biodegradation algorithm was limited to being phenomenological to reduce the computational cost. It included only localized corrosion by incorporating a random pitting corrosion algorithm.

The present work incorporated a more detailed biodegradation algorithm based on the chemistry of biodegradation of WE43. The tissue regeneration algorithm, on the other hand, made use of beam theory which was made possible by the specific type of fixation that was considered. The case-study focuses on investigating the effect of the number of plate holes left unscrewed and the impact of biodegradation on mechanical support in this condition.

## 10.2 Materials and methods

### 10.2.1 Case study

The implant for this case study was a jaw plate based on the one shown in Fig. 10.2. This technique of mandibular fracture fixation is called the 'miniplate fixation technique', also known as 'semi-rigid' or 'functionally adequate fixation'. The loading on the plate in this situation is purely tensile when a mastication load is applied. This is shown in Fig. 10.3. Fig. 10.4 shows the plate that was used for this case study, and Fig. 10.5 shows the use of different amounts of screws for fixation. This was implemented to investigate the effect of leaving holes open and exposed to body fluids. Leaving holes open is a common thing because in some cases the location of a screw may be too close to a fracture line or in a section of the bone that is simply too weak. The details about the geometry are given in section 10.2.3. Leaving a hole open is reflected both in the boundary conditions and in the degradation behavior of the simulation since it is assumed that a screw closes a hole off from body fluids and hence prohibits degradation within the screw hole.

### 10.2.2 Biodegradation behavior simulation

In the current study, the degradation was considered in simulated body fluids (SBF) solutions, which are the most similar buffered solutions to the body environment and are designed to mimic the surrounding environment of implants and medical devices *in vitro*. The biodegradation process was

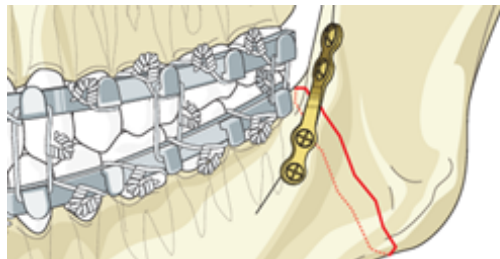


Figure 10.2: Miniplate fixation by AO Surgery Foundation [2]

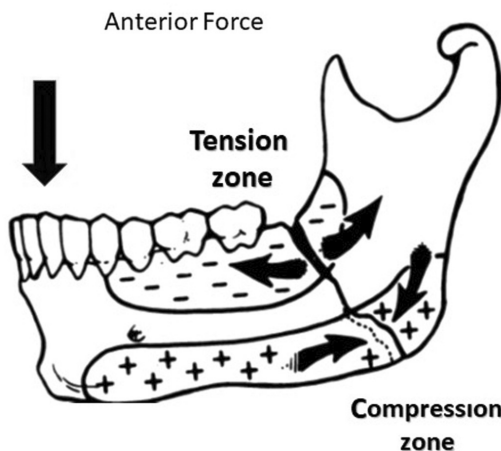


Figure 10.3: Occurrence of compressive- and tensile stresses around the fracture site when biting [3]

modeled as a set of partial differential equations (PDEs), formulating the mass transfer phenomena as well as tracking the location of the surface of the implant during degradation. For the mass transfer model, a system of time-dependent reaction-diffusion PDEs was derived from the underlying oxidation-reduction reactions in SBF solutions. This includes the oxidation of the metallic part, reduction of water and oxygen, changes in pH, the effect of different ions in the medium, and formation of a protective film on the surface of the scaffold, slowing down the rate of degradation. Additionally, investigating the structural changes of implants requires monitoring the morphological changes, which was achieved by tracking the movement of the corrosion front. This was done by constructing an equation based on the Level Set formalism, capturing the movement of the environment-implant

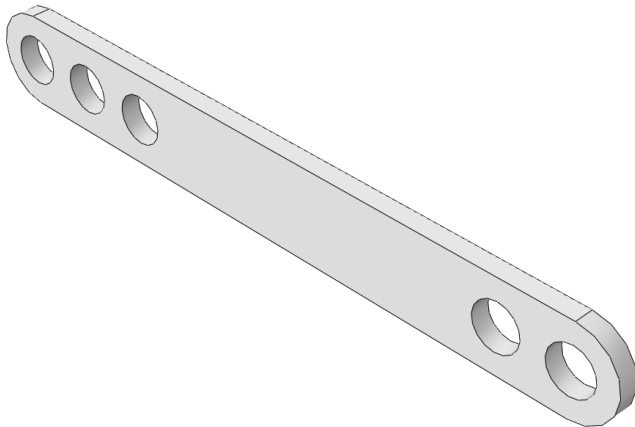


Figure 10.4: Model for the jaw plate

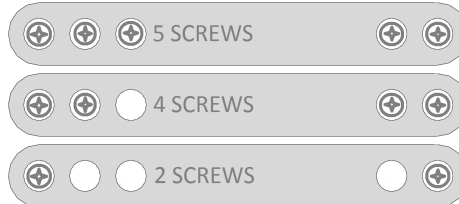


Figure 10.5: Five, four or two screws

interface by defining an implicit surface. So, the zero-iso contour of this implicit Level set function determines the surface of the implant. The derived equations were coupled and solved implicitly using the finite element method, implemented in FreeFEM [67]. Experimental data to validate the developed biodegradation model were collected from immersion tests of simple blocks. More details of the model implementation and validation can be found in our previous work [138]. Moreover, the mesh was refined adaptively on the corrosion front to increase the numerical accuracy of the interface tracking equation, leading to a computational-intensive model. So, in order to increase performance and reduce the simulation time, the code was parallelized in a way that the computation could be distributed across several computing nodes. This was mainly achieved using domain decomposition techniques and high-performance solvers. More information about this efficient implementation as well as a performance analysis of the model is presented in our previous work [139].

For the biodegradation simulation, the jaw plate was embedded into a cubic container acting as the surrounding environment. As mentioned above, the mesh was refined on the metal bulk interface, leading to a mesh comprising of 19,924,153 elements and 3,316,135 degrees of freedom (DOF) for each PDE. The material properties, including the diffusion coefficient of various contributing ions and reaction rates were set to mimic the degradation condition in SBF. The preferred values for SBF solutions as well the process for obtaining them is described in detail in our previous contribution [138]. The biodegradation simulation was carried out using 170 computing cores.

### 10.2.3 Mechanical behavior simulations

The finite element (FE) method was used to characterize the mechanical behavior of the degrading jaw plate. The simulations reflected tensile tests with different amounts of degradation, corresponding to a different point in time during the biodegradation process. Force-displacement curves were recorded during the analysis, from which the maximum bearable force was extracted to characterize the mechanical behavior. The analyses were performed in Abaqus/CAE v6.11 (Dassault Systèmes, USA). The type of analysis was explicit/dynamic. The explicit/dynamic analysis is a technique for the integration of the equations of motion through time. It calculates the next state of the system based on the previous state and in this way calculates motion iteratively. As a result, the system is not unconditionally stable, in contrast to a standard analysis. Therefore, sufficiently small time steps are required to ensure a stable calculation. Explicit dynamic analyses are useful in problems with high-speed dynamics, but also in quasi-static problems with large non-linear deformations and in highly discontinuous post-buckling and collapse simulations [165]. So, this is an ideal type of analysis for the simulation of tensile tests, in which failure of the material occurs. The simulations were performed on a machine with a 32-core AMD EPYC 7551 processor @2.00GHz and 64GB of RAM.

The material model for the simulations was based on WE43, which is a magnesium alloy with yttrium, zirconium, and rare earth elements added. Table 10.1 lists the properties that are important for the simulations. The true stress-strain relationship in the plastic region had to be specified for the plastic deformation behavior, so a stress-strain curve of WE43 from literature was used, shown in Fig. 10.6.

Parameter	Value	Units
Density	1800	kg/m <sup>3</sup>
E-modulus	44.2E+09	Pa
Poisson's ratio	0.27	-
Fracture strain	0.04	-
Yield stress	1.6E+08	Pa

Table 10.1: Material parameters for WE43

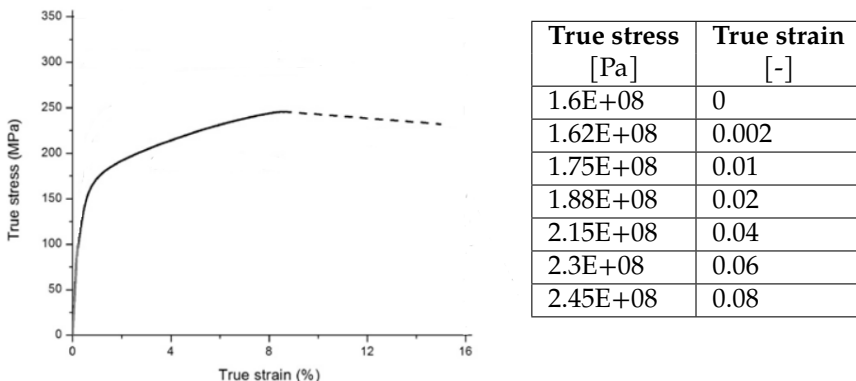


Figure 10.6: True stress-strain curve of WE43 [4]

Sensitivity analyses were performed on various parameters of the explicit/dynamic analysis as well as on the mesh density. The first parameter was the maximum degradation, corresponding to the point at which an element is removed from the analysis as its load-bearing capacities degrade due to plastic deformation. The second was mass scaling, being the artificial increases of the mass of the system in order to increase its predictability. As a result of mass scaling, the time steps (size of the increments in the loading/displacement step) can be increased without divergence of the solution (the non-linear solution path can be traced) and the computation time is decreased. Since the simulation is quasi-static, the behavior of the material can be considered as rate-independent, so the real time scale is not important. The third parameter was the number of processors for calculation (parallel computing). The last parameter was the displacement at failure, which is a material parameter that specifies the evolution of damage with relative plastic displacement after one or more of the damage initiation criteria (fracture strain, stress triaxiality, or strain rate) are met [166, 167]. The values of the investigated parameters that

were used for the analysis of the mechanical behavior of the jaw plate are listed in Table 10.3. The global mesh size was chosen to result in four elements spanning the thickness of the plate with adjusted values of the displacement at failure. Fig. 10.7 and Table 10.2 show the exact dimensions of the models of the jaw plate at five different time points during the biodegradation process. Further degradation after the 120th day is calculated by assuming a linear degradation rate. Other details of the FEA can be found in Table 10.3.

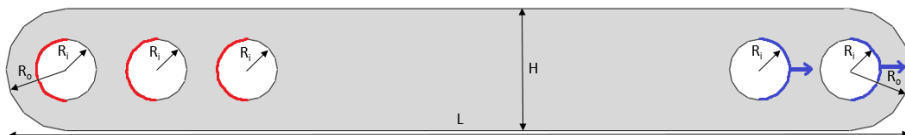


Figure 10.7: Top view of the jaw plate with five screws with dimensions and boundary conditions

Time after implantation [days]	0	28	77	124	170
Depth [mm]	1	0.95	0.9	0.85	0.8
H [mm]	4	3.95	3.9	3.85	3.8
R <sub>i</sub> (screw) [mm]	1	1	1	1	1
R <sub>i</sub> (no screw) [mm]	1	1.025	1.05	1.075	1.1
Mass loss [%]	0	6.63	13.0	19.2	25.2
Mesh size [mm]	0.25	0.2375	0.225	0.2125	0.2
DAF [ $\mu\text{m}$ ]	10	9.63	9.25	8.87	8.48

Table 10.2: Dimensions and mesh size of the different models for the jaw plate with five screws, along with the DAF value

Element type	Tetrahedral
Geometric order	Linear (4-node elements)
Mass scaling factor	1000
Distortion control	Enabled
Distortion control: length ratio	0.1
Element deletion	Enabled
Max degradation	0.95
Processor parallelization	4 processors in parallel

Table 10.3: Details about the FE analysis

### 10.2.4 Bone healing and implant load models

According to Reina et al., the body of the mandible behaves like a long bone [168]. Also, Korioth et al. mentioned that the jaw behaves as a beam, with the corpus (body) behaving as a hollow beam [169]. The 'normal' loading of the mandible occurs when eating. More specifically, the force exerted between the incisors was taken in this case study such that location of the force leads to a large moment due to the large lever arm for the moment generated in the vicinity of the fracture. Fig. 10.8 shows the fractured mandible with an approximate positioning of the jaw plate. The load was assumed to be vertical [168]. The maximal biting force, recorded at the central incisors was taken as 209 N on average [170]. With the fracture being just posterior to the third molar, the lever arm is the distance between the central incisors and the back of the third molar, projected onto the sagittal plane. The value of 50 mm was used for this analysis, based on average values found in literature [171].

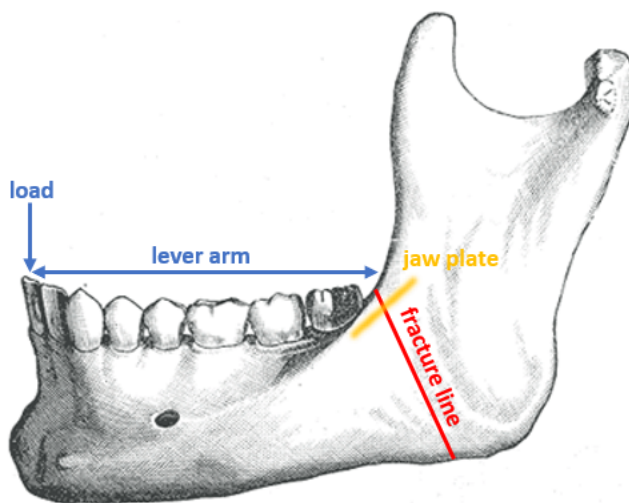


Figure 10.8: Mandible with indication of fracture line, jaw plate, lever arm and load [5]

Fig. 10.9 shows the cross-section of the mandibular body on the left, consisting of an outer layer of cortical bone and an inner core of trabecular bone. An approximation of this cross-section using only rectangular shapes is also presented in Fig. 10.9. This simplification was made for easier calculation of the area moment of inertia of the cross-section. The relevant dimensions for

the calculation were the height and width of the outer (cortical) layer of bone as well as the thickness of this layer. These dimensions were selected based on average values for males, as they are more common to have mandible fractures [156]. The average height of the mandibular body is 22.4 mm for males, as reported by Sittitavornwong et al. [172]. But, since the fracture line was not perpendicular to the longitudinal axis of the mandibular body, the height of the cross-section was larger than the height of the mandibular body. There was no information available on an exact fracture line, but it was estimated to be rotated 25° from the vertical. That brought the height of the mandibular body to 24.7 mm. The average width of the mandibular body is 15.9 mm, according to a study by More et al. [173]. Katranji et al. found the cortical bone thickness in the mandible to be 2.06 mm on average and was assumed to be equal all around the perimeter of the cross-section [174]. While the jaw plate is placed a little more on the side of the mandibular body in Fig. 10.8, it was placed on top of the mandibular body in the approximation in Fig. 10.9. This was done to keep the neutral axis horizontal and to limit the complexity of the approximation. Fig. 10.10 shows a close-up of the cross-section of the jaw plate with the relevant dimensions. The cross-section of the jaw plate consisted of two separate rectangles because the break in the jaw plate occurs close to a hole, which was the weakest region of the jaw plate.

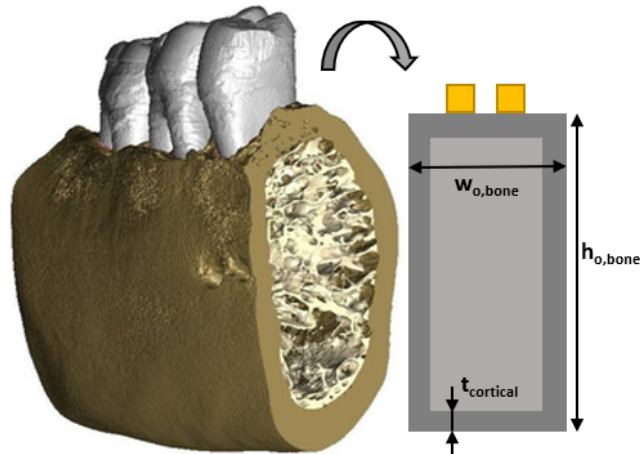


Figure 10.9: cross-section of the mandibular body on the left and approximation of this cross-section with dimensions on the right [6]

The E-modulus of the jaw plate was 44.2 GPa. The E-moduli of the cortical

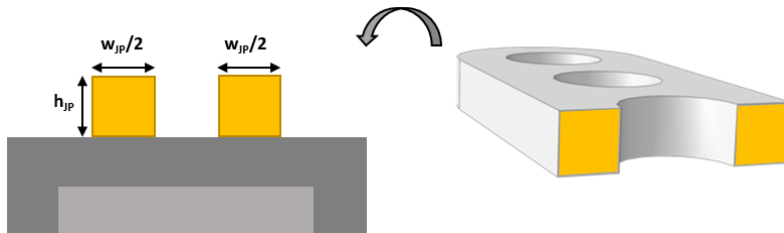


Figure 10.10: Close view of the cross-section of the jaw plate (indicated with JP in the figure) around the third hole (arbitrary, break does not always occur around this hole) with dimensions

and trabecular bone changed over time to capture the bone healing process. To know which value of the E-modulus must be used for the cortical bone, an assumption had to be made regarding the bone healing process [175]. Two scenarios are possible for cortical bone healing: one with direct contact between the broken bone ends and one without [176]. If the broken ends are pressed against each other and are rigidly fixed in place, this is called direct bone healing. The gap between the bone ends must be smaller than 0.001 mm and the interfragmentary strain must be less than 2% for direct bone healing to occur. Cutting cones, consisting of osteoclasts, cross the fracture line and leave behind cavities, which are later filled by osteoblasts. In this way, the continuity of the bone is restored, along with the Haversian systems in the axial direction. If the gap between the bone ends is larger and relative motion is possible between the bone ends, indirect healing occurs. In this scenario, a number of different tissues are formed between the bone ends and the stability of the fracture region is gradually enhanced. In the trabecular bone, osteoblasts deposit new bone in the fracture gap by laying it on the existing bone trabeculae and along the fibers of the fibrous tissue that forms prior to bone formation [175].

In this case-study, the jaw plate was assumed to be able to restrict the relative movement of the bone ends of the mandible with respect to each other. For that reason, the direct bone healing scenario was more likely to occur for the cortical bone.

Lakatos et al. found the modulus of the trabecular bone in the mandible to range from 6.9 MPa to 199.5 MPa [177]. The modulus of the trabecular bone after fracture started from 0 MPa and rose linearly, for the sake of simplicity, to a value of 100 MPa over the course of 168 days. The cortical bone around the

fracture site was initially immature and had a modulus of around 1 GPa [178]. This immature bone was replaced by stronger, mature bone with a modulus of around 6 GPa and later by compact bone [179]. Because the precise rate of stiffening was not available, a rough estimation was made that made the bone modulus increase to 1.3 GPa over the same time period of 168 days.

For the implementation of the beam theory equations, the neutral axis was first calculated with a transformed-section method to take the different materials into account. Then, the area moments of inertia of the different sections were calculated. Finally, the stress in the section that corresponds to the jaw plate was calculated and was converted to a force with the use of integral expressions [180]. For this, the moment in the mandibular body as a result of the biting force was used. The equations were implemented in MATLAB (Mathworks, USA) and automated to loop over different geometries of the cross-section of the plate and material properties of the bone that correspond to the degradation of the plate and the healing of the bone tissue, respectively.

### 10.2.5 Coupling of the models

The biodegradation simulation results were used to derive the changes in geometry on which both the FE analysis and the beam theory analysis relied. The output from the FE simulations delivered the maximum bearable force that the jaw plate can withstand while the output from the beam theory calculations delivered the actual force occurring in the jaw plate, both as a function of time. For that reason, the results could be directly compared to assess the mechanical behavior. However, the missing piece for computing the force in the jaw plate as an integral of the stress over the area of the jaw plate is the fact that stress is a linear function of  $y$ . That means that if the neutral axis is within the jaw plate or very close to it, the force may not be very high, while the maximal stress occurring is actually very high. If this stress is higher than ultimate tensile stress (UTS), it causes problems that might not necessarily be reflected in the total force. What this also reflects is a situation in which the loading of the jaw plate is not predominantly tensile, but instead the jaw plate is under a bending load. Using the force in the jaw plate, as computed by the integral, is only valid if the neutral axis is sufficiently far away from the jaw plate. To check this, the stress variation in the jaw plate and the location of the neutral axis were monitored.

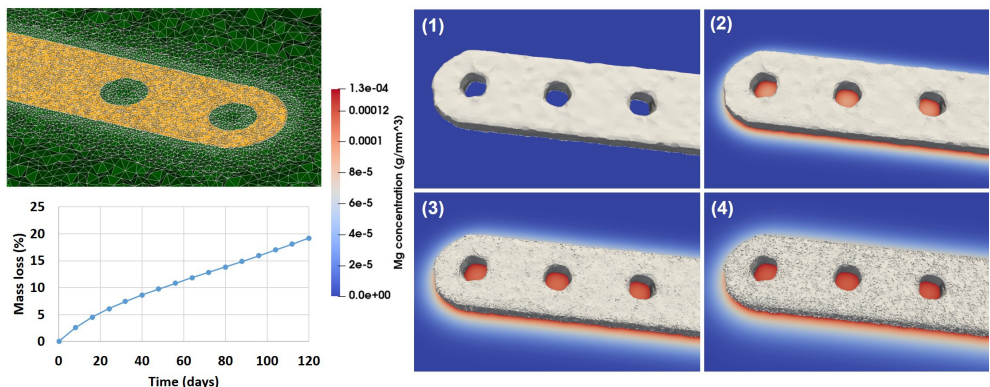


Figure 10.11: A cross-section of the computational mesh and simulation results of the degradation model of the jaw bone plate in SBF solution as well as the mass loss graph over time. The contours display the concentration of magnesium ions on a cross-section view of the medium beside the moving surface of the bone plate at 1) 1st day (initial state), 2) 40th day, 3) 80th day, and 4) 120th day. The gray surface is the zero iso-contour of the level set function, which indicates the surface of the bone plate.

## 10.3 Results

### 10.3.1 Biodegradation results

The simulation of 120 days of the degradation of the jaw bone plate took 18 hours to run using 170 computing cores. Fig. 10.11 shows the visualized interface and magnesium ions release during the corrosion process. It also depicts the mass loss of the bone plate in the SBF solution over time, used to construct the mechanical analysis geometry at certain time points.

### 10.3.2 Sensitivity analyses

The results from the sensitivity analyses showed that the mass scaling and the use of multiple processors for computation had no impact on the force-displacement curves. The maximum degradation only caused changes in the force-displacement curve after the maximum bearable force had been reached, and hence didn't impact the maximum bearable force. The displacement at failure and the mesh size, however, did have a strong impact on the resulting force-

displacement curves. The maximum bearable force was drastically increased with an increased value of the displacement at failure. Changing the mesh size led to the opposite behavior: the maximum bearable force was lower with a larger value of the mesh size. The relationship between both was identified and the misbehavior could be eliminated by adjusting the displacement at failure to the mesh size according to the following general relationship:

$$X_{DAF} = 0.6^{\log_{0.5}(X_{mesh})} \quad (10.1)$$

$X_{DAF}$  is the factor with which the DAF value should be multiplied when the global mesh size is multiplied with  $X_{mesh}$ .

### Mesh check

All models for the tensile tests had four elements in the depth. The relative difference between the maximal force for four elements in the depth compared to five elements in the depth was only 3.4%. The computation time for four elements in the depth of this model was over 4 hours already and refining the mesh to five elements in the depth increased the computation time to over 7 hours. So, the accuracy that would be gained by refining the mesh to five elements in the depth (or further) did not justify the increase in computation time in light of this study.

### Neutral axis and variation in stress in the jaw plate

The location of the neutral axis was analyzed for the five-screw case. It was assumed that in the other cases the behavior was similar. The neutral axis was closest to the jaw plate on day 0 and was at a distance of 7.6 mm from the bottom of the jaw plate at this point. That means that at this point in time, the variation in stress, which was linearly increasing from the neutral axis, was the largest (also taken into account that the force in the jaw plate was the largest at this point). So, to assess the variation of stress in the jaw plate, day 0 should be analyzed. If it is valid at that point in time, then it is valid for the remainder of the simulation. The difference in stress between the top and bottom of the jaw plate was 22.4 MPa at most, which is not too large.

### 10.3.3 Coupled models results

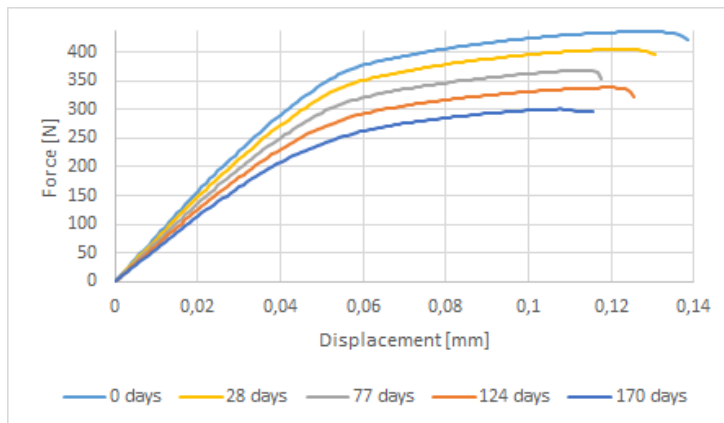


Figure 10.12: Results of tensile test on jaw plate with five screws with different amounts of corrosion

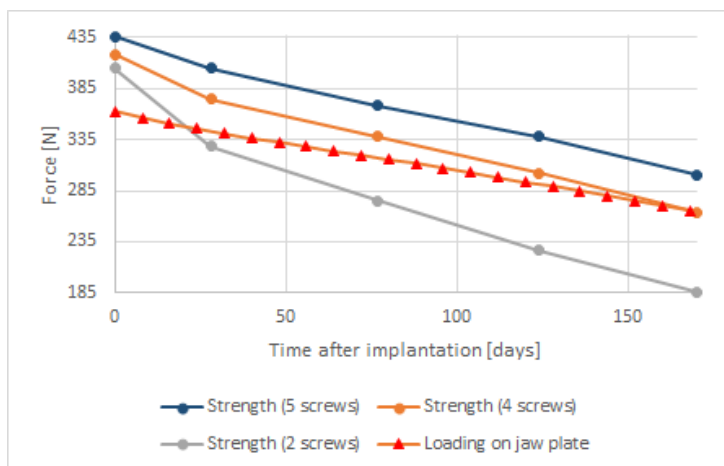


Figure 10.13: Maximal force that can be carried by the jaw plate in each case and estimation of load occurrence as a function of time after implantation in days for five screws

The force-displacement curves for the case with five screws are shown in Fig. 10.12, the cases with four and two screws gave similar force-displacement curves. The strength of the jaw plates was characterized by the maximal values

from the force-displacement curves. In Fig. 10.13, the strength-curves of the jaw plate for the three cases are shown and compared to the loading on the jaw plate, as calculated with beam theory. Comparing the three strength-curves, it could be concluded that leaving more holes open led to a weaker part initially and a faster deterioration of the strength with time as a result of corrosion. In the five-screw case, the strength remained higher than the loading for the simulated time period and hence no failure occurred. In the four- and two-screw cases, failure did occur after about 170 and 20 days respectively.

## 10.4 Discussion

In this work, a coupled mechanical-degradation model was presented to study the effect of biodegradation on the mechanical stability of implants for biodegradable mandibular plates. Three different cases were considered, in each of which a different number of implant holes were left unscrewed. One aspect of the difference between the three cases is the surface that was exposed to body fluids. The extra surfaces exposed to body fluids in the four- and two-screw cases were inside the open holes, which were critical regions. The "extra" corrosion inside the holes had an impact on the strength, as the results of Fig. 10.13 show. The other aspect of the difference between the cases has is on the boundary conditions that represented the screws pulling on the jaw plate. The differences in the maximal force on day 0 between the three cases is a result of the boundary conditions only since there was no corrosion at this point in time and the models were identical.

The use of a "universal" jaw plate with multiple holes allows the jaw plate to be used in various situations involving mandible fractures. Depending on the exact location of fracture lines and the presence of stronger and weaker sections of bone, the amount and placement of screws can be decided upon. The downside to this is that the differences in mechanical behavior and the change thereof as a result of corrosion between the different cases (5/4/2 screws) can lead to unexpected results if not anticipated correctly by the jaw plate designer/surgeon. A patient-specific jaw plate can be designed to meet a specific mechanical behavior. The placement of holes and the presence or absence of screws can then be a powerful tool for obtaining the desired mechanical behavior of the jaw plate.

The results of the strength simulations provided useful knowledge about the

limits in terms of the mechanical strength of the jaw plate and how that evolved during the biodegradation process. Matched with an accurate characterization of the loading, the point at which the jaw plate fails could be predicted. The loading on the jaw plate was derived from the maximal biting force. This has to be taken into account when interpreting the results. The jaw plate would fail if the maximal biting force would be exerted after the point at which the strength curve falls below the loading curve. In practice, the strength of the jaw plate and the way in which this evolves during the biodegradation process are influenced by a range of parameters. Most of these are fixed by the situation/patient: mandible dimensions, bone properties, fracture line geometry, etc. Others are, however, free to be chosen by the implant designer: the jaw plate material and geometry, the location, the number of screws, etc. Certain restrictions on what food may be eaten by the patient for a certain time period can be given to reduce the maximal biting force.

The design of this jaw plate is a complex task that can be modified in various ways. Fig. 10.14 gives an overview of an automated workflow that incorporates the concepts from this study into the iterative design of the jaw plate. With the use of initial data of the mandible and the jaw plate, the mechanical behavior can be determined. Likely, the behavior of the initial design is not as desired. For that reason, the design process is based on the iterative adjustment of the parameters to ultimately obtain the desired mechanical behavior. The material of the jaw plate can be chosen to be stronger or weaker, impacting the estimation of the loading on the jaw plate and the simulation of the strength of the jaw plate. The degradation-related properties of the material impact the corrosion simulation, which in turn determines the geometry changes for the simulation of strength. The geometry of the jaw plate can have similar effects as the material, impacting both strength and degradation behavior. For example, the rate of degradation can be modulated by increasing or decreasing the surface-area-to-volume ratio of the jaw plate. A high surface-area-to-volume ratio (imagine a wide but very thin jaw plate) leads to a faster loss of material (and strength) since the area exposed to body fluids is high. The opposite is true for a low surface-area-to-volume ratio (imagine a jaw plate with a square cross-section perpendicular to the longitudinal axis). The location changes the type of loading on the jaw plate, and it is important that this loading situation is reflected in the simulation of the strength. For example, it is not useful to submit the jaw plate models to a tensile test if the jaw plate is actually experiencing a bending moment once implanted.

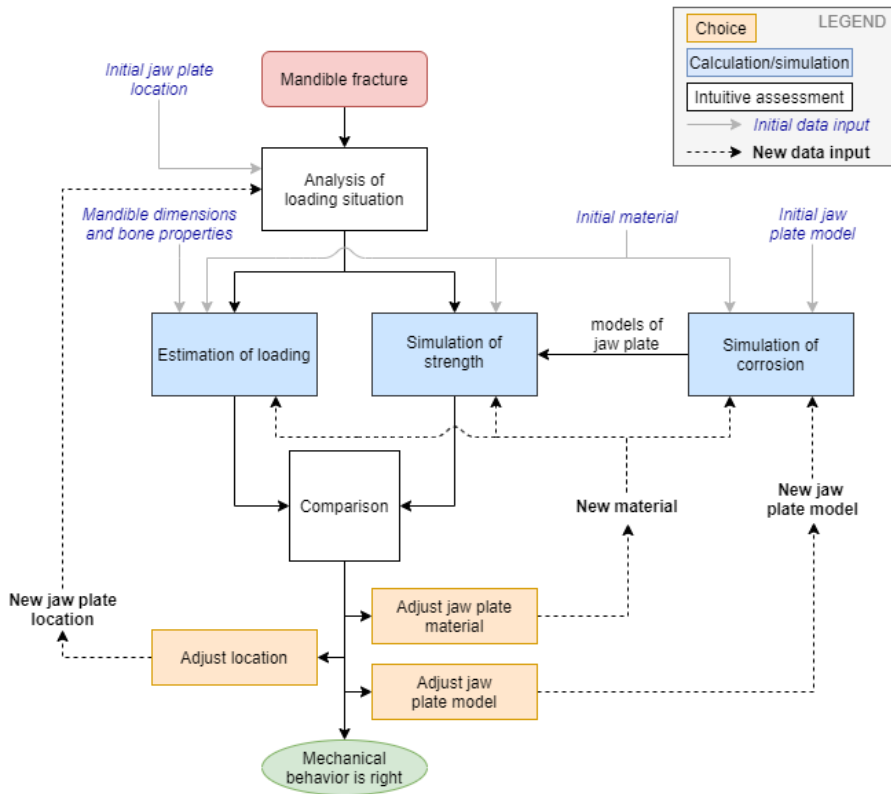


Figure 10.14: Flow chart for the process of iteratively designing a suitable jaw plate

## 10.5 Future perspectives

The validity and accuracy of the curves depend on the data that is used to create them and on the degree to which the simplifications deviate from reality. The E-moduli of the bone could be obtained from dedicated experiments and plugged into the beam theory equations to more accurately define the load on the jaw plate. Alternatively, an FE model of the entire mandible with jaw plate could replace the combination of the beam theory and the FE analysis of the jaw plate separately. This would be more accurate since the loading is not approximated. Another interesting thing to take into account could be the amount of displacement before failure. The area under the force-displacement

curve is an indication of energy absorption. The addition of localized corrosion to the simulations could also be interesting, since the reality of corrosion always involves a combination of localized and uniform corrosion. While the relative change in force values led to interesting conclusions, the absolute values of the results obtained in this study were not validated. Manufacturing real samples, immersing them in SBF, and objecting them to a tensile test would give *in vitro* results that can be compared to the simulation predictions.

## Acknowledgments

This research is financially supported by the Prosperos project, funded by the Interreg VA Flanders The Netherlands program, CCI grant no. 2014TC16RFCB046 and by the Fund for Scientific Research Flanders (FWO), grant G085018N . LG acknowledges support from the European Research Council under the European Unions Horizon 2020 research and innovation programme, ERC CoG 772418. The computational resources and services used in this work were provided by the VSC (Flemish Supercomputer Center), funded by the Research Foundation - Flanders (FWO) and the Flemish Government department EWI.



# Chapter 11

## Applications: Acetabular cup

This chapter is based on prepared manuscript to be submitted to *IEEE Computing in Science & Engineering*:

M. Barzegari, F. Perez-Boerema, G. Zavodszky, and L. Geris, “High-performance computer simulation of biodegradation of optimized personalized implants; a case study of a patient-specific porous acetabular implant,” will be submitted to *IEEE Computing in Science & Engineering*.

### 11.1 Introduction

Before we can take advantage of the interesting properties of metallic biodegradable implants, their biodegradation behavior needs to be evaluated and tuned for the target application. One example from orthopedics is tuning the degradation rate of implants to match the rate of bone formation. *In silico* models can be beneficial in this regard as they can replace resource-consuming *in vitro* or *in vivo* experiments otherwise required. As a case study, in this work, we have developed a computational biodegradation model of a stiffness-optimized patient-specific porous acetabular implant.

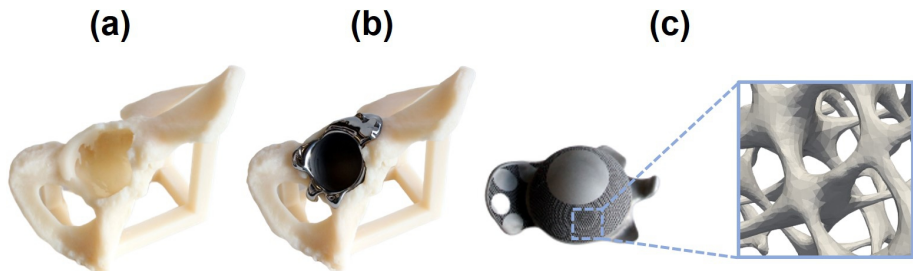


Figure 11.1: Demonstration of the application of a porous acetabular implant.

## 11.2 Materials and Methods

The computational model of the biodegradation process was constructed based on a mechanistic diffusion-reaction model that models the oxidation-reduction reactions occurring during the biodegradation process of metallic materials in simulated body fluid. The finite element method was used to solve the computational model [138]. For building the lattice structure, the in-house developed open-source tool ASLI [181] was used to create a triply periodic minimal surface based infill for the acetabular implant based on the output of a patient-specific topology optimization. The resulting surface mesh, consisting of 5,347,924 faces, was subsequently converted to a volume mesh and embedded in a cubic container that was to act as the environment during the biodegradation simulations. The mesh was refined on the implant/environment interface to increase the numerical accuracy of the model, leading to a final mesh with 45,870,053 elements.

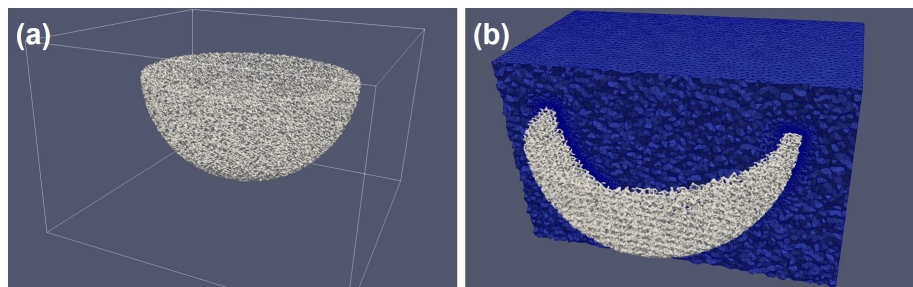


Figure 11.2: The computational model of the optimized acetabular implant embedded inside a cubic container.

For dealing with a problem of this size and making the model capable of being scaled in large-scale computing systems, the model was implemented making use of the high-performance computing (HPC) techniques available in the FreeFEM language v4.10 and PETSc toolkit v3.16.1 [139]. The simulation was carried out using 2,000 CPU cores with 16.5 TB of available memory. The results, with a total size of 148 GB, were visualized using a parallel ParaView server v5.9.1 running on 128 CPU cores. To obtain the scaling behavior of the model in an HPC environment scaling tests were performed by varying the number of employed CPU cores from 60 to 9000.

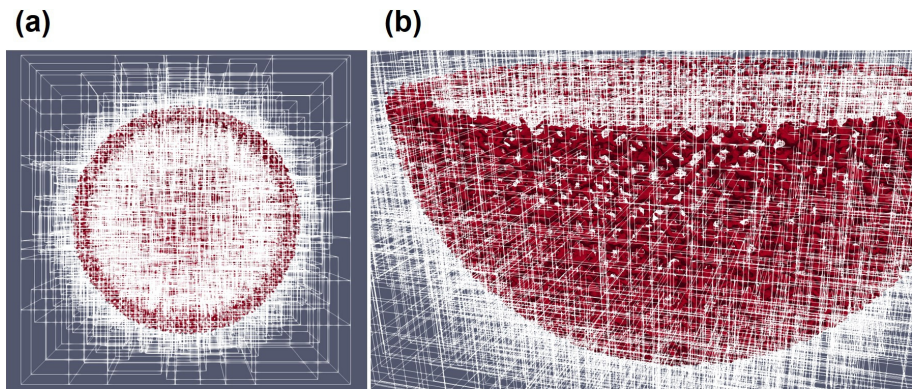


Figure 11.3: Mesh decomposition of the computational biodegradation model to be distributed to available computing nodes.

### 11.3 Results and Discussion

The generated lattice structure of the implant, infilled by skeletal-gyroid unit cell type, is depicted in Fig. 1A. Biodegradation results show that the acetabular implant degrades faster in the region with higher porosity, i.e. the region with more exposed surface area to the environment (Fig. 1B). Loss of material over time was found to be in line with the values obtained in our previous study [138], showing that scaling the model in an HPC environment does not affect the quantitative predictions made by the model. The scaling tests show that the optimal size for the distributed computing environment is 5000 CPU cores, above which no significant improvement in the execution time was observed.

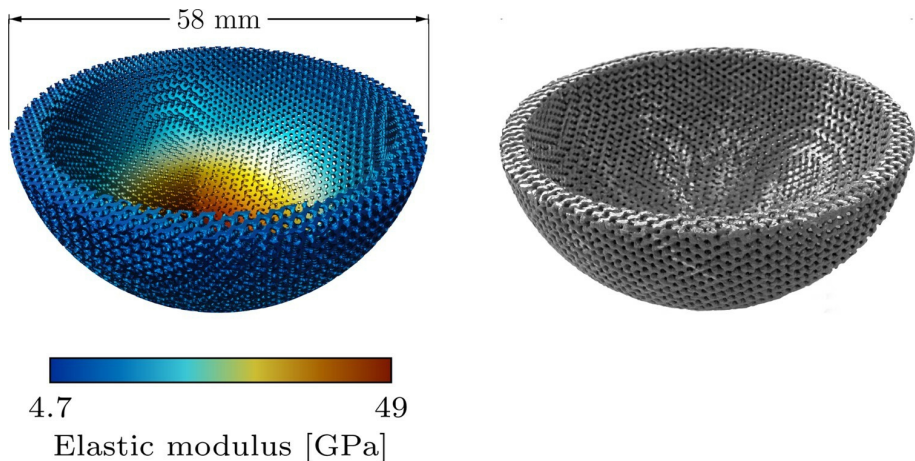


Figure 11.4: Acetabular implant infilled by varying volume fraction to match a desired stiffness distribution.

## 11.4 Conclusions

In this work, taking advantage of HPC techniques to simulate a large-scale 3D model led to a computational model capable of predicting the biodegradation behavior of an acetabular implant in high resolution. Results demonstrate the potential of the model to act as a tool for assessing and tuning the biodegradation properties of orthopedic implants regardless of shape or complexity.

## 11.5 Acknowledgments

Funded by Interreg VA Flanders - Netherlands, (2014TC16RFCB046, Prosp eros) & FWO-Vlaanderen (G085018N).

Dutch supercomputer - Snellius

UK supercomputer - ARCHER2

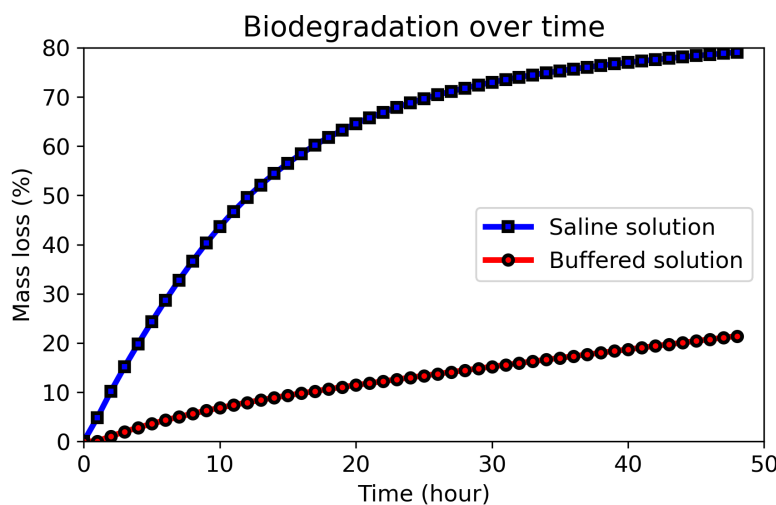


Figure 11.5: Rate of mass loss during the biodegradation of the porous acetabular implant in saline and buffered solutions.

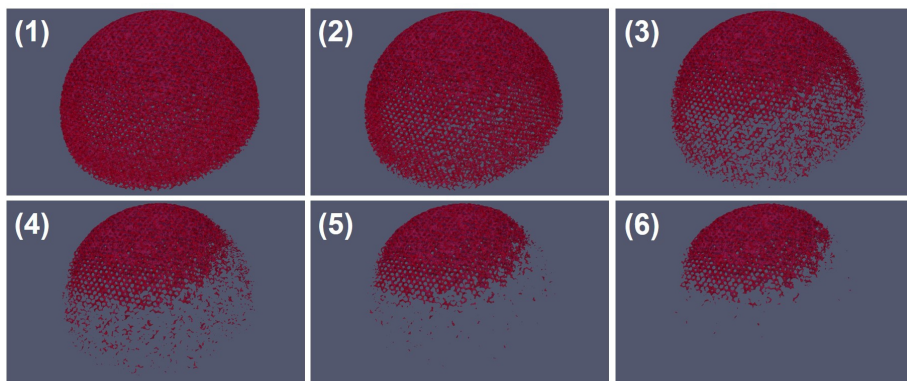


Figure 11.6: Visualization of the change of morphology of the acetabular implant.

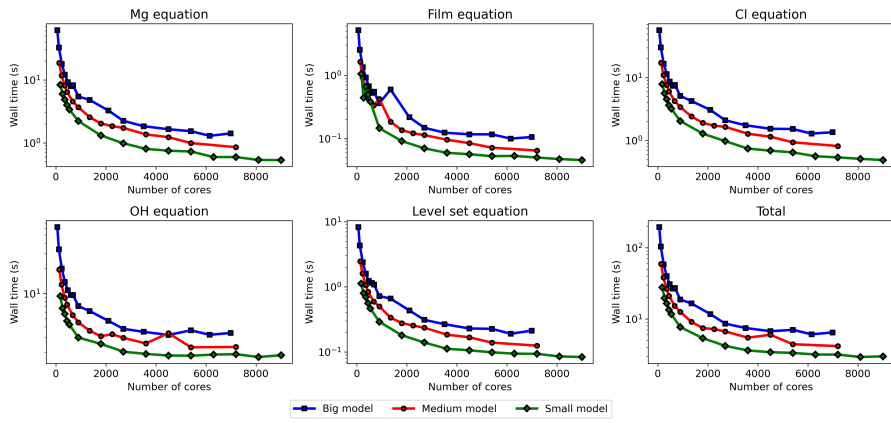


Figure 11.7: Strong scaling of individual components of the biodegradation model.

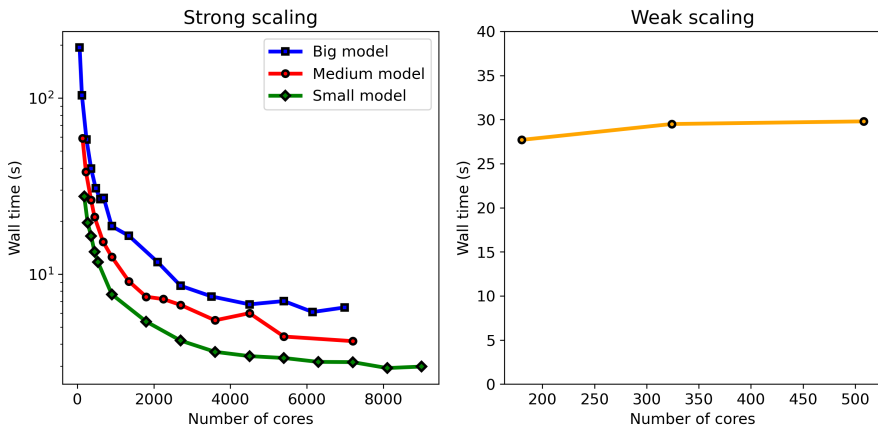


Figure 11.8: Weak and strong scaling of the computational biodegradation model of the acetabular implant.

## **Chapter 12**

# **Applications: Mechanical integrity of infilled structures**



## **Part V**

# **Conclusion and General Discussion**

## **Chapter 13**

# **Conclusion**

...

# Bibliography

- [1] K. Chen, Y. Lu, H. Tang, Y. Gao, F. Zhao, X. Gu, and Y. Fan, "Effect of strain on degradation behaviors of we43, fe and zn wires," *Acta Biomaterialia*, vol. 113, pp. 627 – 645, 2020.
- [2] A. F. S. Reference, "Load-sharing osteosynthesis."
- [3] B. Bohluli, E. Mohammadi, I. zoljanah Oskui, and N. Moharamnejad, "Treatment of mandibular angle fracture: Revision of the basic principles," *Chinese Journal of Traumatology*, vol. 22, no. 2, pp. 117–119, 2019.
- [4] G. Olson and S. Zhang, "Ductilization of high-strength magnesium alloys," 2012.
- [5] T. Odora, "5b. 8. the mandible (lower jaw)."
- [6] S. W. McCormack, U. Witzel, P. J. Watson, M. J. Fagan, and F. Gröning, "Inclusion of periodontal ligament fibres in mandibular finite element models leads to an increase in alveolar bone strains," *PLOS ONE*, vol. 12, pp. 1–23, 11 2017.
- [7] Y. Zheng, X. Gu, and F. Witte, "Biodegradable metals," *Materials Science and Engineering: R: Reports*, vol. 77, pp. 1–34, mar 2014.
- [8] Y. Liu, Y. Zheng, X.-H. Chen, J.-A. Yang, H. Pan, D. Chen, L. Wang, J. Zhang, D. Zhu, S. Wu, K. W. K. Yeung, R.-C. Zeng, Y. Han, and S. Guan, "Fundamental theory of biodegradable metals—definition, criteria, and design," *Advanced Functional Materials*, vol. 29, p. 1805402, feb 2019.
- [9] H.-S. Han, S. Loffredo, I. Jun, J. Edwards, Y.-C. Kim, H.-K. Seok, F. Witte, D. Mantovani, and S. Glyn-Jones, "Current status and outlook on the

- clinical translation of biodegradable metals," *Materials Today*, vol. 23, pp. 57–71, mar 2019.
- [10] D. Zhao, F. Witte, F. Lu, J. Wang, J. Li, and L. Qin, "Current status on clinical applications of magnesium-based orthopaedic implants: A review from clinical translational perspective," *Biomaterials*, vol. 112, pp. 287–302, jan 2017.
- [11] Z. ZHEN, T. fei XI, and Y. feng ZHENG, "A review on in vitro corrosion performance test of biodegradable metallic materials," *Transactions of Nonferrous Metals Society of China*, vol. 23, pp. 2283–2293, aug 2013.
- [12] R. Willumeit-Römer, "The interface between degradable mg and tissue," *JOM*, vol. 71, pp. 1447–1455, feb 2019.
- [13] J. Venezuela and M. Dargusch, "The influence of alloying and fabrication techniques on the mechanical properties, biodegradability and biocompatibility of zinc: A comprehensive review," *Acta Biomaterialia*, vol. 87, pp. 1–40, mar 2019.
- [14] E. Mostaed, M. Sikora-Jasinska, J. W. Drelich, and M. Vedani, "Zinc-based alloys for degradable vascular stent applications," *Acta Biomaterialia*, vol. 71, pp. 1–23, apr 2018.
- [15] M. Schinhammer, A. C. Hänzi, J. F. Löfller, and P. J. Uggowitzer, "Design strategy for biodegradable fe-based alloys for medical applications," *Acta Biomaterialia*, vol. 6, pp. 1705–1713, may 2010.
- [16] M. Esmaily, J. Svensson, S. Fajardo, N. Birbilis, G. Frankel, S. Virtanen, R. Arrabal, S. Thomas, and L. Johansson, "Fundamentals and advances in magnesium alloy corrosion," *Progress in Materials Science*, vol. 89, pp. 92–193, aug 2017.
- [17] B. Heublein, "Biocorrosion of magnesium alloys: a new principle in cardiovascular implant technology?," *Heart*, vol. 89, pp. 651–656, jun 2003.
- [18] M. P. Staiger, A. M. Pietak, J. Huadmai, and G. Dias, "Magnesium and its alloys as orthopedic biomaterials: A review," *Biomaterials*, vol. 27, pp. 1728–1734, mar 2006.
- [19] J. Walker, S. Shadanbaz, T. B. F. Woodfield, M. P. Staiger, and G. J. Dias, "Magnesium biomaterials for orthopedic application: A review from a

- biological perspective," *Journal of Biomedical Materials Research Part B: Applied Biomaterials*, vol. 102, pp. 1316–1331, jan 2014.
- [20] F. Cecchinato, N. A. Agha, A. H. Martinez-Sanchez, B. J. C. Luthringer, F. Feyerabend, R. Jimbo, R. Willumeit-Römer, and A. Wennerberg, "Influence of magnesium alloy degradation on undifferentiated human cells," *PLOS ONE*, vol. 10, p. e0142117, nov 2015.
- [21] D. Mei, S. V. Lamaka, X. Lu, and M. L. Zheludkevich, "Selecting medium for corrosion testing of bioabsorbable magnesium and other metals – a critical review," *Corrosion Science*, vol. 171, p. 108722, jul 2020.
- [22] D. Mei, S. V. Lamaka, J. Gonzalez, F. Feyerabend, R. Willumeit-Römer, and M. L. Zheludkevich, "The role of individual components of simulated body fluid on the corrosion behavior of commercially pure mg," *Corrosion Science*, vol. 147, pp. 81–93, feb 2019.
- [23] R.-C. Zeng, Y. Hu, S.-K. Guan, H.-Z. Cui, and E.-H. Han, "Corrosion of magnesium alloy AZ31: The influence of bicarbonate, sulphate, hydrogen phosphate and dihydrogen phosphate ions in saline solution," *Corrosion Science*, vol. 86, pp. 171–182, sep 2014.
- [24] S. Johnston, M. Dargusch, and A. Atrens, "Building towards a standardised approach to biocorrosion studies: a review of factors influencing mg corrosion in vitro pertinent to in vivo corrosion," *Science China Materials*, vol. 61, pp. 475–500, dec 2017.
- [25] S. V. Lamaka, J. Gonzalez, D. Mei, F. Feyerabend, R. Willumeit-Römer, and M. L. Zheludkevich, "Local pH and its evolution near mg alloy surfaces exposed to simulated body fluids," *Advanced Materials Interfaces*, vol. 5, p. 1800169, jun 2018.
- [26] D. Mei, S. V. Lamaka, C. Feiler, and M. L. Zheludkevich, "The effect of small-molecule bio-relevant organic components at low concentration on the corrosion of commercially pure mg and mg-0.8ca alloy: An overall perspective," *Corrosion Science*, vol. 153, pp. 258–271, jun 2019.
- [27] B. Hadzima, M. Mhaede, and F. Pastorek, "Electrochemical characteristics of calcium-phosphatized AZ31 magnesium alloy in 0.9 % NaCl solution," *Journal of Materials Science: Materials in Medicine*, vol. 25, pp. 1227–1237, jan 2014.

- [28] X. Lu, Y. Li, P. Ju, Y. Chen, J. Yang, K. Qian, T. Zhang, and F. Wang, "Unveiling the inhibition mechanism of an effective inhibitor for AZ91 mg alloy," *Corrosion Science*, vol. 148, pp. 264–271, mar 2019.
- [29] Y. Li, X. Lu, K. Wu, L. Yang, T. Zhang, and F. Wang, "Exploration the inhibition mechanism of sodium dodecyl sulfate on mg alloy," *Corrosion Science*, vol. 168, p. 108559, may 2020.
- [30] A. Atrens, G.-L. Song, M. Liu, Z. Shi, F. Cao, and M. S. Dargusch, "Review of recent developments in the field of magnesium corrosion," *Advanced Engineering Materials*, vol. 17, pp. 400–453, jan 2015.
- [31] C. Schille, M. Braun, H. Wendel, L. Scheideler, N. Hort, H.-P. Reichel, E. Schweizer, and J. Geis-Gerstorfer, "Corrosion of experimental magnesium alloys in blood and PBS: A gravimetric and microscopic evaluation," *Materials Science and Engineering: B*, vol. 176, pp. 1797–1801, dec 2011.
- [32] D. Xue, Y. Yun, Z. Tan, Z. Dong, and M. J. Schulz, "In vivo and in vitro degradation behavior of magnesium alloys as biomaterials," *Journal of Materials Science & Technology*, vol. 28, pp. 261–267, mar 2012.
- [33] Y. Xin, T. Hu, and P. K. Chu, "Degradation behaviour of pure magnesium in simulated body fluids with different concentrations of hco<sub>3</sub>," *Corrosion Science*, vol. 53, pp. 1522–1528, apr 2011.
- [34] N. A. Agha, F. Feyerabend, B. Mihailova, S. Heidrich, U. Bismayer, and R. Willumeit-Römer, "Magnesium degradation influenced by buffering salts in concentrations typical of in vitro and in vivo models," *Materials Science and Engineering: C*, vol. 58, pp. 817–825, jan 2016.
- [35] L.-Y. Cui, Y. Hu, R.-C. Zeng, Y.-X. Yang, D.-D. Sun, S.-Q. Li, F. Zhang, and E.-H. Han, "New insights into the effect of tris-HCl and tris on corrosion of magnesium alloy in presence of bicarbonate, sulfate, hydrogen phosphate and dihydrogen phosphate ions," *Journal of Materials Science & Technology*, vol. 33, pp. 971–986, sep 2017.
- [36] M. B. Kannan, H. Khakbaz, and A. Yamamoto, "Understanding the influence of HEPES buffer concentration on the biodegradation of pure magnesium: An electrochemical study," *Materials Chemistry and Physics*, vol. 197, pp. 47–56, aug 2017.

- [37] Y. Song, D. Shan, R. Chen, F. Zhang, and E.-H. Han, "Biodegradable behaviors of AZ31 magnesium alloy in simulated body fluid," *Materials Science and Engineering: C*, vol. 29, pp. 1039–1045, apr 2009.
- [38] E. L. Silva, S. V. Lamaka, D. Mei, and M. L. Zheludkevich, "The reduction of dissolved oxygen during magnesium corrosion," *ChemistryOpen*, vol. 7, pp. 664–668, aug 2018.
- [39] P. Jiang, C. Blawert, N. Scharnagl, and M. L. Zheludkevich, "Influence of water purity on the corrosion behavior of mg0.5znx (x=ca, ge) alloys," *Corrosion Science*, vol. 153, pp. 62–73, jun 2019.
- [40] D. Mei, C. Wang, S. V. Lamaka, and M. L. Zheludkevich, "Clarifying the influence of albumin on the initial stages of magnesium corrosion in hank's balanced salt solution," *Journal of Magnesium and Alloys*, vol. 9, pp. 805–817, may 2021.
- [41] S. Johnston, Z. Shi, and A. Atrens, "The influence of pH on the corrosion rate of high-purity mg, AZ91 and ZE41 in bicarbonate buffered hanks' solution," *Corrosion Science*, vol. 101, pp. 182–192, dec 2015.
- [42] S. Johnston, Z. Shi, J. Venezuela, C. Wen, M. S. Dargusch, and A. Atrens, "Investigating mg biocorrosion in vitro: Lessons learned and recommendations," *JOM*, vol. 71, pp. 1406–1413, jan 2019.
- [43] C. Wang, D. Mei, G. Wiese, L. Wang, M. Deng, S. V. Lamaka, and M. L. Zheludkevich, "High rate oxygen reduction reaction during corrosion of ultra-high-purity magnesium," *npj Materials Degradation*, vol. 4, dec 2020.
- [44] Y. Chen, Z. Xu, C. Smith, and J. Sankar, "Recent advances on the development of magnesium alloys for biodegradable implants," *Acta Biomaterialia*, vol. 10, pp. 4561–4573, nov 2014.
- [45] Y. Qin, P. Wen, H. Guo, D. Xia, Y. Zheng, L. Jauer, R. Poprawe, M. Voshage, and J. H. Schleifenbaum, "Additive manufacturing of biodegradable metals: Current research status and future perspectives," *Acta Biomaterialia*, vol. 98, pp. 3 – 22, 2019.
- [46] U. Riaz, I. Shabib, and W. Haider, "The current trends of mg alloys in biomedical applications—a review," *Journal of Biomedical Materials Research Part B: Applied Biomaterials*, dec 2018.

- [47] Y. Xin, K. Huo, H. Tao, G. Tang, and P. K. Chu, "Influence of aggressive ions on the degradation behavior of biomedical magnesium alloy in physiological environment," *Acta Biomaterialia*, vol. 4, pp. 2008–2015, nov 2008.
- [48] D. Gastaldi, V. Sassi, L. Petrini, M. Vedani, S. Trasatti, and F. Migliavacca, "Continuum damage model for bioresorbable magnesium alloy devices — application to coronary stents," *Journal of the Mechanical Behavior of Biomedical Materials*, vol. 4, pp. 352–365, apr 2011.
- [49] S. Ahmed, J. Ward, and Y. Liu, "Numerical modelling of effects of biphasic layers of corrosion products to the degradation of magnesium metal in vitro," *Materials*, vol. 11, p. 1, dec 2017.
- [50] J. Grogan, S. Leen, and P. McHugh, "A physical corrosion model for bioabsorbable metal stents," *Acta Biomaterialia*, vol. 10, pp. 2313–2322, may 2014.
- [51] Z. Shen, M. Zhao, D. Bian, D. Shen, X. Zhou, J. Liu, Y. Liu, H. Guo, and Y. Zheng, "Predicting the degradation behavior of magnesium alloys with a diffusion-based theoretical model and in vitro corrosion testing," *Journal of Materials Science & Technology*, vol. 35, pp. 1393–1402, jul 2019.
- [52] J. W. Wilder, C. Clemons, D. Golovaty, K. L. Kreider, G. W. Young, and R. S. Lillard, "An adaptive level set approach for modeling damage due to galvanic corrosion," *Journal of Engineering Mathematics*, vol. 91, pp. 121–142, nov 2014.
- [53] A.-K. Gartzke, S. Julmi, C. Klose, A.-C. Waselau, A. Meyer-Lindenberg, H. J. Maier, S. Besdo, and P. Wriggers, "A simulation model for the degradation of magnesium-based bone implants," *Journal of the Mechanical Behavior of Biomedical Materials*, vol. 101, p. 103411, jan 2020.
- [54] W. Sun, G. Liu, L. Wang, T. Wu, and Y. Liu, "An arbitrary lagrangian-eulerian model for studying the influences of corrosion product deposition on bimetallic corrosion," *Journal of Solid State Electrochemistry*, vol. 17, pp. 829–840, nov 2012.
- [55] P. Bajger, J. M. A. Ashbourn, V. Manhas, Y. Guyot, K. Lietaert, and L. Geris, "Mathematical modelling of the degradation behaviour of biodegradable metals," *Biomechanics and Modeling in Mechanobiology*, vol. 16, pp. 227–238, aug 2016.

- [56] J. Sanz-Herrera, E. Reina-Romo, and A. Boccaccini, "In silico design of magnesium implants: Macroscopic modeling," *Journal of the Mechanical Behavior of Biomedical Materials*, vol. 79, pp. 181–188, mar 2018.
- [57] Y. Gao, L. Wang, X. Gu, Z. Chu, M. Guo, and Y. Fan, "A quantitative study on magnesium alloy stent biodegradation," *Journal of Biomechanics*, vol. 74, pp. 98–105, jun 2018.
- [58] Y. Wang, J. Pan, X. Han, C. Sinka, and L. Ding, "A phenomenological model for the degradation of biodegradable polymers," *Biomaterials*, vol. 29, no. 23, pp. 3393–3401, 2008.
- [59] P. Grindrod, *The theory and applications of reaction-diffusion equations : patterns and waves*. Oxford University Press, 1996.
- [60] J. Crank, *Free and Moving Boundary Problems*. OUP Oxford, 1987.
- [61] S. O. Ronald Fedkiw, *Level Set Methods and Dynamic Implicit Surfaces*. Springer New York, 2002.
- [62] M. Strebl, M. Bruns, and S. Virtanen, "Editors' choice—respirometric in situ methods for real-time monitoring of corrosion rates: Part i. atmospheric corrosion," *Journal of The Electrochemical Society*, vol. 167, p. 021510, jan 2020.
- [63] P. Grathwohl, *Diffusion in Natural Porous Media: Contaminant Transport, Sorption/Desorption and Dissolution Kinetics*. Springer US, 1998.
- [64] D. Höche, "Simulation of corrosion product deposit layer growth on bare magnesium galvanically coupled to aluminum," *Journal of The Electrochemical Society*, vol. 162, pp. C1–C11, nov 2014.
- [65] M. Barzegari and L. Geris, "Highly scalable numerical simulation of coupled reaction-diffusion systems with moving interfaces,"
- [66] S. Scheiner and C. Hellmich, "Stable pitting corrosion of stainless steel as diffusion-controlled dissolution process with a sharp moving electrode boundary," *Corrosion Science*, vol. 49, pp. 319–346, feb 2007.
- [67] F. Hecht, "New development in freefem++," *J. Numer. Math.*, vol. 20, no. 3-4, pp. 251–265, 2012.
- [68] R. D. Falgout and U. M. Yang, "hypre: A library of high performance preconditioners," in *Lecture Notes in Computer Science*, pp. 632–641, Springer Berlin Heidelberg, 2002.

- [69] Y. Saad and M. H. Schultz, "Gmres: A generalized minimal residual algorithm for solving nonsymmetric linear systems," *SIAM Journal on Scientific and Statistical Computing*, vol. 7, no. 3, pp. 856–869, 1986.
- [70] S. Balay, S. Abhyankar, M. F. Adams, J. Brown, P. Brune, K. Buschelman, L. Dalcin, A. Dener, V. Eijkhout, W. D. Gropp, D. Karpeyev, D. Kaushik, M. G. Knepley, D. A. May, L. C. McInnes, R. T. Mills, T. Munson, K. Rupp, P. Sanan, B. F. Smith, S. Zampini, H. Zhang, and H. Zhang, "PETSc Web page." <https://www.mcs.anl.gov/petsc>, 2019.
- [71] P. Jolivet, F. Hecht, F. Nataf, and C. Prudhomme, "Scalable domain decomposition preconditioners for heterogeneous elliptic problems," in *Proceedings of the International Conference on High Performance Computing, Networking, Storage and Analysis*, SC 13, (New York, NY, USA), Association for Computing Machinery, 2013.
- [72] J. Schöberl, "NETGEN an advancing front 2d/3d-mesh generator based on abstract rules," *Computing and Visualization in Science*, vol. 1, pp. 41–52, jul 1997.
- [73] A. Ribes and C. Caremoli, "Salome platform component model for numerical simulation," in *31st Annual International Computer Software and Applications Conference - Vol. 2 - (COMPSAC 2007)*, IEEE, jul 2007.
- [74] J. Mockus, *Bayesian Approach to Global Optimization*. Springer Netherlands, 1989.
- [75] M. Mehrian, Y. Guyot, I. Papantoniou, S. Olofsson, M. Sonnaert, R. Misener, and L. Geris, "Maximizing neotissue growth kinetics in a perfusion bioreactor: An in silico strategy using model reduction and bayesian optimization," *Biotechnology and Bioengineering*, vol. 115, pp. 617–629, dec 2017.
- [76] S. H. Lee and J. C. Rasaiah, "Proton transfer and the mobilities of the H<sup>+</sup> and OH<sup>-</sup> ions from studies of a dissociating model for water," *The Journal of Chemical Physics*, vol. 135, p. 124505, sep 2011.
- [77] J. S. H. Graham C. Hill, *Chemistry in Context - Laboratory Manual*. Oxford University Press, 2001.
- [78] M. Abdalla, A. Joplin, M. Elahinia, and H. Ibrahim, "Corrosion modeling of magnesium and its alloys for biomedical applications: Review," *Corrosion and Materials Degradation*, vol. 1, pp. 219–248, jul 2020.

- [79] R. J. Santucci, M. E. McMahon, and J. R. Scully, "Utilization of chemical stability diagrams for improved understanding of electrochemical systems: evolution of solution chemistry towards equilibrium," *npj Materials Degradation*, vol. 2, jan 2018.
- [80] K. B. Deshpande, "Numerical modeling of micro-galvanic corrosion," *Electrochimica Acta*, vol. 56, pp. 1737–1745, jan 2011.
- [81] O. Dolgikh, H. Simillion, S. V. Lamaka, A. C. Bastos, H. B. Xue, M. G. Taryba, A. R. Oliveira, C. Allély, B. V. D. Bossche, K. V. D. Bergh, J. D. Strycker, and J. Deconinck, "Corrosion protection of steel cut-edges by hot-dip galvanized al(zn,mg) coatings in 1 wt% NaCl: Part II. numerical simulations," *Materials and Corrosion*, vol. 70, pp. 780–792, jan 2019.
- [82] T. J. Chung, *Computational Fluid Dynamics*. Cambridge University Press, 2014.
- [83] A. Quarteroni, "Navier-stokes equations," in *Numerical Models for Differential Problems*, pp. 429–482, Springer Milan, 2014.
- [84] V. Girault and P.-A. Raviart, *Finite Element Approximation of the Navier-Stokes Equations*. Springer Berlin Heidelberg, 1979.
- [85] H. Elman, D. Silvester, and A. Wathen, *Finite Elements and Fast Iterative Solvers with Applications in Incompressible Fluid Dynamics*. Oxford University PressOxford, jun 2014.
- [86] F. de Vuyst, "Numerical modeling of transport problems using freefem++ software – with examples in biology, CFD, traffic flow and energy transfer." Lecture, Sept. 2013.
- [87] Y. Guyot, I. Papantoniou, F. P. Luyten, and L. Geris, "Coupling curvature-dependent and shear stress-stimulated neotissue growth in dynamic bioreactor cultures: a 3d computational model of a complete scaffold," *Biomechanics and Modeling in Mechanobiology*, vol. 15, pp. 169–180, jan 2016.
- [88] Y. Sun and C. Beckermann, "Sharp interface tracking using the phase-field equation," *Journal of Computational Physics*, vol. 220, pp. 626–653, jan 2007.
- [89] S. Osher and J. A. Sethian, "Fronts propagating with curvature-dependent speed: Algorithms based on hamilton-jacobi formulations," *Journal of Computational Physics*, vol. 79, pp. 12–49, nov 1988.

- [90] A. M. Andrew, "Level set methods and fast marching methods: Evolving interfaces in computational geometry, fluid mechanics, computer vision, and materials science, by j.a. sethian, cambridge university press, cambridge, uk, 2nd edn. 1999 (first published 1996 as level set methods) xviii + 420pp., isbn (paperback) 0-521-64557-3, (hardback) 0-521-64204-3 (pbk, £18.95)," *Robotica*, vol. 18, p. 8992, jan 2000.
- [91] W. J. Rider and D. B. Kothe, "Reconstructing volume tracking," *Journal of Computational Physics*, vol. 141, pp. 112–152, apr 1998.
- [92] W. J. Boettinger, J. A. Warren, C. Beckermann, and A. Karma, "Phase-field simulation of solidification," *Annual Review of Materials Research*, vol. 32, pp. 163–194, aug 2002.
- [93] I. Bellemans, N. Moelans, and K. Verbeken, "Phase-field modelling in extractive metallurgy," *Critical Reviews in Solid State and Materials Sciences*, vol. 43, pp. 417–454, dec 2017.
- [94] A. Karma and W.-J. Rappel, "Quantitative phase-field modeling of dendritic growth in two and three dimensions," *Physical Review E*, vol. 57, pp. 4323–4349, apr 1998.
- [95] L.-Q. Chen, "Phase-field models for microstructure evolution," *Annual Review of Materials Research*, vol. 32, pp. 113–140, aug 2002.
- [96] L.-Q. Chen and W. Yang, "Computer simulation of the domain dynamics of a quenched system with a large number of nonconserved order parameters: The grain-growth kinetics," *Physical Review B*, vol. 50, pp. 15752–15756, dec 1994.
- [97] H. Henry and H. Levine, "Dynamic instabilities of fracture under biaxial strain using a phase field model," *Physical Review Letters*, vol. 93, sep 2004.
- [98] R. Spatschek, E. Brener, and A. Karma, "Phase field modeling of crack propagation," *Philosophical Magazine*, vol. 91, pp. 75–95, jan 2011.
- [99] D. N. Bhate, A. Kumar, and A. F. Bower, "Diffuse interface model for electromigration and stress voiding," *Journal of Applied Physics*, vol. 87, pp. 1712–1721, feb 2000.
- [100] W. Mai, S. Soghrati, and R. G. Buchheit, "A phase field model for simulating the pitting corrosion," *Corrosion Science*, vol. 110, pp. 157–166, sep 2016.

- [101] C. Lin, H. Ruan, and S.-Q. Shi, "Phase field study of mechanico-electrochemical corrosion," *Electrochimica Acta*, vol. 310, pp. 240–255, jul 2019.
- [102] A. Imanian and M. Amiri, "Phase field modeling of galvanic corrosion," 2018.
- [103] C. Lin and H. Ruan, "Multi-phase-field modeling of localized corrosion involving galvanic pitting and mechano-electrochemical coupling," *Corrosion Science*, vol. 177, p. 108900, dec 2020.
- [104] T. Q. Ansari, Z. Xiao, S. Hu, Y. Li, J.-L. Luo, and S.-Q. Shi, "Phase-field model of pitting corrosion kinetics in metallic materials," *npj Computational Materials*, vol. 4, jul 2018.
- [105] C. Tsuyuki, A. Yamanaka, and Y. Ogimoto, "Phase-field modeling for pH-dependent general and pitting corrosion of iron," *Scientific Reports*, vol. 8, aug 2018.
- [106] A. F. Chadwick, J. A. Stewart, R. A. Enrique, S. Du, and K. Thornton, "Numerical modeling of localized corrosion using phase-field and smoothed boundary methods," *Journal of The Electrochemical Society*, vol. 165, no. 10, pp. C633–C646, 2018.
- [107] D. Jeong and J. Kim, "Phase-field model and its splitting numerical scheme for tissue growth," *Applied Numerical Mathematics*, vol. 117, pp. 22–35, jul 2017.
- [108] H. G. Lee, J. Park, S. Yoon, C. Lee, and J. Kim, "Mathematical model and numerical simulation for tissue growth on bioscaffolds," *Applied Sciences*, vol. 9, p. 4058, sep 2019.
- [109] C. Beckermann, H.-J. Diepers, I. Steinbach, A. Karma, and X. Tong, "Modeling melt convection in phase-field simulations of solidification," *Journal of Computational Physics*, vol. 154, pp. 468–496, sep 1999.
- [110] J. Shen, , and X. Y. and, "Numerical approximations of allen-cahn and cahn-hilliard equations," *Discrete & Continuous Dynamical Systems - A*, vol. 28, no. 4, pp. 1669–1691, 2010.
- [111] H. Abboud, C. A. Kosseifi, and J.-P. Chehab, "A stabilized bi-grid method for allen-cahn equation in finite elements," *Computational and Applied Mathematics*, vol. 38, mar 2019.

- [112] A. S. Vagbharathi and S. Gopalakrishnan, "An extended finite-element model coupled with level set method for analysis of growth of corrosion pits in metallic structures," *Proceedings of the Royal Society A: Mathematical, Physical and Engineering Sciences*, vol. 470, p. 20140001, aug 2014.
- [113] R. Duddu, "Numerical modeling of corrosion pit propagation using the combined extended finite element and level set method," *Computational Mechanics*, vol. 54, pp. 613–627, apr 2014.
- [114] Z. Xu, H. Huang, X. Li, and P. Meakin, "Phase field and level set methods for modeling solute precipitation and/or dissolution," *Computer Physics Communications*, vol. 183, pp. 15–19, jan 2012.
- [115] W. Chen and E. D. Schutter, "Parallel STEPS: Large scale stochastic spatial reaction-diffusion simulation with high performance computers," *Frontiers in Neuroinformatics*, vol. 11, feb 2017.
- [116] S. N. Arjunan, A. Miyauchi, K. Iwamoto, and K. Takahashi, "pSpatioocyte: a high-performance simulator for intracellular reaction-diffusion systems," *BMC Bioinformatics*, vol. 21, jan 2020.
- [117] M. J. Hallock, J. E. Stone, E. Roberts, C. Fry, and Z. Luthey-Schulten, "Simulation of reaction diffusion processes over biologically relevant size and time scales using multi-GPU workstations," *Parallel Computing*, vol. 40, pp. 86–99, may 2014.
- [118] B. E. Kendall, C. J. Briggs, W. W. Murdoch, P. Turchin, S. P. Ellner, E. McCauley, R. M. Nisbet, and S. N. Wood, "WHY DO POPULATIONS CYCLE? a SYNTHESIS OF STATISTICAL AND MECHANISTIC MODELING APPROACHES," *Ecology*, vol. 80, pp. 1789–1805, sep 1999.
- [119] J. Ahrens, B. Geveci, and C. Law, "Paraview: An end-user tool for large data visualization," *The visualization handbook*, vol. 717, 2005.
- [120] E. Wendland and H. Schulz, "Numerical experiments on mass lumping for the advection-diffusion equation," *Pesquisa e Tecnologia Minerva*, vol. 2, pp. 227–233, 01 2005.
- [121] M. Badri, P. Jolivet, B. Rousseau, and Y. Favennec, "High performance computation of radiative transfer equation using the finite element method," *Journal of Computational Physics*, vol. 360, pp. 74–92, may 2018.

- [122] H. A. Daas, L. Grigori, P. Jolivet, and P.-H. Tournier, “A multilevel schwarz preconditioner based on a hierarchy of robust coarse spaces,” 2019.
- [123] G. Karypis and V. Kumar, “A fast and high quality multilevel scheme for partitioning irregular graphs,” *SIAM J. Sci. Comput.*, vol. 20, p. 359392, Dec. 1998.
- [124] V. Dolean, P. Jolivet, and F. Nataf, *An Introduction to Domain Decomposition Methods*. Philadelphia, PA: Society for Industrial and Applied Mathematics, 2015.
- [125] P. R. Amestoy, I. S. Duff, J. Koster, and J.-Y. L'Excellent, “A fully asynchronous multifrontal solver using distributed dynamic scheduling,” *SIAM Journal on Matrix Analysis and Applications*, vol. 23, no. 1, pp. 15–41, 2001.
- [126] Y. Saad, *Iterative Methods for Sparse Linear Systems*. Society for Industrial and Applied Mathematics, jan 2003.
- [127] I. C. F. Ipsen and C. D. Meyer, “The idea behind krylov methods,” *The American Mathematical Monthly*, vol. 105, pp. 889–899, dec 1998.
- [128] M. R. Hestenes, E. Stiefel, *et al.*, “Methods of conjugate gradients for solving linear systems,” *Journal of research of the National Bureau of Standards*, vol. 49, no. 6, pp. 409–436, 1952.
- [129] G. J. Habetler and E. L. Wachspress, “Symmetric successive over-relaxation in solving diffusion difference equations,” *Mathematics of Computation*, pp. 356–362, 1961.
- [130] S. F. McCormick, *Multigrid methods*. SIAM, 1987.
- [131] G. Russo and P. Smereka, “A remark on computing distance functions,” *Journal of Computational Physics*, vol. 163, pp. 51–67, sep 2000.
- [132] N. I. Z. Abidin, B. Rolfe, H. Owen, J. Malisano, D. Martin, J. Hofstetter, P. J. Uggowitzer, and A. Atrens, “The in vivo and in vitro corrosion of high-purity magnesium and magnesium alloys WZ21 and AZ91,” *Corrosion Science*, vol. 75, pp. 354–366, oct 2013.
- [133] J. L. Gustafson, “Reevaluating amdahl's law,” *Communications of the ACM*, vol. 31, pp. 532–533, may 1988.

- [134] G. M. Amdahl, "Validity of the single processor approach to achieving large scale computing capabilities," in *Proceedings of the April 18-20, 1967, spring joint computer conference on - AFIPS' 67 (Spring)*, ACM Press, 1967.
- [135] A. Ghai, C. Lu, and X. Jiao, "A comparison of preconditioned krylov subspace methods for large-scale nonsymmetric linear systems," *Numerical Linear Algebra with Applications*, vol. 26, p. e2215, oct 2018.
- [136] A. M. Hassan and M. El-Shenawee, "Parallel implementation of the diffusion-drift algorithm for modeling the electrophysiological activity of breast tumors," *Journal of Parallel and Distributed Computing*, vol. 71, pp. 1011–1023, jul 2011.
- [137] C. Rettinger, C. Godenschwager, S. Eibl, T. Preclik, T. Schruff, R. Frings, and U. Rüde, "Fully resolved simulations of dune formation in riverbeds," in *High Performance Computing* (J. M. Kunkel, R. Yokota, P. Balaji, and D. Keyes, eds.), (Cham), pp. 3–21, Springer International Publishing, 2017.
- [138] M. Barzegari, D. Mei, S. V. Lamaka, and L. Geris, "Computational modeling of degradation process of biodegradable magnesium biomaterials," *Corrosion Science*, vol. 190, p. 109674, 2021.
- [139] M. Barzegari and L. Geris, "Highly scalable numerical simulation of coupled reactiondiffusion systems with moving interfaces," *The International Journal of High Performance Computing Applications*, vol. 36, no. 2, pp. 198–213, 2022.
- [140] D. Höche, "Simulation of corrosion product deposit layer growth on bare magnesium galvanically coupled to aluminum," *Journal of The Electrochemical Society*, vol. 162, no. 1, pp. C1–C11, 2014.
- [141] J. Sanz-Herrera, E. Reina-Romo, and A. Boccaccini, "In silico design of magnesium implants: Macroscopic modeling," *Journal of the Mechanical Behavior of Biomedical Materials*, vol. 79, pp. 181–188, mar 2018.
- [142] C. Köhn, D. van Laethem, J. Deconinck, and A. Hubin, "A simulation study of steric effects on the anodic dissolution at high current densities," *Materials and Corrosion*, vol. 72, no. 4, pp. 610–619, 2021.
- [143] T. G. Kurtz, "The relationship between stochastic and deterministic models for chemical reactions," *The Journal of Chemical Physics*, vol. 57, no. 7, pp. 2976–2978, 1972.

- [144] C. Dapogny, C. Dobrzynski, and P. Frey, "Three-dimensional adaptive domain remeshing, implicit domain meshing, and applications to free and moving boundary problems," *Journal of Computational Physics*, 2014.
- [145] M. Barzegari and L. Geris, "Biodeg corrosion and biodegradation simulation software: user manual and theory guide," 2022.
- [146] M. Dehghan, "An inverse problem of finding a source parameter in a semilinear parabolic equation," *Applied Mathematical Modelling*, vol. 25, no. 9, pp. 743–754, 2001.
- [147] A. Tarantola, *Inverse Problem Theory: Methods for Data Fitting and Model Parameter Estimation*. Elsevier Science Ltd, 1987.
- [148] P. Magni and G. Sparacino, "5 - parameter estimation," in *Modelling Methodology for Physiology and Medicine (Second Edition)* (E. Carson and C. Cobelli, eds.), pp. 83 – 110, Elsevier, second edition ed., 2014.
- [149] J. Bergstra, D. Yamins, and D. D. Cox, "Making a science of model search: Hyperparameter optimization in hundreds of dimensions for vision architectures," in *Proceedings of the 30th International Conference on Machine Learning - Volume 28*, p. I115I123, JMLR.org, 2013.
- [150] O. Chen, S. Kalyuga, and J. Sweller, "The worked example effect, the generation effect, and element interactivity," *Journal of Educational Psychology*, vol. 107, no. 3, p. 689704, 2015.
- [151] M. K., S. M.P., and M. K., "Stent thrombosis," *Treasure Island (FL), StatPearls Publishing*, 2020.
- [152] G. M. Raghavendra, K. Varaprasad, and T. Jayaramudu, "Chapter 2 - biomaterials: Design, development and biomedical applications," in *Nanotechnology Applications for Tissue Engineering* (S. Thomas, Y. Grohens, and N. Ninan, eds.), pp. 21 – 44, Oxford: William Andrew Publishing, 2015.
- [153] H.-S. Han, S. Loffredo, I. Jun, J. Edwards, Y.-C. Kim, H.-K. Seok, F. Witte, D. Mantovani, and S. Glyn-Jones, "Current status and outlook on the clinical translation of biodegradable metals," *Materials Today*, vol. 23, pp. 57 – 71, 2019.
- [154] J. Chen, L. Tan, X. Yu, I. P. Etim, M. Ibrahim, and K. Yang, "Mechanical properties of magnesium alloys for medical application: A review,"

- Journal of the Mechanical Behavior of Biomedical Materials*, vol. 87, pp. 68 – 79, 2018.
- [155] Y. Yang, C. He, Dianyu E, W. Yang, F. Qi, D. Xie, L. Shen, S. Peng, and C. Shuai, “Mg bone implant: Features, developments and perspectives,” *Materials & Design*, vol. 185, p. 108259, 2020.
  - [156] D. B. M. R. D. in Department of Oral, M. S. N. P. D. College, and H. Visnagar, “Mandible fractures.”
  - [157] F. E. Levy, R. W. Smith, R. M. Odland, and L. J. Marentette, “Monocortical Miniplate Fixation of Mandibular Angle Fractures,” *Archives of Otolaryngology Head & Neck Surgery*, vol. 117, pp. 149–154, 02 1991.
  - [158] A. Vautrin, M. Wesseling, R. Wirix-Speetjens, and M. J. Gomez-Benito, “Time-dependent in silico modelling of orthognathic surgery to support the design of biodegradable bone plates,” *Journal of the Mechanical Behavior of Biomedical Materials*, vol. 121, p. 104641, 2021.
  - [159] K. Zheng, Z. Liao, N. Yoda, J. Fang, J. Chen, Z. Zhang, J. Zhong, C. Peck, K. Sasaki, M. V. Swain, and Q. Li, “Investigation on masticatory muscular functionality following oral reconstruction an inverse identification approach,” *Journal of Biomechanics*, vol. 90, pp. 1–8, 2019.
  - [160] C. Wu, K. Zheng, J. Fang, G. P. Steven, and Q. Li, “Time-dependent topology optimization of bone plates considering bone remodeling,” *Computer Methods in Applied Mechanics and Engineering*, vol. 359, p. 112702, 2020.
  - [161] A. Boccaccio, P. Prendergast, C. Pappalettere, and D. Kelly, “Tissue differentiation and bone regeneration in an osteotomized mandible: A computational analysis of the latency period,” *Medical & biological engineering & computing*, vol. 46, pp. 283–98, 04 2008.
  - [162] H. Mehboob and S.-H. Chang, “Optimal design of a functionally graded biodegradable composite bone plate by using the taguchi method and finite element analysis,” *Composite Structures*, vol. 119, p. 166173, 01 2015.
  - [163] S. Ma, B. Zhou, and B. Markert, “Numerical simulation of the tissue differentiation and corrosion process of biodegradable magnesium implants during bone fracture healing,” *ZAMM - Journal of Applied Mathematics and Mechanics / Zeitschrift für Angewandte Mathematik und Mechanik*, vol. 98, 08 2018.

- [164] J. Alierta, M. Pérez, and J. M. Garcia Aznar, "An interface finite element model can be used to predict healing outcome of bone fractures," *Journal of the mechanical behavior of biomedical materials*, vol. 29C, pp. 328–338, 10 2013.
- [165] A. Inc., "Abaqus/explicit: Advanced topics."
- [166] Abaqus, "Damage evolution and element removal for ductile metals (documentation)."
- [167] M. Islam, "How to perform element deletion in abaqus using ductile damage criteria?," 05 2018.
- [168] J. Reina, J. García-Aznar, J. Domínguez, and M. Doblaré, "Numerical estimation of bone density and elastic constants distribution in a human mandible," *Journal of Biomechanics*, vol. 40, no. 4, pp. 828–836, 2007.
- [169] T. Korieth, D. Romilly, and A. Hannam, "Three-dimensional finite element stress analysis of the dentate human mandible.," *American journal of physical anthropology*, vol. 88 1, pp. 69–96, 1992.
- [170] A. Mansour, "A comparison of orthodontic elastic forces: Focus on reduced inventory," *journal of orthodontic science*, vol. 6, p. 136, 10 2017.
- [171] Dent-Wiki, "Form and function of the dentition."
- [172] S. Sittitavornwong, D. Ashley, D. Denison, D. Walma, S. Potter, C. P. Lin, and J. Freind, "Assessment of the integrity of adult human mandibular angle," *Craniomaxillofacial Trauma & Reconstruction Open*, vol. 03, pp. e18–e23, 01 2019.
- [173] R. More and A. Reddy, "Study of mandibular thickness in dentulous and edentulous mandibles," *Indian Journal of Clinical Anatomy and Physiology*, vol. 5, pp. 457–460, 11 2018.
- [174] A. Katranchi, K. Misch, and H.-L. Wang, "Cortical bone thickness in dentate and edentulous human cadavers," *Journal of periodontology*, vol. 78, pp. 874–8, 06 2007.
- [175] K. Voss and P. Montavon, "13 - fractures," in *Feline Orthopedic Surgery and Musculoskeletal Disease* (P. Montavon, K. Voss, and S. Langley-Hobbs, eds.), pp. 129–152, Edinburgh: W.B. Saunders, 2009.

- [176] R. Marsell and T. A. Einhorn, "The biology of fracture healing," *Injury*, vol. 42, no. 6, pp. 551–555, 2011. Bone Regeneration in the 21st Century.
- [177] E. Lakatos, L. Magyar, and I. Bojtár, "Material properties of the mandibular trabecular bone," *Journal of Medical Engineering*, vol. 2014, 10 2014.
- [178] H. Isaksson, C. van Donkelaar, and K. Ito, "Sensitivity of tissue differentiation and bone healing predictions to tissue properties," *Journal of biomechanics*, vol. 42, pp. 555–64, 03 2009.
- [179] H. Histology, "Part b types of bone."
- [180] S. K. Fenster and A. C. Ugural, *Advanced Mechanics of Materials and Applied Elasticity*, ch. 5.9. Pearson, 8 2019.
- [181] F. Perez-Boerema, M. Barzegari, and L. Geris, "A flexible and easy-to-use open-source tool for designing functionally graded 3d porous structures," *Virtual and Physical Prototyping*, vol. 17, pp. 682–699, mar 2022.

# List of publications

## Publications in refereed journals

1. H. Keramati, F. Hamdullahpur, **M. Barzegari**, "Deep reinforcement learning for heat exchanger shape optimization", *International Journal Of Heat And Mass Transfer*, 2022
2. **M. Barzegari**, L. Geris, "BioDeg: A finite element software for the simulation of the corrosion and biodegradation process in metallic biomaterials", *Journal of Open Source Software*, 2022
3. F. Perez Boerema, **M. Barzegari**, L. Geris, "A flexible and easy-to-use open-source tool for designing functionally graded 3D porous structures", *Virtual And Physical Prototyping*, 2022
4. D. Van Hede, B. Liang, S. Anania, **M. Barzegari**, B. Verlee, G. Nolens, J. Pirson, L. Geris, F. Lambert, "3D-Printed Synthetic Hydroxyapatite Scaffold With In Silico Optimized Macrostructure Enhances Bone Formation In Vivo", *Advanced Functional Materials*, 2021
5. **M. Barzegari**, L. Geris, "Highly scalable numerical simulation of coupled reaction-diffusion systems with moving interfaces", *Journal of High Performance Computing Applications*, 2021
6. **M. Barzegari**, D. Mei, S.V. Lamaka, L. Geris, "Computational modeling of degradation process of biodegradable magnesium biomaterials", *Corrosion Science*, 2021
7. J. Barrasa Fano, A. Shapeti, A. Jorge Peñas, **M. Barzegari**, J.A. Sanz-Herrera, H. Van Oosterwyck, "TFMLAB: a MATLAB toolbox for 4D Traction Force Microscopy", *SoftwareX*, 2021

8. **M. Barzegari**, L. Geris, "An open source crash course on parameter estimation of computational models using a Bayesian optimization approach", *Journal of Open Source Education*, 2021
9. F. Firouzi, B. Farahani, **M. Barzegari**, M. Daneshmand, "AI-Driven Data Monetization: The other Face of Data in IoT-based Smart and Connected Health", *IEEE Internet of Things Journal*, 2020
10. **M. Barzegari**, B. Vahidi, M.R. Safarinejad, M. Ebad, "A computational analysis of the effect of supporting organs on predicted vesical pressure in stress urinary incontinence", *Medical & Biological Engineering & Computing*, 2020
11. B. Farahani, **M. Barzegari**, F. Shams Aliee, K. A. Shaik, "Towards collaborative intelligent IoT eHealth: From device to fog, and cloud", *Microprocessors and Microsystems*, 2020
12. **M. Barzegari**, H. Bayani, S. M. H. Mirbagheri, and H. Shetabivash, "Multiphase aluminum A356 foam formation process simulation using lattice Boltzmann method", *Journal of Materials Research and Technology*, 2019
13. H. Bayani, S. M. H. Mirbagheri, **M. Barzegari**, and S. Firoozi, "Simulation of Unconstrained Solidification of A356 Aluminium Alloy on Distribution of Micro/Macro Shrinkage", *Journal of Materials Research and Technology*, 2014

## Publications as Book Chapters

1. F. Firouzi, B. Farahani, F. Ye, **M. Barzegari**, "Machine Learning for IoT", *Intelligent Internet of Things*, Springer International Publishing, 2020
2. S. M. H. Mirbagheri, H. Bayani, **M. Barzegari**, S. Firoozi, "Simulation of Liquid Flow Permeability for Dendritic Structures during Solidification Process", *Computational Fluid Dynamics Technologies and Applications*, In-tec, 2011

## Preprints

1. T. Herpelinck, L. Ory, G. Nasello, **M. Barzegari**, J. Bolander, F.P. Luyten, P. Tylzanowski, L. Geris, "An integrated single-cell atlas of the skeleton from development through adulthood", biorXiv Preprint
2. **M. Barzegari**, H. Bayani, S. M. H. Mirbagheri, "A Criterion for Bubble Merging in Liquid Metal: Computational and Experimental Study", arXiv Preprint
3. **M. Barzegari**, B. Vahidi, M. R. Safarinejad, M. Hashemipour "Pathological Analysis of Stress Urinary Incontinence in Females using Artificial Neural Networks", arXiv Preprint

## Publications in refereed conference proceedings

1. F. Firouzi, B. Farahani, E. Panahi, **M. Barzegari**, " Task Offloading for Edge-Fog-Cloud Interplay in the Healthcare Internet of Things (IoT)", *Proceedings of the International Conference on Omni-Layer Intelligent Systems*, 2021
2. B. Farahani, **M. Barzegari**, F. Shams Aliee, " Towards Collaborative Machine Learning Driven Healthcare Internet of Things", *Proceedings of the International Conference on Omni-Layer Intelligent Systems*, 2019

## Conference and symposium abstracts (first author)

1. (Oral presentation) **M. Barzegari**, F. Perez-Boerema, G. Zavodszky, L. Geris, "High-performance computational modeling of metallic biomaterials biodegradation; a case study of a personalized biodegradable porous acetabular ". Virtual Physiological Human Conference (VPH), 2022
2. (Oral presentation) **M. Barzegari**, L. Geris, "Mathematical investigation of corrosion behavior of bioabsorbable metals on the biodegradation interface". 8th European Congress on Computational Methods in Applied Sciences and Engineering (ECCOMAS), 2022

3. (Oral presentation) **M. Barzegari**, L. Geris, "Massively parallel finite element simulation of reaction-diffusion systems with moving boundaries: a use-case for biomaterials degradation modeling". HPC Asia, 2022
4. (Oral presentation) **M. Barzegari**, L. Geris, "BioDeg: corrosion/biodegradation simulation software for metallic biomaterials based on FreeFEM-PETSc-Qt". FreeFEM Days, 13th Edition, 2021
5. (Oral presentation) **M. Barzegari**, L. Geris, "Interactive Educational Materials for Computational Tissue Engineering Using Jupyter Notebooks". 6th World Congress of Tissue Engineering and Regenerative Medicine International Society (TERMIS), 2021
6. (Oral presentation) **M. Barzegari**, L. Geris, "Mathematical modeling of curvature-based cell/tissue growth on open porous scaffolds for bone tissue engineering". 8th Belgian Symposium on Tissue Engineering, 2021
7. (Oral presentation) **M. Barzegari**, L. Geris, "Physics-informed neural network model for cell viability and oxygen consumption of pancreatic islets". Mechanistic Machine Learning and Digital Twins for Computational Science, Engineering & Technology conference (MMLDT), 2021
8. (Oral presentation) **M. Barzegari**, L. Geris, "High-performance computing in biomedical engineering; a use-case for biomaterials degradation modeling". 17th International Symposium on Computer Methods in Biomechanics and Biomedical Engineering (CMBBE), 2021
9. (Oral presentation) **M. Barzegari**, D. Mei, S.V. Lamaka, L. Geris, "Mathematical modeling of degradation process of biodegradable metallic biomaterials in immersion and perfusion setups". XXVIII Congress of the International Society of Biomechanics (ISB), 2021
10. (Oral presentation) **M. Barzegari**, L. Geris, "Mathematical modeling of biodegradation of metallic biomaterials using reaction-diffusion equations and level set method". SIAM Conference on Mathematical Aspects of Materials Science, 2021
11. (Oral presentation) **M. Barzegari**, L. Geris, "Reproducible research in computational sciences: A use case for uncertainty quantification using Jupyter notebooks". KU Leuven Open Science Study Day, 2021

12. (Oral presentation) **M. Barzegari**, L. Geris, "Investigating the Biodegradation of Metallic Biomaterials using HPC-Based Simulation Techniques". 14th World Congress on Computational Mechanics, 2021
13. (Oral presentation) **M. Barzegari**, L. Geris, "Computational modeling of in-vitro biodegradation of metallic scaffolds and bone implants". 11th World Biomaterials Congress, 2020
14. (Poster presentation) **M. Barzegari**, L. Geris, "Jupyter for uncertainty quantification and parameter estimation of computational models". Jupyter-Con, 2020
15. (Oral presentation) **M. Barzegari**, L. Geris, "High-performance numerical simulation of biodegradation process with moving boundaries". FreeFEM Days, 11th Edition, 2019
16. (Oral presentation) **M. Barzegari**, L. Geris, "Computational Modeling Of Biodegradation Of Metallic Biomaterials". 18th National Day on Biomedical Engineering, 2019
17. (Poster presentation) **M. Barzegari**, L. Geris, "Developing a mathematical model of biodegradable metallic scaffolds for bone tissue engineering applications". 7th Belgian Symposium on Tissue Engineering, 2019
18. (Oral presentation) **M. Barzegari**, F.P. Boerema, L. Geris, "Computational optimization and biodegradation of 3D-printed patient-specific acetabular implants". European Orthopaedic Research Society (EORS), 2019
19. (Oral presentation) **M. Barzegari**, L. Geris, "High-performance simulation of biodegradation behavior of magnesium-based biomaterials". Fluid and solid mechanics for tissue engineering, 2019
20. (Oral presentation) **M. Barzegari**, L. Geris, "Numerical simulation of biodegradation and corrosion of magnesiumbased orthopedic implants". 2nd International Conference on Simulation for Additive Manufacturing, 2019
21. (Oral presentation) **M. Barzegari**, L. Geris, "Mathematical modeling of biodegradation of metal implants in orthopedics". 11th Symposium on Biodegradable Metals, Alicante, 2019

## Conference and symposium abstracts (co-author)

1. L. Lafuente Gracia, **M. Barzegari**, L. Geris, "Towards an open-source bioregulatory 3D model of bone fracture healing in FreeFEM", 9th World Congress of Biomechanics (WCB), 2022
2. L. Lafuente Gracia, **M. Barzegari**, L. Geris, "Towards an in silico bioregulatory model of osteogenesis and sprouting angiogenesis in 3D", 27th Congress of the European Society of Biomechanics (ESB), 2022
3. P. Ansoms, **M. Barzegari**, L. Geris, "Finite element analysis of mechanical behavior of a jaw plate during the implant biodegradation process", 27th Congress of the European Society of Biomechanics (ESB), 2022
4. R. de Vries, **M. Barzegari**, S. Mohammed, A. Stell, C. Hermanns, M. Jetten, D. de Bont, O.P. da Silva Filho, V. Vaithilingam, A Carlier, L. Geris, A. van Apeldoorn, (2021), "Upscaling of a Next Generation Microwell-Based Beta Cell Replacement Device". 6th TERMIS World Congress on Tissue Engineering and Regenerative Medicine (TERMIS), 2021
5. F. Perez-Boerema, **M. Barzegari**, L. Geris, "Creating your own TPMS-based functionally graded scaffolds for 3D-printing". 17th International Symposium on Computer Methods in Biomechanics and Biomedical Engineering (CMBBE), 2021
6. J.B. Fano, A. Shapeti, M. Condor, J. De Jong, A.A. Fernández, **M. Barzegari**, J.A. Sanz-Herrera, H. van Oosterwyck, (2021), "Quantifying cellular forces in a 3D in vitro vascular model". 17th International Symposium on Computer Methods in Biomechanics and Biomedical Engineering (CMBBE), 2021



FACULTY OF ENGINEERING SCIENCE  
DEPARTMENT OF MECHANICAL ENGINEERING  
BIOMECHANICS SECTION  
Celestijnenlaan 300 box 2419  
B-3001 Leuven

